

**Analytical and Experimental Modeling of Internal Erosion in
Porous Media**

by

Saman Azadbakht

A thesis submitted in partial fulfillment of the requirements for the degree of

Doctor of Philosophy

in

Petroleum Engineering

Department of Civil and Environmental Engineering

University of Alberta

© Saman Azadbakht, 2015

Abstract

Constitutive law is a key component in the development of numerical models to simulate erosion of solid particles in a porous medium. In combination with the principle of conservation of mass, these models allow the estimation of internal erosion rate as a function of various parameters such as fluid velocity and time. This research aims at enhancing the existing constitutive laws describing the internal erosion phenomenon.

Using the principles of dimensional analysis, we developed a mathematical relation between the internal erosion rate, fluid velocity and a proportionality constant called erosion coefficient. An equation is derived which indicates that the erosion coefficient is a function of grain density, particle Reynolds number and porosity variation during the erosion. Results of a series of erosion experiments were used to calibrate and validate the proposed constitutive law. The model is able to explain decreasing erosion rate over time. Further, the comparison between experimental data and analytical predictions show that the proposed model is able to predict the experimental results with reasonable accuracy.

An experimental apparatus was designed and set up to perform a series of internal erosion tests on unconsolidated sand packs with different grain size distributions (GSD). The tests were conducted at different hydraulic gradients. During the testing, inflow pressure, fluid flow rate and turbidity of outflow stream were monitored and recorded. In this way, the mass of eroded particles was estimated as a function of time for different GSD's.

Based on the observations from the experimental results, we developed another constitutive law to model internal erosion as an exponential decay process. This model is an enhancement to the model that we developed using dimensional analysis technique. The proposed constitutive law was calibrated using the test results we gathered in our experimental program and some experimental data that we obtained from the literature. The results of this analysis show that internal erosion is, indeed, an exponential decay phenomenon. This erosion constitutive model has two calibration parameters, namely, final value of porosity, φ_f , and decay coefficient, λ . We developed, using dimensional analysis technique, relationships to predict φ_f and λ using material and test parameters. The proposed relationships were calibrated and validated using experimental data and the validation results show that the proposed relationships can predict φ_f and λ with reasonable accuracy.

Acknowledgements

I am grateful to my supervisor, Dr. Alireza Nouri, for his guidance and support throughout my research work. I am, also, thankful to my co-supervisor, Dr. Dave Chan, for his help and advice during this work.

I would like to thank petroleum engineering technician, Todd Kinnee, for his help in design and set-up of the experimental apparatus. Help of Christine Hereygers with experimental work is appreciated as well.

Also, I want to thank the thesis examination committee members, Dr. Farshid Torabi, Dr. Douglas Schmitt, Dr. Lijun Deng and Dr. Huazhou Li, for providing valuable comments for further improvement of this thesis.

Table of Contents

Abstract	ii
Acknowledgements	iv
Table of Contents.....	v
List of Tables	viii
List of Figures and Illustrations	x
CHAPTER ONE: INTRODUCTION	1
1.1 Background.....	1
1.2 Statement of the problem and research objectives	2
1.3 Methodology.....	3
1.4 Structure of the thesis	3
CHAPTER TWO: LITERATURE REVIEW	5
2.1 Introduction	5
2.2 The erosion phenomenon.....	7
2.2.1 Internal erosion	7
2.2.2 Surface erosion	8
2.3 Study of internal and surface erosion in petroleum engineering	8
2.3.1 Fines migration.....	9
2.3.2 Sand production.....	10
2.4 Experimental study of erosion phenomenon.....	11
2.4.1 Internal erosion experiments	12
2.4.2 Surface erosion experiments	17
2.5 Common constitutive laws for modeling the erosion phenomenon	20
2.6 Summary.....	22
2.7 Nomenclature	23
2.8 References	23
CHAPTER THREE: CONSTITUTIVE MODELING OF INTERNAL EROSION IN POROUS MEDIA USING DIMENSIONAL ANALYSIS TECHNIQUE.....	28
3.1 Introduction	28
3.2 Mathematical modeling.....	29
3.2.1 Modified erosion law.....	30
3.2.2 Critical fluid velocity	34
3.2.2.1 Pressure gradient force	34
3.2.2.2 Drag force	35
3.2.2.3 Gravity force due to buoyant weight of the particle.....	36
3.2.2.4 Erosion condition.....	36
3.3 Experimental data	37
3.4 Model calibration	40

3.5 Model validation	47
3.6 Discussion and concluding remarks	50
3.7 Nomenclature	51
3.8 References	53
CHAPTER FOUR: EXPERIMENTAL INVESTIGATION OF INTERNAL EROSION IN UNCONSOLIDATED POROUS MEDIA	55
4.1 Introduction	55
4.2 Experimental set-up	55
4.2.1 Data Acquisition	59
4.3 Test specimen preparation	62
4.4 Test specimen packing method	65
4.4.1 Sample saturation	67
4.5 Testing plan	67
4.5.1 Trial tests	68
4.6 Results of main erosion tests	69
4.6.1 Test repeatability	69
4.6.2 Test results	72
4.6.2.1 Different GSD's and same hydraulic gradient	73
4.6.2.2 Same GSD and different hydraulic gradients	75
4.7 Discussion	78
4.8 Nomenclature	80
4.9 References	81
CHAPTER FIVE: MODELING INTERNAL EROSION IN POROUS MEDIA AS AN EXPONENTIAL DECAY PHENOMENON	83
5.1 Introduction	83
5.2 Mathematical modeling	83
5.3 Determining model parameters	86
5.4 Applying the model to constant velocity erosion tests	86
5.5 Applying the model to variable velocity tests	93
5.5.1 Grain size distribution #1 (GSD1)	94
5.5.2 Grain size distribution #2 (GSD2)	98
5.5.3 Grain size distribution #3 (GSD3)	101
5.6 Discussion and concluding remarks	105
5.7 Nomenclature	106
5.8 References	106
CHAPTER SIX: DEVELOPING RELATIONSHIPS FOR THE PREDICTION OF φ_f AND λ USING DIMENSIONAL ANALYSIS TECHNIQUE	107
6.1 Introduction	107
6.2 Mathematical modeling	108

6.2.1 Final porosity, φ_f	108
6.2.2 Decay coefficient, λ	111
6.3 Experimental data	112
6.4 Model calibration	115
6.4.1 Constant velocity tests	116
6.4.2 Variable velocity tests	118
6.5 Model validation	121
6.5.1 Constant velocity tests	121
6.5.2 Variable velocity tests	123
6.6 Discussion and concluding remarks.....	124
6.7 Nomenclature	125
6.8 References	126
CHAPTER SEVEN: CONCLUDING REMARKS.....	127
7.1 Main contributions	127
7.2 Recommendations for further research.....	129
BIBLIOGRAPHY.....	132
APPENDIX A: MODIFICATION OF EROSION CONSTITUTIVE LAW BASED ON DIMENSIONAL ANALYSIS TECHNIQUE BY USING TANGENT EROSION RATE.....	137
A.1. Introduction.....	137
A.2. Mathematical modeling	138
A.3. Experimental data and model calibration.....	139
A.4. Model validation.....	145

List of Tables

Table 2-1: Summary of issues related to erosion phenomenon	11
Table 3-1: Properties of the silty-sand used in the experiments by Sterpi (2003).....	39
Table 3-2: Summary of calibration parameters for Tests 1, 2 and 3.....	45
Table 3-3: Calculated values of α and β for Tests 4 and 5	49
Table 4-1: Properties of the three GSD's used in the erosion experiments.....	63
Table 4-2: Properties of the test specimens used in the erosion experiments	65
Table 4-3: Testing plan.....	67
Table 4-4: Comparison of repeatability tests for GSD1	72
Table 4-5: Comparison of repeatability tests for GSD2.....	72
Table 5-1: Parameters of the erosion experiments in Sterpi (2003).....	87
Table 5-2: Summary of calibration parameters for constant velocity tests	90
Table 5-3: Properties of the test specimens used in variable velocity erosion experiments.....	93
Table 5-4: Summary of calibration parameters for GSD1 tests	96
Table 5-5: Summary of calibration parameters for GSD2 tests	100
Table 5-6: Summary of calibration parameters for GSD3 tests	103
Table 6-1: Required parameters for model calibration for Sterpi (2003), GSD1, GSD2 and GSD3 experiments	115
Table 6-2: Required parameters for model calibration, Sterpi (2003) tests.....	116
Table 6-3: Summary of calibration parameters for Tests 1, 2 and 3, Sterpi (2003).....	118
Table 6-4: Required parameters for model calibration, variable velocity tests (GSD1, GSD2 and GSD3)	119
Table 6-5: Summary of calibration parameters for variable velocity tests listed in Table 6-4	121
Table 6-6: Calculated values of φ_f and λ for Tests 4 and 5, Sterpi (2003)	121
Table 6-7: Calculated values of φ_f and λ for Tests GSD1-2 and GSD2-2.....	123

Table A-1: Summary of calibration parameters for Tests 1, 2 and 3143
Table A-2: Calculated values of α and β for Tests 4 and 5.....147

List of Figures and Illustrations

Figure 2-1: Schematic of internal erosion process.....	6
Figure 2-2: Schematic of surface erosion process.	6
Figure 2-3: Experimental set-up used by Skempton and Brogan (1994).....	13
Figure 2-4: Experimental set-up used by Adel et al. (1994).....	14
Figure 2-5: Experimental set-up used by Wilhelm (2000).....	15
Figure 2-6: Experimental setup used by Sterpi (2003).....	16
Figure 2-7: Schematic of the apparatus used by Papamichos et al. (2001).....	19
Figure 2-8: Schematic of the apparatus used by Servant et al. (2006).....	19
Figure 3-1: Grain size distribution for the silty-sand used for laboratory experiments, Sterpi (2003)	39
Figure 3-2: Results of erosion tests on silty-sand for different hydraulic gradients, Sterpi (2003)	40
Figure 3-3: Calibrating model parameters for Test 1 ($i=0.18$)	43
Figure 3-4: Calibrating model parameters for Test 2 ($i=0.39$)	44
Figure 3-5: Calibrating model parameters for Test 3 ($i=0.55$)	44
Figure 3-6: Comparison between experimental and calculated values of secant erosion rate, $i=0.18$	46
Figure 3-7: Comparison between experimental and calculated values of secant erosion rate, $i=0.39$	46
Figure 3-8: Comparison between experimental and calculated values of secant erosion rate, $i=0.55$	47
Figure 3-9: Variation of α with hydraulic gradient for Tests 1, 2 and 3 and best fit (solid line)	47
Figure 3-10: Variation of β with hydraulic gradient for Tests 1, 2 and 3 and best fit (solid line)	48
Figure 3-11: Comparison between experimental results and model prediction of secant erosion rate, $i=0.60$	49
Figure 3-12: Comparison between experimental results and model prediction of secant erosion rate, $i=0.75$	50

Figure 4-1: Schematic of the experimental set-up (not to scale)	57
Figure 4-2: Photograph of the experimental apparatus	58
Figure 4-3: Position of outflow ports with relation to the test specimen	59
Figure 4-4: Portable turbidimeter used in the experiments. Picture from manufacturer's website (http://www.hfscientific.com)	60
Figure 4-5: Calibration curve for the turbidity meter used in the experiments	61
Figure 4-6: Grain size distribution of coarse sand, fine sand and silt, used to make artificial samples.....	62
Figure 4-7: Grain size distribution of artificial test materials	64
Figure 4-8: Fluid velocity vs. hydraulic gradient for fine sand component	69
Figure 4-9: Test repeatability for GSD1 at hydraulic gradient of 0.7, comparison of eroded mass	70
Figure 4-10: Test repeatability for GSD1 at hydraulic gradient of 0.7, comparison of permeability	70
Figure 4-11: Test repeatability for GSD2 at hydraulic gradient of 0.7, comparison of eroded mass	71
Figure 4-12: Test repeatability for GSD2 at hydraulic gradient of 0.7, comparison of permeability	71
Figure 4-13: Comparison of eroded mass for all GSD's at hydraulic gradient of 0.5.....	73
Figure 4-14: Comparison of permeability for all GSD's at hydraulic gradient of 0.5.....	73
Figure 4-15: Comparison of eroded mass for all GSD's at hydraulic gradient of 0.7.....	74
Figure 4-16: Comparison of permeability for all GSD's at hydraulic gradient of 0.7.....	74
Figure 4-17: Comparison of eroded mass for GSD1 at hydraulic gradients of 0.3 and 0.5.....	75
Figure 4-18: Eroded mass for GSD1 at hydraulic gradient of 0.7.....	76
Figure 4-19: Comparison of permeability for GSD1 at different hydraulic gradients.	76

Figure 4-20: Comparison of eroded mass for GSD2 at different hydraulic gradients.....	77
Figure 4-21: Comparison of permeability for GSD2 at different hydraulic gradients.....	77
Figure 4-22: Comparison of eroded mass for GSD3 at different hydraulic gradients.....	78
Figure 4-23: Comparison of permeability for GSD3 at different hydraulic gradients.....	78
Figure 5-1: Eroded mass vs. time for constant velocity erosion tests, (Sterpi 2003).....	87
Figure 5-2: Calibration of λ for Test 1 ($i=0.18$).....	88
Figure 5-3: Calibration of λ for Test 2 ($i=0.39$).....	88
Figure 5-4: Calibration of λ for Test 3 ($i=0.55$).....	89
Figure 5-5: Calibration of λ for Test 4 ($i=0.60$).....	89
Figure 5-6: Calibration of λ for Test 5 ($i=0.75$).....	90
Figure 5-7: Comparison between model and experiment, Test 1.....	91
Figure 5-8: Comparison between model and experiment, Test 2.....	91
Figure 5-9: Comparison between model and experiment, Test 3.....	92
Figure 5-10: Comparison between model and experiment, Test 4.....	92
Figure 5-11: Comparison between model and experiment, Test 5.....	93
Figure 5-12: Eroded mass vs. time for GSD1.....	94
Figure 5-13: Calibration of λ for Test 1 ($i=0.30$), GSD1.....	95
Figure 5-14: Calibration of λ for Test 2 ($i=0.50$), GSD1.....	95
Figure 5-15: Calibration of λ for Test 3 ($i=0.70$), GSD1.....	96
Figure 5-16: Comparison between model and experiment, Test 1, GSD1.....	97
Figure 5-17: Comparison between model and experiment, Test 2, GSD1.....	97
Figure 5-18: Comparison between model and experiment, Test 3, GSD1.....	98
Figure 5-19: Eroded mass vs. time for GSD2.....	99

Figure 5-20: Calibration of λ for Test 1 ($i=0.50$), GSD2.....	99
Figure 5-21: Calibration of λ for Test 2 ($i=0.70$), GSD2.....	100
Figure 5-22: Comparison between model and experiment, Test 1, GSD2	101
Figure 5-23: Comparison between model and experiment, Test 2, GSD2	101
Figure 5-24: Eroded mass vs. time for GSD3.....	102
Figure 5-25: Calibration of λ for Test 1 ($i=0.50$), GSD3.....	102
Figure 5-26: Calibration of λ for Test 2 ($i=0.70$), GSD3.....	103
Figure 5-27: Comparison between model and experiment, Test 1, GSD3	104
Figure 5-28: Comparison between model and experiment, Test 2, GSD3	104
Figure 6-1: Results of erosion tests for different hydraulic gradients, Sterpi (2003).....	113
Figure 6-2: Eroded mass vs. time for GSD1, Tests 1 and 2.....	113
Figure 6-3: Eroded mass vs. time for GSD1, Test 3.....	114
Figure 6-4: Eroded mass vs. time for GSD2.....	114
Figure 6-5: Eroded mass vs. time for GSD3.....	115
Figure 6-6: Calibrating α and β for Tests 1, 2 and 3, Sterpi (2003).....	117
Figure 6-7: Calibrating γ_1 and γ_2 for Tests 1, 2 and 3, Sterpi (2003).....	118
Figure 6-8: Calibrating α and β for variable velocity tests	120
Figure 6-9: Calibrating γ_1 and γ_2 for variable velocity tests	120
Figure 6-10: Comparison between experimental results and model prediction of eroded mass, Test 4, Sterpi (2003)	122
Figure 6-11: Comparison between experimental results and model prediction of eroded mass, Test 5, Sterpi (2003)	122
Figure 6-12: Comparison between experimental results and model prediction of eroded mass, Test GSD1-2, $i=0.50$	123
Figure 6-13: Comparison between experimental results and model prediction of eroded mass, Test GSD2-2, $i=0.70$	124
Figure A-1: Calibrating model parameters for Test 1 ($i=0.18$).....	141

Figure A-2: Calibrating model parameters for Test 2 ($i=0.39$).....	142
Figure A-3: Calibrating model parameters for Test 3 ($i=0.55$).....	142
Figure A-4: Comparison between experimental and calculated values of tangent erosion rate, $i=0.18$	144
Figure A-5: Comparison between experimental and calculated values of tangent erosion rate, $i=0.39$	144
Figure A-6: Comparison between experimental and calculated values of tangent erosion rate, $i=0.55$	145
Figure A-7: Variation of α with hydraulic gradient for Tests 1, 2 and 3 and best fit (solid line)	145
Figure A-8: Variation of β with hydraulic gradient for Tests 1, 2 and 3 and best fit (solid line)	146
Figure A-9: Comparison between experimental results and model prediction of tangent erosion rate, $i=0.60$	147
Figure A-10: Comparison between experimental results and model prediction of tangent erosion rate, $i=0.75$	148

Chapter 1

Introduction

1.1 Background

The phenomenon of mass transport in porous media has been studied in various engineering fields. Different terminologies are used to describe this process such as particle erosion, fines migration, scour erosion, piping erosion, suffusion, etc.

In the petroleum industry, particle erosion refers to the concurrent production of solid particles along with reservoir fluids and is a common problem encountered in oil and gas production operations. In petroleum engineering terminology, this process is known as fines migration or sand production. Although fines migration and sand production have some similarities, they are usually treated as two different phenomena. These phenomena can be distinguished based on the dominant forces driving the process, size of the mobilized particles and production and operational consequences.

Particle erosion process consists of two distinct stages:

- 1) Generation of loose particles. In case of sand production, this happens through mechanical degradation and failure of the reservoir rock during which, rock turns into cohesionless fragments; and in the case of fines migration, the loose particles can be the small particles not carrying any load in the structure of the rock or they can be the result of grain crushing upon reservoir depletion.
- 2) Transport of loose particles fragments through the porous medium into the perforations or wellbore. In case of sand production, this happens under the

influence of hydrodynamic forces of the flowing fluids and in case of fines migration, the driving mechanism is a combination of colloidal forces and the hydrodynamic forces.

In this context, if the particles migrate from within the porous media, the process is known as internal erosion and if the particles are eroded from the surface of the cavity, the process is referred to as surface erosion. Therefore, fines migration can be classified as a form of internal erosion and sand production can be either internal erosion or surface erosion or a combination of both.

Extensive research in different fields of engineering has been carried out in the past century to identify the key parameters controlling the initiation and severity of internal and surface erosion in porous media. Researchers have used analytical and numerical modeling techniques along with laboratory experiments for better understanding of the erosion phenomenon. By adopting the principle of conservation of mass, numerical models estimate the solid erosion rate as a function of various parameters. A key component in the structure of such numerical models is the erosion constitutive law.

Laboratory testing of erosion plays an important role in development of any analytical or numerical tool for modeling this phenomenon. Laboratory experiments are required to calibrate and validate analytical and/or numerical models. In the existing literature, the erosion experiments are conducted on both consolidated (rocks) and unconsolidated (loose sands, soils) porous media. The usual form of erosion experiments in rocks is performed on hollow cylinder test specimens (whether natural or synthetic) or perforated samples with various stress and fluid flow schemes. Erosion tests are also conducted on unconsolidated porous media in small-scale and large-scale experiments. More details regarding erosion modeling is provided in Chapter 2.

1.2 Statement of the problem and research objectives

As mentioned earlier, one of the main components of existing analytical and numerical models for the modeling of erosion in porous media is the constitutive law for erosion. To the best of our knowledge, all the existing laws for internal

erosion are partially based on intuitive assumptions and lack substantial experimental evidence. The objective of this research is to provide an enhancement to existing constitutive laws for describing internal erosion in porous media.

1.3 Methodology

Our research focuses on the development of a constitutive law for the description of internal erosion. We use a combination of analytical and experimental modeling approaches to achieve this goal.

Using the principles of dimensional analysis, a mathematical relationship is derived for the assessment of the rate of internal erosion in relation to the fluid velocity and a proportionality constant called the erosion coefficient, λ . This coefficient is one of the main parameters in existing constitutive laws for internal erosion, which has to be calibrated experimentally. Using the theoretical relationship for calculating the rate of erosion, we can relate λ to grain density, particle Reynolds number and porosity changes. We used published data of a series of erosion experiments to establish the functional relationship between λ and other parameters.

We designed and built an experimental apparatus to conduct the internal erosion tests. We used unconsolidated test specimens which were prepared by mixing different proportions of coarse sand, fine sand and silt. The grain size distributions of the test specimens were designed to resemble typical hydrocarbon-bearing sand formations. Based on the observations from experimental results, we developed a constitutive law for internal erosion based on the concept of exponential decay. The proposed constitutive law was calibrated using the test results we gathered in our experimental program and some experimental data that we obtained from the literature.

1.4 Structure of the thesis

This thesis consists of seven chapters. Chapter 1 gives a brief introduction into the objective, methodology and significance of our work. Chapter 2 presents a review of the existing literature on the topic of particle erosion in porous media.

Chapter 3 presents the constitutive law that we propose for internal erosion based on the dimensional analysis approach. The model has been calibrated and validated using experimental data we obtained from the literature. The advantage of the proposed model is that it offers a functional form for the erosion coefficient. This functional form accounts for the effect of parameters such as grain specific density, particle Reynolds number and porosity variations on erosion coefficient, which had not been explicitly addressed in previous works. The validation results show that the model is able to predict the erosion rates with reasonable accuracy.

Chapter 4 contains the details of our experimental program such as specifications of the experimental apparatus and data acquisition methods, the procedures for preparation of test specimen, testing plan and results.

In Chapter 5, we have tried to model the internal erosion in porous media as an exponential decay phenomenon. Here, instead of modeling the rate of eroded solids, we model the rate of decay of the initial erodible mass within the test specimen. The developed model has been calibrated using test data from 12 different tests and four grain size distributions. The results show that internal erosion is, indeed, an exponential decay process.

The proposed model in Chapter 5 has two calibration parameters, namely, final value of porosity, φ_f , and decay coefficient, λ . In Chapter 6, we used dimensional analysis technique to develop relationships to predict φ_f and λ using material and test parameters. The suggested relationships were calibrated and validated using experimental data and the validation results show that the proposed relationships can predict φ_f and λ with reasonable accuracy.

Chapter 7, which is the last chapter of this thesis, contains the conclusions that we draw from our work along with recommendations for further research.

Appendix A (only appendix of the thesis) is very similar to Chapter 3 with the exception that the proposed model is reformulated based on tangent erosion rate instead of secant erosion rate. All chapters have their own list of nomenclature and references. Slightly different versions of Chapters 3, 4, 5 and 6 are submitted to different journals for review and publication. Also, a bibliography is given at the end of the thesis which combines all the references used throughout this work.

Chapter 2

Literature Review

2.1 Introduction

Mass transport in porous media has been studied across a broad spectrum of engineering disciplines. As such, different terminologies are used in different fields to refer to this phenomenon. Thus, it is inevitable to explain and distinguish between different definitions and terminologies from the beginning. Generally speaking, mass transport in porous media can be divided into two main categories:

1. The finer particles are transported by the seepage forces within a fixed framework formed by the coarser particles. Generally, this form of mass transport doesn't involve direct geometrical changes in the structure of porous media (even though particle rearrangement may happen) and is referred to as internal erosion. Other equivalent terms for this process are "piping erosion" and "suffusion".
2. Particles are transported by the seepage forces parallel or perpendicular to the surface of the porous medium. This form of mass transport involves visible geometrical changes to the structure of the material and is referred to as surface erosion or scour erosion. In this form of erosion, the particles move by sliding, rolling or a combination of both.

To better illustrate the differences between these two categories, idealized schematics of internal erosion and surface erosion are depicted in Figure 2-1 and Figure 2-2 respectively. In these figures, the blue arrows show the direction of

fluid flow and red arrows show the direction of particle movement. In case of internal erosion, the direction of fluid flow can be upward, downward or horizontal. In case of surface erosion, the fluid flow direction is usually parallel to the material surface. Surface erosion induced by a fluid flow perpendicular to the material surface is referred to as fluidization.

A brief review of the research on these topics in various fields of engineering is presented in the next sections. More emphasis is given to the research and applications in the field of petroleum engineering.

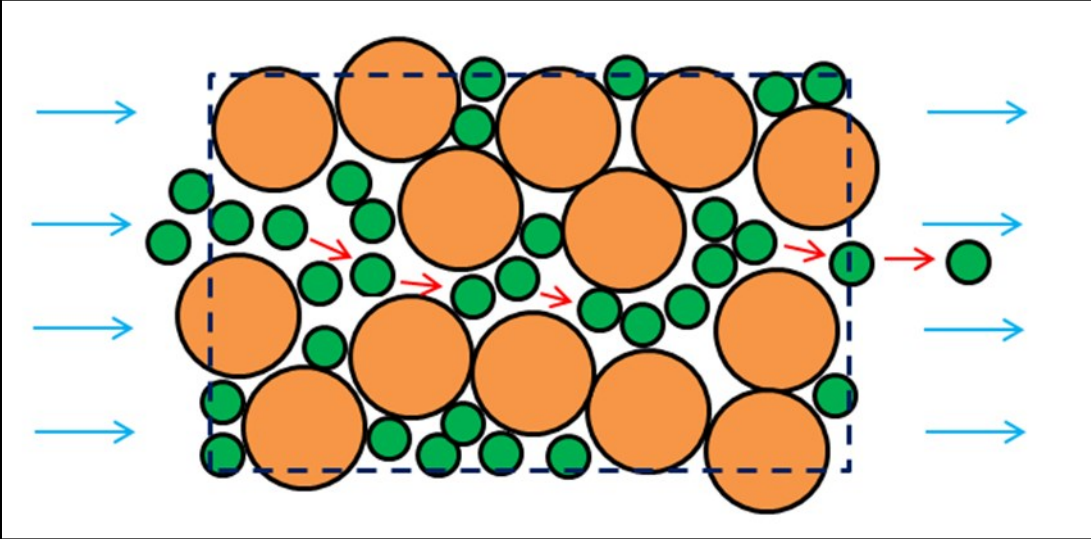


Figure 2-1: Schematic of internal erosion process.

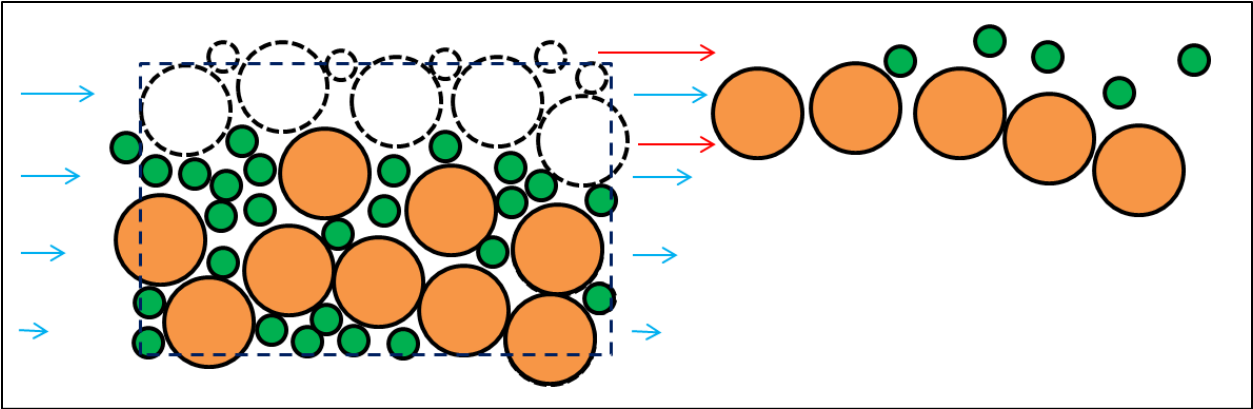


Figure 2-2: Schematic of surface erosion process.

2.2 The erosion phenomenon

As mentioned earlier, the erosion phenomenon has been extensively studied in various fields of engineering. Erosion happens in many natural and man-made structures such as river embankments and earth dams and it usually has detrimental effects on the stability of structures. As such, the erosion phenomenon has found high importance in engineering science due to its economics and safety implications. There is a plethora of literature available regarding research on this topic. Following sections give a glimpse into the research on internal and surface erosion phenomena in different fields of engineering.

2.2.1 Internal erosion

Internal erosion is a common problem encountered in earth structures such as water dams, river/highway embankments and coastal protection structures. This problem is also known as “filter instability”. An ideal (stable) filter allows seepage of fluids through it but at the same time, prevents the erosion of finer particles. Loss of mass due to internal erosion can jeopardize stability of the earth structures. Due to its area of application and importance from economic and safety point of view, the phenomenon of internal erosion has been extensively studied in the past century by civil engineers. Karl Terzaghi is believed to be the first one who conducted laboratory experiments to study filter instability mechanisms in the 1920’s (Nguyen, 2012). Almost all of the works in this area focus on determining the filter stability criteria. Filter stability criteria are the rules prescribing the relative percentages of fine and coarse components of the filter to eliminate or minimize internal erosion (de Graauw et al. 1984; Kenny and Lau, 1985; Skempton and Brogan, 1994).

Urban regions are among other areas where the internal erosion of subsurface soil can be problematic. In some cities, aggressive water pumping from subsurface water tables, on which the cities are built, have drawn the attention to the possibility of erosion of finer portions of the subsurface soil and the consequent changes in soil’s physical and mechanical properties. Researchers have shown that changes in soil’s physical and mechanical properties due to internal erosion can potentially lead to surface subsidence and instability of buildings and structures

(Sterpi 2003; Cividini et al. 2004; Cividini et al. 2009). Similar research has been carried out in the area of water treatment and sanitation. Water sanitation is in fact a *reverse* internal erosion process by which the solid particles are removed from the fluid phase as they pass through a porous sand pack. Research about this process, which is also known as “sand bed filtration”, goes back to 1930’s (e.g., ASCE 1936; Baylis 1937; Iwasaki 1937). In water sanitation, the focus is on separation of suspended and colloidal particles in the clay-size range from water. Later on, filtration experiments were conducted involving particle sizes in the silt-sand range (Sakthivadivel 1967). A comprehensive review of the models for water filtration can be found in Sakthivadivel and Irmay (1966).

2.2.2 Surface erosion

Surface erosion in the form of scour is believed to be the main cause of failure of bridges and other hydraulic and coastal structures (Briaud et al. 2001). In such situations, the porous bed in the vicinity of the bridge piers and coastal structures is washed away under the hydrodynamic shear stresses exerted by the fluid currents or waves; resulting in instability and eventually failure of the structure. Again, in depth theoretical and experimental research has been carried out to determine and predict the scour erosion rate and erosion depth in such circumstances (Briaud et al. 1999; Wand and Fell 2004; Indraratna et al. 2008; Indraratna et al. 2013). Also, surface erosion of soil through defective sewer pipes can result in creation of sinkholes which are, again, a major concern in urban regions from the safety and economics point of view (Guo et al. 2013).

2.3 Study of internal and surface erosion in petroleum engineering

The topic of particle erosion in porous media is also of particular interest to petroleum engineers. In petroleum industry, this phenomenon is categorized into fines migration and sand production and research on these topics can be traced back to 1930’s (Wilson 1933; Coberly 1937; Chenault 1938). Extensive research has been carried out since then to identify the key parameters affecting the initiation and severity of this phenomenon. Although fines migration and sand production have some similarities, they are usually treated as two different

phenomena. These phenomena can be distinguished based on the dominant forces driving the process, size of the mobilized particles and production and operational consequences. These differences are discussed in the following paragraphs.

2.3.1 Fines migration

Fines migration is defined as the mobilization and transport of infinitesimal loose particles present in the pore space of the rock (Gruesbeck and Collins 1982; Khilar and Fogler 1983). Fines migration is mainly an electro-chemical process and is greatly affected by water salinity and particle wettability (Muecke 1979; Selby and Ali 1988). Colloidal forces such as electric double-layer repulsion, London-Van der Waals attraction, Born repulsion and acid-base interactions are the main contributing forces in the release and mobilization of fines adhered to the pore structure of the rock (Khilar and Fogler 1987).

Fines migration is usually considered in the context of formation damage and impaired wellbore productivity. If the sizes of the mobilized fines are larger than pore constrictions, or if the fine particles move in high concentrations, it results in fines redeposition by either particle entrapment or particle bridging. Particle entrapment, which is also known as pore clogging, reduces the available cross sectional area for fluid flow, resulting in severe permeability reduction especially in the near wellbore region.

Regarding the size of the migrating fines in porous media, there doesn't seem to be a unanimous agreement between different researchers. For example, Khilar and Fogler (1998) have suggested the fine particle range to be between 1 to 5 microns and seldom exceeding 10 microns. Vaidya (1991) performed a waterflooding test on a Berea sandstone core and collected the effluent. The results of particle size analysis showed that the majority of fine particles in the effluent fall in the range 2-4 microns. Li (2000) performed core flooding experiments to study the effect of fines migration on oil recovery in waterflooding projects. In these experiments, clay particles in the range of 1-2 microns were used to represent formation fines. Gruesbeck and Collins (1982) conducted fine migration experiments on synthetic and natural cores. In their work, they defined fines as particles which have a diameter of less than 5 microns. Therefore, as a general rule of thumb, one can

consider a range of 1-5 microns a reasonable representative range for the size of formation fines. A comprehensive review on the topic of fines migration can be found in Khilar and Fogler (1998).

2.3.2 Sand production

Sand production is a common problem in production and injection wells. As the name implies, sand production refers to the production of loose sand particles along with hydrocarbon fluids from the reservoir. Sand production can occur as an internal or surface erosion process or as a combination of both. Numerous factors can contribute to sand production among them being the rock strength, in-situ stresses, reservoir pressure, water cut, fluid flow rate and wellbore completion. An exhaustive list of such factors can be found in Veeken et al. (1991).

The two main mechanisms responsible for sanding, are mechanical failure of rock and hydrodynamic forces that carry rock fragments into the wellbore. These two mechanisms are coupled in nature i.e., rock failure is a precursor to sanding and sanding furthers rock failure. Rock around the cavity may undergo plastic deformation and disaggregation. Rock disaggregation may generate loose rock fragments which could then be carried into the perforation cavity and/or wellbore by the seepage forces of the reservoir fluid (Vardoulakis et al. 1996; Papamichos and Vardoulakis 2005).

In sand production, colloidal forces don't play any role and the main driving force (after rock failure and disaggregation) is brought about by the action of hydrodynamic forces of the flowing fluid. Since the size of particles in sand production is usually a few orders of magnitude larger than those in fines migration, gravity force can also play a significant role in this process.

Sand production is usually considered a significant issue because of the operational problems that it causes such as damage to downhole tubular and equipment. Sand particles can act as abrasives especially at high fluid velocities and can cause severe damage to downhole and surface equipment through abrasion and erosion. Also, larger sand particles can settle down in the wellbore due to gravity forces and over time, they can plug the producing zones; a

phenomenon which is referred to as “sand-up” (Wilson 1933). Such problems are not encountered in case of fines migration and production. Contrary to fines migration, sand production is sometimes considered a production enhancement mechanism. This is particularly applicable in heavy oil fields (Vaziri et al. 2002) in which sand influx is necessary to result in higher production rates than conventional methods that try to exclude sand from hydrocarbon fluids.

A summary of the above discussion is presented in Table 2-1. This table shows the common problems arising from erosion phenomenon in various fields of engineering along with a few related references.

Table 2-1: Summary of issues related to erosion phenomenon

Issue	Field of study	Example reference
Fines migration Sand production	Petroleum engineering	Muecke 1979 Gruesbeck and Collins 1982 Selby and Ali 1988
Surface subsidence	Geotechnical engineering Structural engineering	Sterpi 2003 Cividini et al. 2009
Filter stability	Dam Engineering	de Graauw et al. 1984 Kenny and Lau 1985 Skempton and Brogan 1994
Scour erosion Sediment transport Sinkholes	Highway engineering River engineering Urban design	Briaud et al. 2001 Indraratna et al. 2008 Gou et al. 2013

2.4 Experimental study of erosion phenomenon

For better understanding of the erosion mechanism, researchers have extensively studied internal and surface erosion experimentally. Internal and surface erosion tests have been conducted on rocks and cohesionless porous media (sands and soils). Such tests have also been used to calibrate and validate the numerical models developed for the purpose of erosion prediction and quantification. The following sections present a brief review of experimental research for investigation

of internal and surface erosion in rocks and cohesionless porous media. Emphasis is placed on the experimental study of the internal erosion process.

2.4.1 Internal erosion experiments

In this section, first, a review is provided on different forms of internal erosion experiments related to geofilter design and stability (common in the field of geotechnical engineering) and surface subsidence due to soil erosion (structural engineering). At the end of this section, experimental works on fines migration and gravel pack design (common in the field of petroleum engineering) are presented.

Skempton and Brogan (1994) used an experimental set-up (Figure 2-3) to study the piping phenomenon in sandy gravels. Piping refers to a state in which the velocity of the flowing fluid is high enough to wash the grains away from the main body of sand or soil and form a channel or pipe as a result, which can lead to instability and failure of structures. In this set-up, the inner diameter (ID) of the cylinder was 13.9 cm and the thickness of the sand sample was 15.5 cm. They compared the experimental values of critical hydraulic gradient (hydraulic gradient at which fines start moving) with the theoretical values and found out that grain size distribution plays a major role in the critical hydraulic gradients of sandy gravel samples.

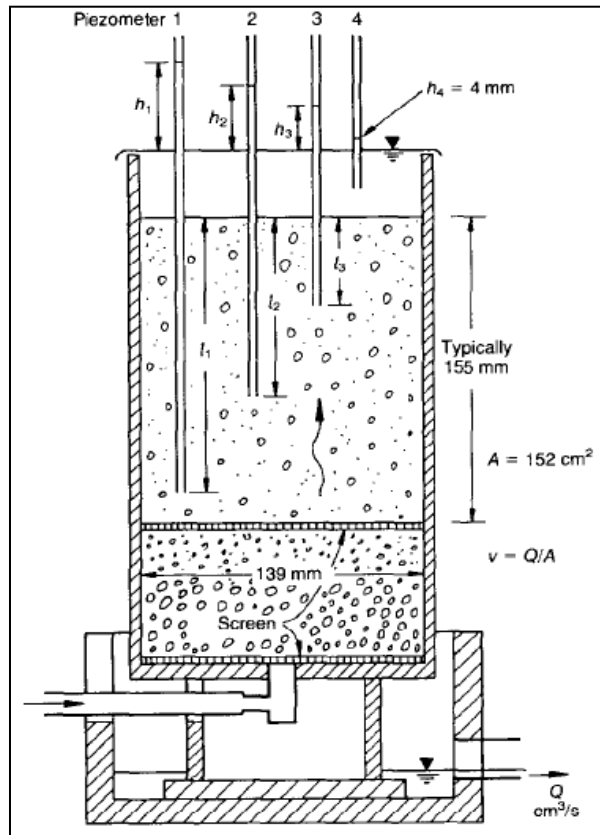


Figure 2-3: Experimental set-up used by Skempton and Brogan (1994)

Adel et al. (1994) developed a transport model which was used in the design of erosion-control filters. Such filters have application in coastal protection structures, storm-surge barriers and river embankments for erosion prevention purposes. In order to determine the model constants, an experimental set-up shown in Figure 2-4 was employed. Samples with different grain size distributions were subjected to different hydraulic gradients and the eroded sand/silt particles were collected downstream and weighed. These results were then used to calibrate the theoretical model. In a similar work, Adel et al. (1988) studied the stability of minestone filters. Such filters are widely used in slope protection applications along river banks and dikes. Because of wide grain size distribution of minestone, smaller grains can be easily washed out of the skeleton of larger grains. They developed a stochastic model to predict the mass of transported particles as a function of the fluid velocity within the filter. The model could predict the experimental results with reasonable accuracy. Worman and Olafsdottir (1992)

used a similar experimental and numerical approach to determine the transport rate of fine particles through coarse gravel layers.

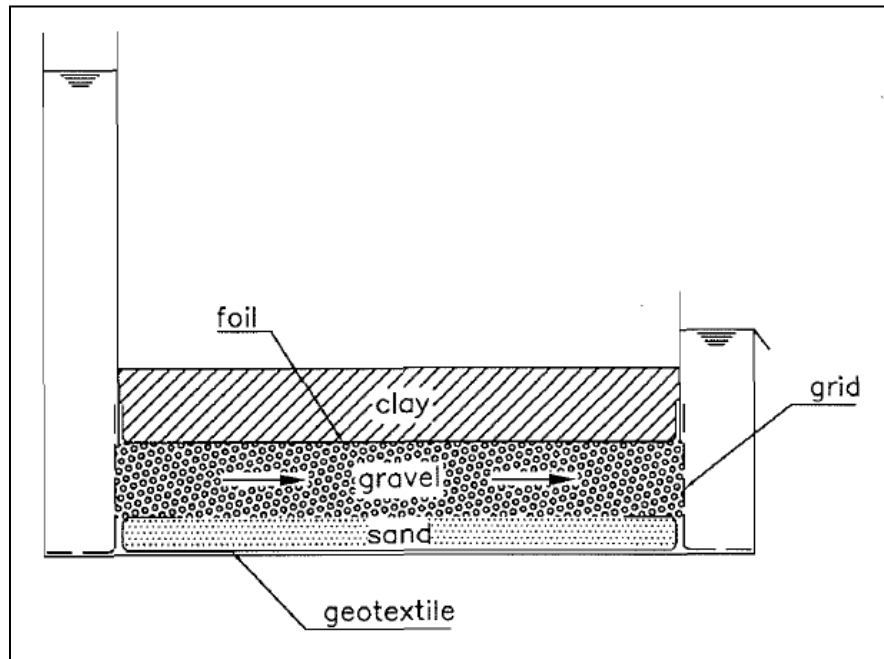


Figure 2-4: Experimental set-up used by Adel et al. (1994)

Wilhelm (2000) used a laboratory set-up shown in Figure 2-5 to study piping phenomenon in saturated granular media. In this figure, the cylinder that holds the test specimen is 52 cm high and has an inner diameter of 19 cm. Hydraulic gradient across the sample is controlled by a water reservoir with variable elevation. Wilhelm's work showed that classical two-component continuum porous media models are not able to describe the onset of piping in saturated sand-water mixtures properly. Thus, a new term accounting for the spatial distribution of porosity was introduced which resulted in better agreement with experimental data.

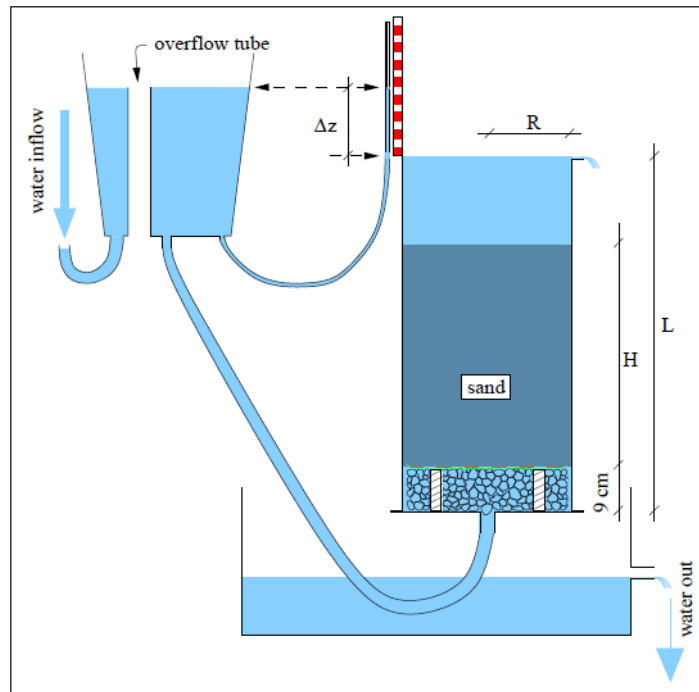


Figure 2-5: Experimental set-up used by Wilhelm (2000)

Sterpi (2003) conducted a series of internal erosion experiments on a well-graded silty-sand. In this work, the testing apparatus, which is shown in Figure 2-6, consisted of a permeameter in which the specimen was packed in seven layers. An upward fluid flow was induced through the specimen by applying different hydraulic gradients using an upper reservoir. Water and eroded particles were collected in a lower reservoir and the mass of eroded solids was measured at certain time intervals.

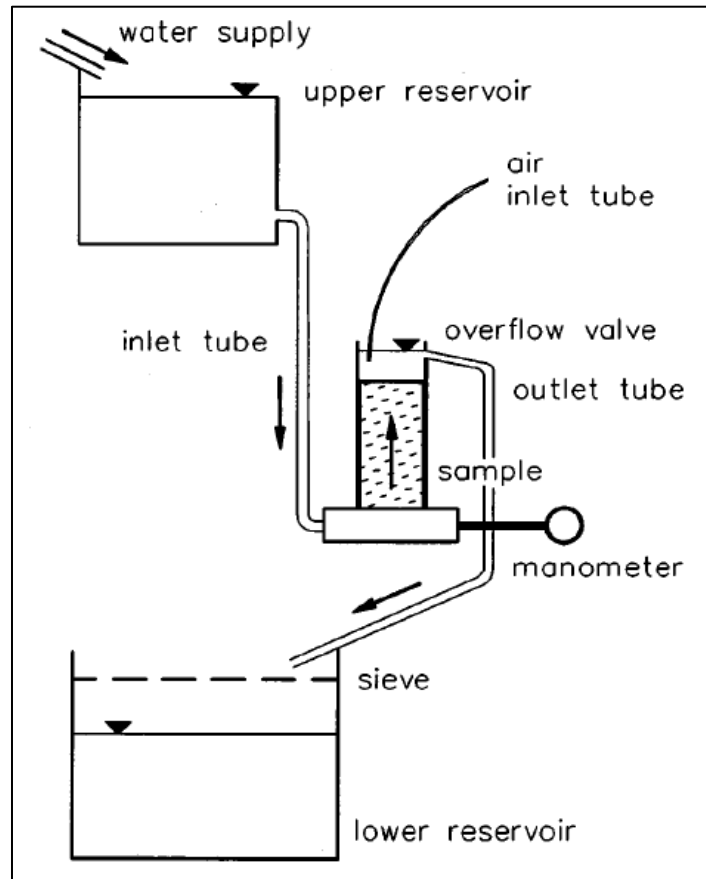


Figure 2-6: Experimental setup used by Sterpi (2003)

The tests were originally conducted to estimate the amount of eroded material in subsurface water tables under various hydraulic gradients and the results were used in a numerical model to estimate the subsequent surface subsidence for geotechnical assessments.

In addition to unconsolidated media, internal erosion tests have also been conducted on rocks. For example, Khilar and Fogler (1983) performed erosion tests on Berea sandstone cores. In these tests, the effect of water salinity on particle detachment and mobilization and its effect on the permeability of the rock were examined.

Similar experiments were conducted by Vaidya (1991) on Berea sandstone cores. In this work, the importance of water pH on release of particles and consequent permeability reduction was studied. The results showed that, in addition to water salinity, pH also plays an important role in the release of particles in pore

structure of the rock. A model was proposed to predict the permeability changes as a result of variations in fluid salinity and pH.

Selby and Ali (1988) conducted laboratory tests on sandstone cores to study the effect of internal erosion of fine particles on relative permeability of the rock. They performed two phase flow experiments on Berea sandstone and showed that increased water salinity, which promotes fines migration, can significantly reduce the relative permeability to oil.

Internal erosion experiments have also been conducted by researchers for design and optimization of gravel packs. Gravel packs are used in wellbores along with slotted liners and/or wire-wrapped screens, to prevent the production of sand particles with the formation fluid (Wilson 1933; Coberly 1937; Chenault 1938). The design criteria for gravel packs are very similar to those employed in design of geofilters (which are used in water dams and other earth structures). In this context, an ideal gravel pack allows the flow of the reservoir fluids and at the same time prevents the production of loose sand particles. The main challenge in the design of gravel packs is that they may get clogged over time and cause considerable reduction in wellbore productivity (Saucier 1974; Penberthy and Shaughnessy 1992).

An issue regarding the erosion experiments presented above is that they were mainly used for establishing the filter stability criteria or studying the mechanisms of fines migration and its effect on permeability reduction. Little attention has been given to quantification of the eroded mass or constitutive modeling of the erosion process.

2.4.2 Surface erosion experiments

Similar to internal erosion experiments, surface erosion experiments are also conducted on rocks and cohesionless porous media. This section provides a brief review on different forms of surface erosion experiments related to bridge, road and highway design (common in the field of geotechnical engineering) and sand production (common in the field of petroleum engineering).

Briaud et al. (2001) developed an experimental apparatus to measure the rate of surface erosion (scour) in fine and coarse grained soils. Field samples could be tested using this apparatus to estimate the rate of scour for different hydraulic shear stresses (fluid velocities). Such test results could be used in prediction of scour depth at bridge piers for various fluid velocities and times. Also, this apparatus made it possible to measure the critical shear stress necessary to start the erosion process. Experimental results showed that the critical shear stress is linearly related to the median particle diameter of the soil.

Indraratna et al. (2008) built an apparatus to measure the critical shear stress and the rate of surface erosion in chemically stabilized soils. Chemical stabilizers are used to increase erosion resistance of soils on road/highway embankments and other earth structures. They used cement and lignosulfonate as stabilizers and found out that lignosulfonate is more effective than cement in increasing the erosion resistance of the soil. Later on, Indraratna et al. (2013) developed an analytical model, based on principle of conservation of energy, to predict the erosion rate as a function of hydraulic shear stress. The model was validated using the experimental data obtained by Indraratna et al. (2008) and model predictions showed a good agreements with experimental data.

Papamichos et al. (2001) performed hollow cylinder tests on synthetic samples made of weak compactive sandstone and examined the effect of fluid flow rate and external stress on sanding rate. The samples had an external diameter of 20 cm and were 20 cm high. The diameter of the inner hole was 2 cm. The schematic of the test apparatus is shown in Figure 2-7. They also developed a numerical model for volumetric prediction of sand production. By comparing the experimental and numerical results, they showed that there is an extensive coupling between the poro-mechanical and erosion behaviour of the rock.

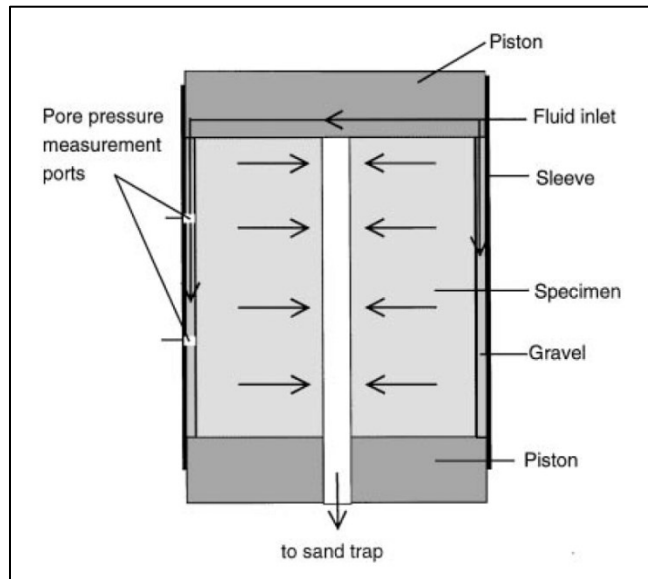


Figure 2-7: Schematic of the apparatus used by Papamichos et al. (2001)

To study the mechanisms of cold heavy oil production with sand (CHOPS), Servant et al. (2006) performed laboratory tests on cohesionless sand samples in a special odometer designed to simulate a producing sand layer (Figure 2-8). The apparatus was equipped with X-ray computer tomography to monitor, in real time, the initiation and propagation of the sanded zone. They used oil and water as the flowing fluids and found out that effective consolidation pressure along with porosity play a major role in the initiation of sanding and development of the sanded zone.

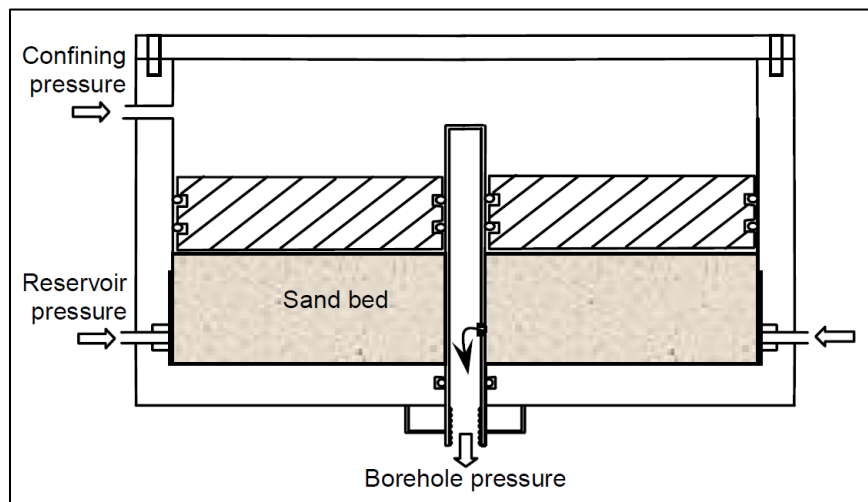


Figure 2-8: Schematic of the apparatus used by Servant et al. (2006)

2.5 Common constitutive laws for modeling the erosion phenomenon

Erosion constitutive law is a key component in the development of numerical models for the simulation of erosion in a porous medium. Constitutive laws for erosion accompany the law of conservation of mass for the solid phase. Depending on the degree of coupling between erosion, fluid flow and deformation behaviour of the porous medium, other constitutive laws may be required to address the possible interaction between these phenomena. In this section, we briefly review the common constitutive laws for the numerical modelling of internal and surface erosion. Emphasis is given to applications in the field of petroleum engineering.

Continuum erosion model, which is based on three phase mixture theory, was first introduced by Vardoulakis et al. (1996). They used the conservation of mass for solid, fluid, and fluidized solid phases along with Darcy's law and a constitutive law for mass generation with the following form:

$$\dot{m} = \rho_s \lambda (1 - \varphi) c \|\bar{q}_i\| \quad (2-1)$$

In Eq. (2-1), \dot{m} is the mass erosion rate, ρ_s is the grain density, λ is the erosion coefficient, φ is the rock porosity, c is the concentration of solids in the fluid phase, \bar{q}_i is the flow flux of the mixture of solids and fluid and $\|\cdot\|$ is a symbol representing Euclidean norm of a vector. The resulting system of equations was solved assuming 1-D radial fluid flow to study internal and surface erosion effects. The model can predict intermittent sand production events and it only focuses on the transport aspects of the erosion problem.

Stavropoulou et al. (1998) further developed the model by Vardoulakis et al. (1996) by accounting for rock degradation process. They also modified the constitutive laws for mass generation which enforces the sand production to stop after reaching critical sand concentration:

$$\dot{m} = \rho_s \lambda (1 - \varphi) \left(c - \frac{c^2}{c_{cr}} \right) \|\bar{q}_i\| \quad (2-2)$$

Here, c_{cr} is the critical saturation of the solid particles in the fluid phase. When the saturation of solid particles reaches its critical value, the rates of sand erosion and deposition become equal and the sand production process stops.

The erosion model was further modified by Papamichos et al. (2001) by coupling the poro-mechanical behavior of the fluid-rock system with erosion behavior of the rock. Mass generation constitutive law was a bit modified by dropping the concentration term for sake of simplicity:

$$\dot{m} = \rho_s \lambda (1 - \varphi) \|\bar{q}_i\| \quad (2-3)$$

In this work, sand production tests were conducted on hollow cylinder samples to calibrate model constants and numerical simulations were performed with various degrees of coupling between the poro-mechanical and erosion processes.

Later on, Papamichos (2010) modified the mass generation law to the following form:

$$\dot{m} = \rho_s \lambda \langle \|\mathbf{p}_i\| - p_{gcr} \rangle \quad (2-4)$$

In Eq. (2-4), p_{gcr} is the critical pressure gradient necessary to dislodge and mobilize the sand particles and $\|\mathbf{p}_i\|$ is the norm of pressure gradient vector. They extended the erosion model to account for the effect of water on rock's stiffness and degradation.

Constitutive laws given by Eq. (2-3) and (2-4) were used for numerical study of surface erosion. Fjaer et al. (2004) and Detournay et al. (2006) have used constitutive laws similar to Eq. (2-3) and (2-4) in their works.

Sterpi (2003) used a constitutive law for internal erosion which was obtained by fitting a curve to the experimental data. This constitutive law was used in a numerical model to estimate the surface subsidence due to internal erosion of soil particles in subsurface water tables. A similar approach was used by Cividini et al. (2009).

One of the main parameters appearing in the existing constitutive laws for particle erosion, is the erosion coefficient, λ , which has to be calibrated experimentally. However, in the literature, it is not clearly stated how λ is affected by or related to other parameters such as particle diameter, fluid velocity, fluid viscosity and porosity. Also, another limitation of the above constitutive laws is that they contain some intuitive assumptions without experimental evidence.

2.6 Summary

The erosion phenomenon has been studied in various engineering disciplines. In a broad point of view, erosion can be divided into two main categories of internal erosion and surface erosion. This topic has been studied by petroleum engineers since the 1930's. In the petroleum industry, the erosion phenomenon is of particular interest in the areas of fines migration and sand production. Fines migration and sand production phenomena can be distinguished based on the dominant forces driving the process, size ranges of the mobilized particles and production and operational consequences. Fines migration is usually considered in the context of formation damage and impaired reservoir productivity. Sand production is usually addressed for the operational problems that it causes such as damage to downhole tubular and equipment.

The erosion constitutive law is an important component in the numerical models for the simulation of solid erosion in porous media. A list of most common constitutive erosion laws was presented before. As mentioned above, an issue regarding the modeling of erosion phenomenon is that the common constitutive laws describing erosion in porous media [Eq. (2-1) to Eq. (2-4)] are partially based on intuitive assumptions and are not supported by experimental evidence. Therefore, one of the main goals of our research was to develop a constitutive law for internal erosion with the help of laboratory experiments. Due to lack of sufficient experimental data, we designed and set up an apparatus to conduct internal erosion experiments to generate enough data for the purpose of model development and calibration. Also, another issue with the current constitutive laws is that they don't address the relationship between the erosion coefficient and other parameters such as particle diameter, fluid velocity, fluid viscosity and

porosity. We have tried to address this issue as well in our research. Also, we tried to undertake more systematic approaches (such as dimensional analysis) towards the constitutive modeling of erosion. Further details are given in Chapters 3-5.

2.7 Nomenclature

c	Concentration of solids in fluid phase
c_{cr}	Critical concentration of solids in the fluid phase
\dot{m}	Mass erosion rate per unit volume
p_i	Pressure gradient vector
p_{gcr}	Critical pressure gradient
\bar{q}_i	Flow flux of the mixture of solids and fluid
λ	Erosion coefficient
ρ_s	Grain density
φ	Porosity
$\ \ \ $	Norm of a vector

2.8 References

- Adel, H. den, Bakker, K. J. and Breteler, M. K. 1988. Internal stability of minestone. Proc. Int. Symp. Modelling Soil-Water-Structure Interaction, pp. 225-231. Rotterdam: Balkema.
- Adel, H. den, Koenders, M. and Bakker, K.J. 1994. The analysis of relaxed criteria for erosion-control filters. Canadian Geotechnical Journal (CGJ), Vol. 31, No. 6, pp. 829-840.
- ASCE, 1936. Filter sand for water purification plants. Proc. ASCE, No. 62, pp. 1543-1580
- Baylis J. R., 1937. Experiences in filtration. J. of Amer. Water Works Ass., No. 29, pp. 1010-1048.
- Briaud, J.L., Ting, F. C. K., Chen, H. C., Gudavalli, R., Perugu, S. and Wei, G., 1999. SRICOS: Prediction of Scour Rate in Cohesive Soils at Bridge Piers,

- Journal of Geotechnical and Geoenvironmental Engineering, Vol. 125, No.4, pp. 237-246.
- Briaud, J. L., Ting, F. C. K., Chen, H. C., Cao, Y., Han, S. W., and Kwak, K. W. 2001. Erosion function apparatus for scour rate predictions. Journal of Geotechnical and Geoenvironmental Engineering, Vol. 127, No. 2, pp. 105–113.
- Chenault, R. L., 1938. Experiments on fluid capacity and plugging of oil-well screens, American Petroleum Institute, API-38-293.
- Cividini, A. and Gioda, G., 2004. Finite element approach to the erosion and transport of fine particles in granular soils. Int. J. Geomech., Vol. 4, No 3, pp.191–198.
- Cividini, A., Bonomi, S., Vignati, G.C. and Gioda G., 2009. Seepage-induced erosion in granular soil and consequent settlements. Int. J. Geomech., Vol. 9, No. 4, pp. 187–194.
- Coberly, C. J., 1937. Selection of screen openings for unconsolidated sands, American Petroleum Institute, API-37-189.
- de Gaauw, A., Van Der Meulen, T. and Van Der Does De Bye, M., 1984. Design Criteria for Granular Filters, J. Waterway, Port, Coastal, Ocean Eng. Vol. 110, No. 1, pp. 80-96.
- Detournay, C., Tan, C. and Wu, B., 2006. Modeling the mechanism and rate of sand production using FLAC, The 4th International FLAC Symposium on Numerical Modeling in Geomechanics, paper: 08-10.
- Fjaer, E., Cerasi, P., Li, L. and Papamichos, P., 2004. Modeling the rate of sand production, The 6th North America Rock Mechanics Symposium (NARMS), Houston, Texas, USA, June 5–9.
- Gruesbeck, C. and Collins, R. E., 1982. Entrainment and deposition of fine particles in porous media, Soc. Pet. Eng. J., pp. 847-856.
- Guo, S., Shao, Y., Zhang, T., Zhu, D., and Zhang, Y., 2013. Physical modeling on sand erosion around defective sewer pipes under the influence of groundwater, J. Hydraul. Eng., Vol. 139, No. 12, pp. 1247–1257.
- Indraratna, B., Muttuvel, T., Khabbaz, H. and Armstrong, R., 2008. Predicting the Erosion Rate of Chemically Treated Soil Using a Process Simulation

- Apparatus for Internal Crack Erosion, *J. Geotech. Geoenviron. Eng.*, Vol. 134, No. 6, pp. 837-844.
- Indraratna, B., Athukorala, R., and Vinod, J., 2013. Estimating the Rate of Erosion of a Silty Sand Treated with Lignosulfonate, *J. Geotech. Geoenviron. Eng.*, Vol. 139, No. 5, pp. 701-714.
- Iwasaki, T. 1937. Some Notes on sand filtration, *J. of Amer. Water Works Ass.*, Vol. 29, No. 10, pp.1591-1602.
- Kenney, T. C., and Lau, D., 1985. Internal stability of granular filters. *Can. Geotech. J.*, Vol. 22, No. 2, pp. 215–225.
- Khilar, K. C. and Fogler, H. S., 1983. Water sensitivity of sandstones, *Soc. Pet. Eng. J.*, Vol. 23, No. 1, pp. 55-64
- Khilar, K. C. and Fogler, H. S., 1987. Colloidally induced fines migration in porous media, *Rev. Chem. Eng.*, Vol. 4, No.1, pp. 43-67.
- Khilar, K.C., and Fogler, H.S., 1998, *Migration of Fines in Porous Media*. Kluwer Academic Publishers.
- Li, K., 2000. Fines migration and other aspects of recovery of crude oil by waterflooding, MSc thesis, University of Wyoming, USA.
- Muecke, T. W., 1979. Formation of fines and factors controlling their movement in porous media, *JPT*, pp. 144-50.
- Nguyen, V. T., 2012. Flow through filters in embankment dams, PhD thesis, University of Wolongong, Australia.
- Papamichos, E., Vardoulakis, I., Tronvoll, J. and Skjaerstein, A., 2001. Volumetric sand production model and experiment, *International Journal for Numerical and Analytical Methods in Geomechanics*, Vol. 25, No. 8, pp. 789-808.
- Papamichos, E. and Vardoulakis, I., 2005. Sand erosion with a porosity diffusion law, *International Journal of Computers and Geotechnics*, Vol. 32, No. 1, pp. 47-58.
- Papamichos, E., 2010. Erosion and multiphase flow in porous media. Application to sand production, Special issue of *European Journal of Environmental and Civil Engineering*, Vol. 14/8-9, pp. 1129-1154.

- Penberthy, W.L. Jr. and Shaughnessy, C.M., 1992. Sand control, Vol. 1, SPE Monograph Series, Richardson, Texas.
- Sakthivadivel, R. and Irmay, S., 1966. A review of filtration theories, HEL 15-4. University of California, Berkeley
- Sakthivadivel, R. 1967. Theory and mechanism of filtration of non-colloidal fines through a porous medium, PhD thesis. University of California, Berkeley
- Saucier, R. J., 1974. Considerations in gravel pack design, Journal of Petroleum Technology, Vol. 26, No. 2, pp. 205-212.
- Selby, R. J., and Ali, S. M. F., 1988. Mechanics of sand production and the flow of fines in porous media, Journal of Canadian Petroleum Technology, Vol. 27, No. 3, pp. 55-63.
- Servant, G., Marchina, P., Peysson, Y., Bemmer, E. and Nauroy, J., 2006. Sand erosion in weakly consolidated reservoirs: Experiments and numerical modeling, SPE/DOE Symposium on Improved Oil Recovery, Tulsa, OK, USA, April 22-26.
- Skempton, A. W. and Brogan, J. M., 1994. Experiments on piping in sandy gravels, Geotechnique, Vol. 44, No. 3, pp. 449-460.
- Skjaerstein, A., Stavropoulou, M., Vardoulakis, I., Tronvoll, J., 1997. Hydrodynamic erosion; A potential mechanism of sand production in weak sandstones, International Journal of Rock Mechanics and Mining Sciences, Vol. 34, No. 3-4, pp. 292.e1-292.e18.
- Stavropoulou, M., Papanastasiou, P., and Vardoulakis, I., 1998. Coupled wellbore erosion and stability analysis, Int. J. Numer. Anal. Meth. Geomech., Vol. 22, pp. 749-769.
- Sterpi, D., 2003. Effect of the erosion and transport of fine particles due to seepage flow. Int. J. Geomech., Vol. 3, No., 1, pp. 111-122.
- Vaidya, R. N., 1991. Fines migration and formation damage, PhD thesis, University of Michigan, USA.
- Vardoulakis, I., Stavropoulou, M. and Papanastasiou, P. 1996. Hydro-mechanical aspects of the sand production problem, Journal of Transport in Porous Media, Vol. 22, No. 2, pp. 225-244.

- Vaziri, H., Barree, B., Xiao, Y., Palmer, I., Kutas, M., 2002. What is the magic of water in producing sand, SPE Annual Technical Conference and Exhibition, San Antonio, Texas, USA, 29 September - 2 October.
- Veeken, C.A.M., Davies, D.R., Kenter, C.J., Kooijman, A.P., 1991. Sand production prediction review: developing an integrated approach, Proceedings of the SPE Annual Technical Conference and Exhibition, Dallas, Texas, USA. 6 – 9 October.
- Wan, C.F. and Fell, R., 2004. Investigation of erosion of soils in embankment dams, *J. Geotech. Geoenviron. Eng.*, Vol. 130, No. 4, pp. 373–380.
- Wilhelm, Th., 2000. Piping in Saturated Granular Media, Ph.D. Thesis, University of Innsbruck
- Wilson, C. S., 1933. Selection and use of screened pipe, *Transactions of the AIME*, Vol. 103, No. 1, pp. 116-135.
- Worman, A. and Olafsdottir, R., 1992. Erosion in a granular medium interface. *J. Hydraul. Res.*, Vol. 30, No. 5, pp. 639–655
- Wu, B., Tan, C. P., 2001. Effect of water-cut on sandstone strength and implications in sand production prediction. 38th U.S. Symposium on Rock Mechanics (USRMS), Washington D.C., USA, July 7-10.

Chapter 3

Constitutive Modeling of Internal Erosion in Porous Media Using Dimensional Analysis Technique

3.1 Introduction

Equations (2-1) to (2-4) are among the most popular forms of constitutive laws used in the literature for numerical modeling of internal and surface erosion processes. In these equations, the erosion coefficient, λ , is a calibration parameter; thus, it has to be determined experimentally. The common practice is to assign values of λ in a way that results a match between the numerical and experimental values of the eroded mass. The erosion coefficient, however, is not a constant and may be affected by variations in porosity, fluid viscosity and fluid velocity. In this chapter, we derived a modified constitutive law for internal erosion. This modified law relates the rate of erosion and fluid velocity through the erosion coefficient as a constant of proportionality. In the modified formulations, we propose that the erosion coefficient is a function of particle density, porosity variation, and a dimensionless parameter called particle Reynolds number. Data from a series of laboratory tests were used to infer the form of this relationship and for calibrating the model parameters. The experimental results show that the erosion coefficient

is directly related to the particle Reynolds number and inversely related to the porosity variation ($\varphi - \varphi_0$).

The proposed constitutive law for rate of erosion, \dot{m} , can be used in a numerical model along with the laws of conservation of mass for fluid and solid phases combined with the Darcy's law. The system of equation for an erosion problem, assuming steady state conditions, can be shown as follows:

$$v_{i,i} = 0 \quad (3-1)$$

$$v_i = -\frac{k}{\mu} p_{,i} \quad (3-2)$$

$$\rho_s \frac{\partial \varphi}{\partial t} = \dot{m} \quad (3-3)$$

Equation (3-1) is the conservation law for the fluid, Eq. (3-2) is Darcy's law and Eq. (3-3) is the conservation law for the solid. In equations above, v_i is the i^{th} component of fluid velocity vector, $p_{,i}$ is the i^{th} component of pressure gradient vector, k is intrinsic permeability, μ is fluid viscosity, ρ_s is grain density, φ is porosity and \dot{m} is erosion rate. The required equation to have an equal number of equations and unknowns in the above set of equations is the constitutive law for the rate of erosion, \dot{m} .

Additional conservation and constitutive laws need to be added to the system of equations if the effect of erosion process on the deformation behaviour of the porous medium is to be incorporated. If the effect of erosion process on the permeability is to be considered, an appropriate permeability law has to be added to the system of equations as well. It should be noted that \dot{m} in the above set of equations is tangent erosion rate but the model developed in this chapter is based on secant formulations. We have developed the same model using tangent formulations and the results are presented in Appendix A.

3.2 Mathematical modeling

In this section, first, the modified constitutive law for particle erosion rate in porous media is presented using the principles of dimensional analysis. Next, the formulation for calculating the critical fluid velocity, which is the minimum fluid

velocity required to initiate the erosion process, is derived based on analytical relations. Working on this model was a preliminary step towards the development of our main erosion model which we proposed in Chapters 5 and 6.

3.2.1 Modified erosion law

The purpose here is to quantify the amount of solid mass that is eroded in a porous medium with a certain grain density, porosity, and grain size distribution, when it is subjected to a flowing fluid of certain velocity and viscosity. Generally, it can be assumed that there is a lower bound for fluid velocity which we call “critical velocity”. The erosion process is expected to start only when the fluid velocity exceeds this lower limit.

The general form of the relationship between eroded mass and the rest of the parameters stated above can be shown in the following form:

$$m = f[(v_f - v_{cr}), D_p, \mu, \rho_s, (\varphi - \varphi_0), (t - t_0), V_{EB}] \quad (3-4)$$

where, m is the eroded mass, v_f is the apparent (Darcy) fluid velocity, v_{cr} is the apparent critical fluid velocity required to initiate the erosion process, D_p is the mean diameter of the *eroded* particles, μ is the fluid viscosity, ρ_s is the density of the eroded particles, $(\varphi - \varphi_0)$ is the difference between the new porosity and the initial porosity, t_0 is the time at which erosion starts, $(t - t_0)$ is the time elapsed after the start of erosion process and V_{EB} is volume of erosion boundary. Erosion boundary is defined as the zone in which the particles are mobilized and eroded out. In a numerical model, this could be the size of the numerical element. In an erosion experiment, V_{EB} could be considered as the volume of the test specimen. Such a zone experiences an increase in porosity as a result of the internal erosion process.

It should be noted that the internal erosion process is governed by the degree of uniformity of the particle assembly. In this process, finer particles are eroded and removed from the pore space formed by coarser particles. As a result, internal erosion is expected to occur only in poorly-graded assemblies of particles (assemblies with high coefficients of uniformity).

If the eroded mass is expressed as time rate and is normalized by the volume of erosion boundary, then Eq.(3-4) is reduced to:

$$m' = f[(v_f - v_{cr}), D_p, \mu, \rho_s, (\varphi - \varphi_0)] \quad (3-5)$$

where m' is the mass rate of eroded particles per unit volume. Since we use total eroded mass in Eq. (3-4), m' in the equation above is *secant* erosion rate per unit volume and is defined as follows:

$$m' = \frac{m}{(t - t_0) V_{EB}} \quad (3-6)$$

The reason for using secant erosion rate instead of tangent rate was to eliminate the effects of transient phenomena (such as pore clogging and unclogging) on the model calibration. Another method to lessen the effect of transient phenomena is to use a central difference scheme for calculating the erosion rate. This approach has been used along with the same procedure presented in this chapter, for the development of the erosion constitutive law based on tangent erosion rates and the results are presented in Appendix A.

The list of arguments in Eq. (3-5) has been selected based on the following criteria:

- **Dimensional requirements:** The dependent parameter in this model is the mass rate per unit volume. In order to make this parameter dimensionless, there should be parameters on the right-hand side with dimensions of mass, length, time or combinations of these dimensions. This requirement justifies the existence of $[(v_f - v_{cr}), D_p, \rho_s]$ or $[(v_f - v_{cr}), D_p, \mu]$ group of parameters on the right-hand side of this equation.
- **Physics of the problem:** Particle mobilization and erosion is due to the action of drag forces and kinetic forces of the flowing fluid. Parameters μ and $(v_f - v_{cr})$ represent these two forces, respectively.
- **Experimental and field observations:** Laboratory and field observations (Papamichos and Malmanger, 1999; Vardoulakis 2006) show that the rate of

erosion decreases with time. In other words, the larger the eroded mass, the lower the rate of erosion. Therefore, there is a relationship between the rate of erosion and the eroded mass. Since eroded mass is related to porosity changes through the law of conservation of mass, the parameter $(\varphi - \varphi_0)$ has been added to reflect this process.

Applying dimensional analysis technique to Eq. (3-5), it is desirable to gain some insight into the functional form of the relationship among the parameters.

There are six parameters in Eq. (3-5) but there are only three independent dimensions, namely; mass $[M]$, length $[L]$, and time $[T]$. Infinite number of dimensionless parameters can be formed using the parameters given in Eq. (3-5) but using the Buckingham's π theorem, only three of them will be independent (Hornung 2006).

Using the parameter listed in Eq. (3-5), the following relations are formed to represent the three standard physical measures when forming the dimensionless groups. Different combinations of these parameters can be used to form the basic standard measures but at the end, the resulting functional relationship can be reduced to the same form. Therefore, Eq. (3-7) through (3-9) are used to represent mass, length and time, respectively.

$$[\rho_s D_p^3] = [M] \quad (3-7)$$

$$[D_p] = [L] \quad (3-8)$$

$$\left[\frac{D_p}{(v_f - v_{cr})} \right] = [T] \quad (3-9)$$

Using the relationships above, the parameters in Eq. (3-5) are nondimensionalized one by one.

$$[m'] = [ML^{-3}T^{-1}] = \left[(\rho_s D_p^3)(D_p)^{-3} \left[\frac{D_p}{(v_f - v_{cr})} \right]^{-1} \right] = \left[\frac{\rho_s(v_f - v_{cr})}{D_p} \right] \quad (3-10)$$

$$[\mu] = [ML^{-1}T^{-1}] = \left[(\rho_s D_p^3)(D_p)^{-1} \left[\frac{D_p}{(v_f - v_{cr})} \right]^{-1} \right] = [\rho_s D_p (v_f - v_{cr})] \quad (3-11)$$

The third dimensionless parameter is selected to be $(\varphi - \varphi_0)$.

Using Eq. (3-10) and (3-11) and parameter $(\varphi - \varphi_0)$, Eq. (3-5) can be written in the following form:

$$\frac{D_p m'}{\rho_s (v_f - v_{cr})} = g \left[\frac{\rho_s D_p (v_f - v_{cr})}{\mu}, (\varphi - \varphi_0) \right] = g \left[\frac{G_s \rho_f D_p (v_f - v_{cr})}{\mu}, (\varphi - \varphi_0) \right] \quad (3-12)$$

where $g[\]$ denotes the function of the variables in the bracket. Reynolds number for a particle of diameter D_p is defined as follows (Charlez 1997):

$$Rp = \frac{\rho_f D_p v_f}{\mu} \quad (3-13)$$

Using Eq. (3-13), Eq. (3-12) can be shown as follows:

$$\frac{D_p m'}{\rho_s (v_f - v_{cr})} = g[G_s (Rp - Rp_{cr}), (\varphi - \varphi_0)] \quad (3-14)$$

where, G_s is the specific gravity of the particle; Rp is the particle Reynolds number and Rp_{cr} is the particle Reynolds number at critical fluid velocity. Eq. (3-14) can be further simplified into the following form:

$$m' = \frac{\lambda \rho_s (v_f - v_{cr})}{D_p} \quad (3-15)$$

where, λ is the erosion coefficient and is represented by the following equation:

$$\lambda = g[G_s (Rp - Rp_{cr}), (\varphi - \varphi_0)] \quad (3-16)$$

Eq. (3-15) can be compared to Eq. (2-1) and Eq. (2-3). It should be noted that the effect of porosity on erosion rate is absorbed into λ in the current work whereas in previous works, it is represented in the form of $(1 - \varphi)$. Also, v_f and \bar{q}_i are different notations representing the same parameter, i.e., apparent fluid velocity. We also can see that (3-16) has reduced a five-dimensional problem in Eq. (3-5) to a two-dimensional problem.

As per Eq. (3-16), erosion coefficient, λ , is proposed to be a function of particle specific gravity, particle Reynolds number and porosity. The precise functional form of this relationship will be determined experimentally.

The constitutive model offered for the erosion of solids in porous media, shown in Eq. (3-15) and Eq. (3-16), should satisfy the principle of conservation of mass. For the problem described at the beginning of this section, the principle of conservation of mass in *total* (not incremental) form can be simplified into the following equation:

$$\rho_s \frac{\Delta\varphi}{\Delta t} = m' \quad (3-17)$$

Where m' is the mass generation term and expresses *secant* erosion rate per unit volume. In Eq. (3-17) $\Delta\varphi$ and Δt are equivalent to $(\varphi - \varphi_0)$ and $(t - t_0)$, respectively.

3.2.2 Critical fluid velocity

Movement of a particle through a porous medium caused by a flowing fluid is governed by balance between the driving forces and the resisting forces. The driving forces are: 1) pressure gradient force and 2) drag force of the flowing fluid. The buoyant weight of particle can be either a driving or resisting force or it can be neutral depending on the direction of fluid flow with respect to gravity. The analytical derivation of the relationship pertaining to each one of the force components will be given below. An expression is derived based on the balance of these forces to calculate the critical fluid velocity required to initiate particle movement.

3.2.2.1 Pressure gradient force

Pressure gradient force in an arbitrary direction n , F_{pn} , exerted on an assembly of particles with volume, V , is given by the following formula (Detournay et al. 2006). Here, it is assumed that z is the vertical coordinate pointing upward, opposite to the direction of gravity:

$$F_{Pn} = -V \frac{d(p + \rho_f g z)}{dn} = -V \frac{d\Phi}{dn} \quad (3-18)$$

where Φ is fluid potential.

The volume V is comprised of n_p particles each having a volume V_p . Volumes V and V_p are related through porosity, φ . Substituting the equivalent terms in Eq. (3-18) yields:

$$F_{Pn} = -\frac{1}{1 - \varphi} \frac{d\Phi}{dn} \sum_{p=1}^{n_p} V_p \quad (3-19)$$

Knowing that the total pressure gradient force on volume V is the sum of the pressure gradient forces on individual particles each having volume V_p , the following relationship is used to represent the pressure gradient force on each particle in any direction n :

$$F_{PGn} = -\frac{V_p}{1 - \varphi} \frac{d\Phi}{dn} \quad (3-20)$$

3.2.2.2 Drag force

Drag force of a flowing fluid in direction n exerted on an immersed body can be computed using the following equation (Charlez 1997):

$$F_{Dn} = C_D A_{cs} \left(\frac{\rho_f v_{An}^2}{2} \right) \quad (3-21)$$

In Eq. (3-21), C_D is the drag coefficient which is a function of the Reynold's number, A_{cs} is the cross sectional area of the immersed body projected in the direction n , ρ_f is fluid density and v_{An} is the actual fluid velocity in the direction n . For spherical particles with diameter D_p and assuming laminar fluid flow conditions, Eq. (3-21) reduces to the following form (Asgian et al. 1995):

$$F_{Dn} = 3\pi \mu D_p v_{An} \quad (3-22)$$

where v_{An} is related to component of the apparent (Darcy) velocity, v_{fn} , through the following relationship:

$$v_{An} = \frac{v_{fn}}{\phi} = -\frac{k}{\mu\phi} \frac{d\Phi}{dn} \quad (3-23)$$

Here, k is the intrinsic permeability of the medium. Replacing Eq. (3-23) in Eq. (3-22) results:

$$F_{Dn} = -\frac{3\pi D_p k}{\phi} \frac{d\Phi}{dn} \quad (3-24)$$

3.2.2.3 Gravity force due to buoyant weight of the particle

The gravitational force in the direction n against particle movement, F_{Gn} exerted on a particle with volume V_p and density ρ_s submerged in a flowing fluid with density ρ_f is given by the following relationship:

$$F_{Gn} = (\rho_s - \rho_f)V_p g \cos \theta_n \quad (3-25)$$

where g is acceleration due to gravity and θ_n is the angle between the direction n and vertical upward direction. For vertical upward flow θ_n is zero, for horizontal flow, θ_n is 90° and for downward flow, θ_n is 180° . If fluid flow is upward, gravity resists erosion, if fluid flow is downward, gravity drives the erosion process and if fluid flow is horizontal, gravity is neutral towards the particle movement.

3.2.2.4 Erosion condition

It is assumed that particles will move in direction n when the sum of the driving forces on the particle in that direction is larger than the resisting forces. This assumption can be expressed in the following form:

$$F_{PGn} + F_{Dn} > F_{Gn} \quad (3-26)$$

Replacing Eq. (3-20), (3-24) and (3-25) in the inequality above and replacing $\frac{d\Phi}{dn}$ using Darcy's law, an expression is derived for the estimation of critical fluid velocity as follows:

$$v_{fn} > \frac{A}{B} = v_{crn} \quad (3-27)$$

where parameters A and B are given in Eq. (3-28) and (3-29), respectively.

$$A = (\rho_s - \rho_f)V_p g \cos \theta_n \quad (3-28)$$

$$B = \left(\frac{V_p \mu}{(1 - \phi)k} + \frac{3\pi D_p \mu}{\phi} \right) \quad (3-29)$$

Thus, in any direction n , the apparent fluid velocity, v_{fn} , has to exceed the critical velocity, v_{crn} , given in Eq. (3-27) for the erosion process to start.

It is worth noting that Eq. (3-27) only sets a lower bound for the initiation of particle mobilization. The fact of matter is that not all the particles which meet the criterion in Eq. (3-27) can be eroded. Some of the mobilized particles are redeposited along the way and another portion will be trapped behind pore throats that are smaller than their diameters (particle entrapment). Particle redeposition and particle entrapment are two well-known causes of diminishing erosion rates in the internal erosion process. The proposed model accounts for these processes by using a nonlinear erosion coefficient. More discussion will be provided in the model calibration section.

3.3 Experimental data

Data from a series of erosion experiments on a well-graded silty-sand were used to determine the functional form of the relationship in Eq. (3-16). Details of sample preparation and test procedures were reported in the paper by Sterpi (2003). In Sterpi (2003), the testing apparatus consisted of a permeameter in which the specimen was packed in seven layers. An upward fluid flow was induced through the specimen by applying different hydraulic gradients using an upper reservoir. Water and eroded particles were collected in a lower reservoir and the mass of

eroded solids was measured at certain time intervals. Grain size distribution of the test specimens is shown in Figure 3-1 and other relevant properties are given in Table 3-1. Figure 3-2 shows the results of erosion tests with five different hydraulic gradients. The results are reported as the percentage of eroded fines versus time. In this work, “fines” are defined as particles that can pass through the standard ASTM #200 sieve (with diameter of 0.074 mm). The samples in these tests had an initial fine content of 23% by weight (Figure 3-1). The tests were originally conducted to estimate the amount of eroded material in subsurface water tables under various hydraulic gradients and the results were used in a numerical model to estimate subsequent surface subsidence for geotechnical assessments.

In Table 3-1, permeability and hydraulic conductivity parameters are related to each other. The difference originates from different forms of Darcy’s law used in petroleum and geotechnical engineering. The relationship between these two forms of Darcy’s law is given in Eq. (3-30).

$$v_f = \frac{k |\Delta\Phi|}{\mu \Delta L} = \frac{k\gamma |\Delta h|}{\mu \Delta L} = \frac{k\gamma}{\mu} i = Ki \quad (3-30)$$

where k is the intrinsic permeability with the unit of area, $|\Delta\Phi|$ is difference of fluid potential across the sample, ΔL is the sample length, γ is the unit weight of the fluid, $|\Delta h|$ is the hydraulic head difference across the sample, K is hydraulic conductivity with unit of velocity, and i is hydraulic gradient which is a dimensionless parameter.

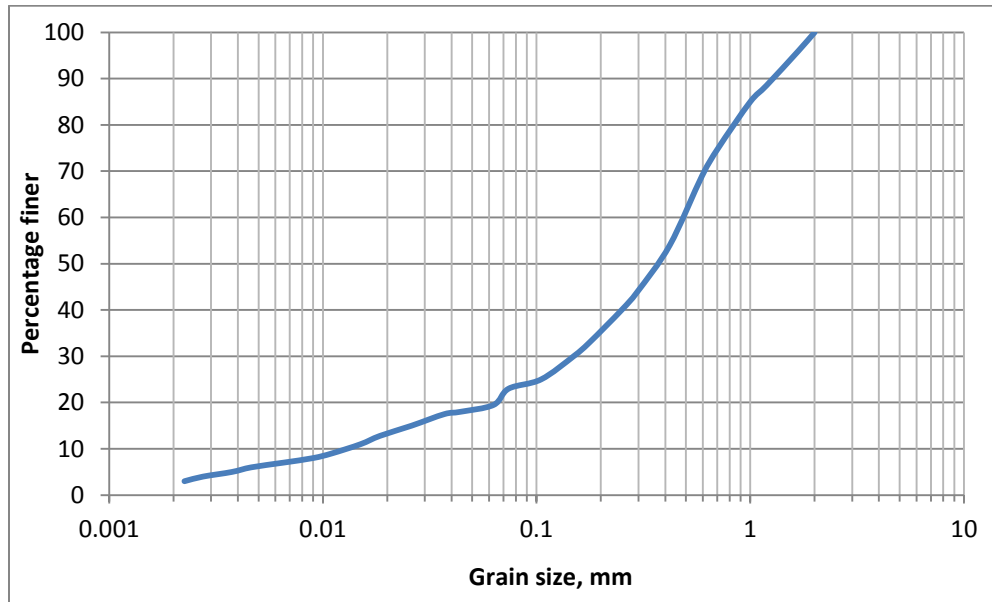


Figure 3-1: Grain size distribution for the silty-sand used for laboratory experiments, Sterpi (2003)

Table 3-1: Properties of the silty-sand used in the experiments by Sterpi (2003)

Parameter	Value
Sample diameter, m	0.07
Sample height, m	0.14
Initial porosity, φ_0	0.338
Specific gravity, G_s	2.72
Initial mass of sample, kg	0.97
Initial percentage of fine particles by weight, %	23
Hydraulic conductivity, K, m/sec	0.0001
Permeability, k, Darcy	10.33
Fluid viscosity, μ , Pa.sec	0.001

No appreciable change in permeability was reported during the testing except for Test 2 which showed an increase in permeability 5 hours after the start of the test (Figure 3-2). The constant permeability (with the exception of test 2) combined with the constant hydraulic gradient implies a constant fluid velocity during each test.

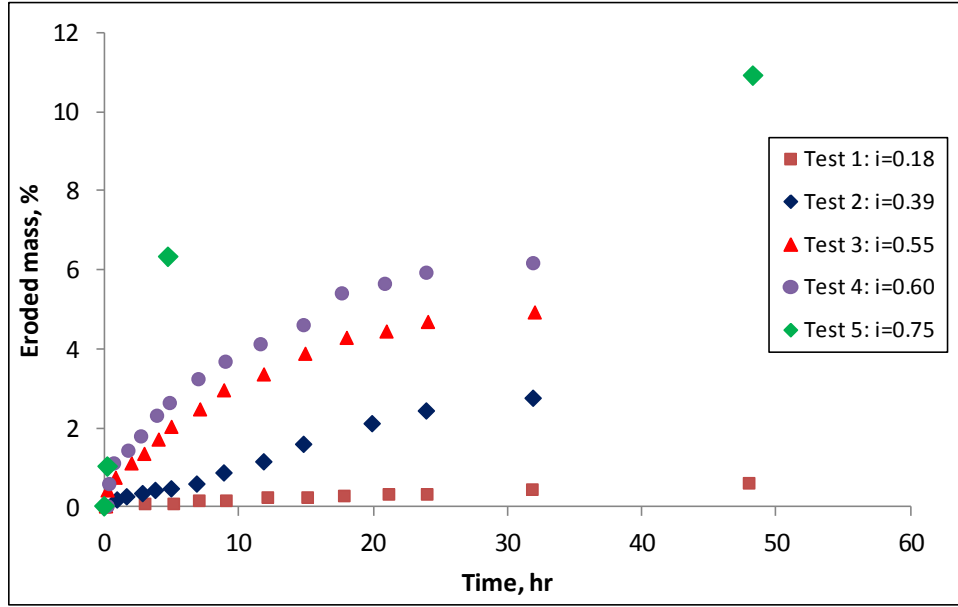


Figure 3-2: Results of erosion tests on silty-sand for different hydraulic gradients, Sterpi (2003)

3.4 Model calibration

The proposed constitutive law for internal erosion of particles in porous media is represented by Eq. (3-15) and (3-16). The purpose of this section is to offer a functional form for the erosion parameter (λ) given by Eq. (3-16). The actual functional form of λ is unknown but based on experimental observations (Figure 3-2), we know that λ is directly proportional to fluid velocity and inversely proportional to porosity change, $(\varphi - \varphi_0)$. In other words, a higher fluid velocity results in a higher value of λ and higher eroded mass [higher $(\varphi - \varphi_0)$] results in a lower λ value. Having these observations and using the approximation theory (David and Nolle 1982), the functional form of λ can be approximated using the equation below:

$$\lambda = \alpha \left[\frac{G_S(Rp - Rp_{cr})}{\varphi - \varphi_0} \right]^\beta \quad (3-31)$$

where α and β are dimensionless calibration parameters.

Let's define ω as:

$$\omega = \frac{G_s(Rp - Rp_{cr})}{\varphi - \varphi_0} \quad (3-32)$$

Then Eq. (3-31) can be simplified to:

$$\lambda = \alpha \omega^\beta \quad (3-33)$$

If we take the natural log of from both sides of Eq. (3-33), we have:

$$\ln \lambda = \ln \alpha + \beta \ln \omega \quad (3-34)$$

Therefore, if we plot $\ln \lambda$ versus $\ln \omega$, $\ln \alpha$ will be the intercept and β will be the slope of the line. Experimental data given in Figure 3-2 are used to estimate the values of α and β for each test. Using the data in Table 3-1 and Figure 3-2, the mass of eroded particles (silt and clay), m , can be calculated at any time for all tests, using the following formula:

$$m = p p_{if} m_t \quad (3-35)$$

where p is the percentage of eroded fine particles (Figure 3-2), p_{if} is the initial percentage of fine particles (Table 3-1) and m_t is the total mass of the test specimen (Table 3-1).

Next, the eroded mass is normalized by the volume of the sample and is plotted as a function of time. The secant slope of such a curve for each point, which is computed as the total eroded mass divided by total flow time, will give the values for m' . In Eq. (3-16), φ_0 is the initial porosity of the sample before the start of the erosion and φ is the porosity of the sample after the initiation of the erosion process. The difference between these two parameters is computed using the following relationship:

$$\varphi - \varphi_0 = \frac{m}{\rho_s V_t} \quad (3-36)$$

where m is the cumulative mass of eroded solids which is obtained from Figure 3-2, and V_t is the total volume of the sample. It should be noted that Eq. (3-36) is a special form of Eq. (3-17).

It is obvious that the diameter of the eroded particles must be smaller than the pore throats which they are moving through. According to the experimental work of Abrams (1977), the particles should have a diameter equal or smaller than one-third of the average pore throat size of the porous medium in order to be able to pass through the pore network without being entrapped. Therefore, the particle diameter D_p used in the calculation of the Reynolds number and critical fluid velocity is assumed to be the harmonic mean diameter of all particles smaller than 1/3 of the average pore throat size of the test specimen. The harmonic mean diameter is calculated using the method suggested by Kovacs (1981).

Different methods are available in the literature to estimate the average pore throat diameter of an assembly of particles based on the grain size distribution curve (e.g., Kovacs 1981; Uno et al. 1996). The average pore throat size of the test specimen, which is obtained using Figure 3-1 and the method suggested by Uno et al. (1996), has been computed to be around 14.5 microns. Therefore, D_p is assigned a constant value of 3.7 microns for all tests. As it was mentioned before, D_p is calculated as the harmonic mean diameter of all particles smaller than 1/3 of average pore throat size. Also, the critical fluid velocity is calculated using Eq. (3-27) by setting porosity equal to φ_0 and is assumed to remain constant for all tests. Since the fluid flow is in the upward direction, θ_n is set to zero in Eq. (3-28).

Based on the approach discussed above and by using Eq. (3-15) and Eq. (3-32), the corresponding values of λ and ω for each test can be obtained from the experimental data (Table 3-1 and Figure 3-2). Tests 1, 2 and 3 (with hydraulic gradients of 0.18, 0.39 and 0.55, respectively) were used to determine the material parameters and Tests 4 and 5 (with hydraulic gradients of 0.60 and 0.75, respectively) were used to validate the proposed model. Figure 3-3 through Figure 3-5 show the plots of $\ln \lambda$ versus $\ln \omega$ for Tests 1, 2 and 3, respectively.

In Figure 3-3 through Figure 3-5, the green diamonds represent experimental data and the solid line represents the best linear fit. For all the plots in this

chapter, linear regression lines were obtained using the method of least squares. The corresponding equation for the linear fit is also shown in these plots along with the value of coefficient of determination, R^2 . Also, in these figures, the upper-right data points correspond to the start of the test and lower-left data points correspond to the end of the test.

In Test 2, there was a sudden increase in fluid velocity after five hours (Sterpi 2003). Only data points up to five hours after the start of the test were used in the calibration of α and β (Figure 3-4). This is because we use the value of fluid velocity to calculate λ and ω but we don't have the value of velocity after five hours in this test.

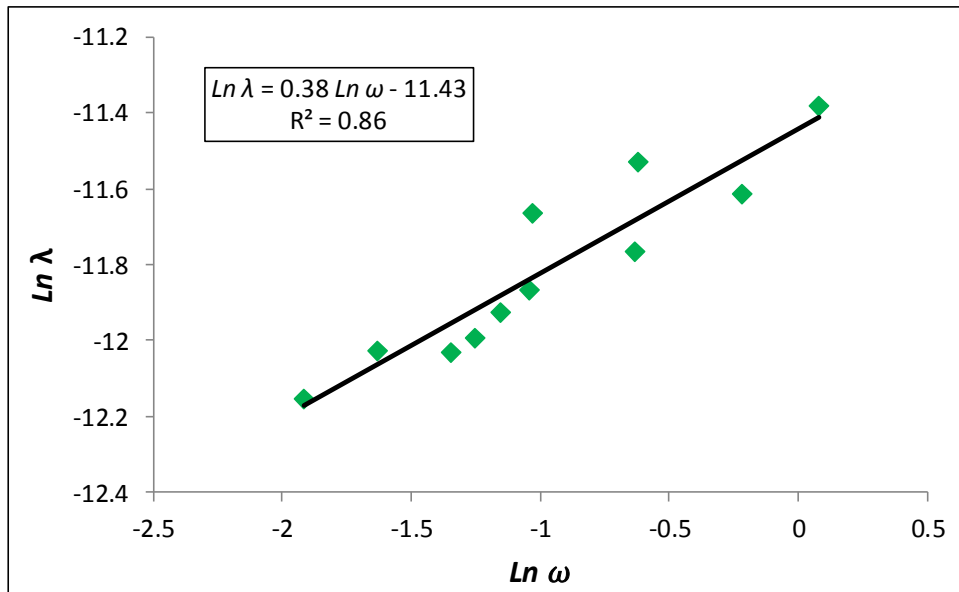


Figure 3-3: Calibrating model parameters for Test 1 ($i=0.18$)

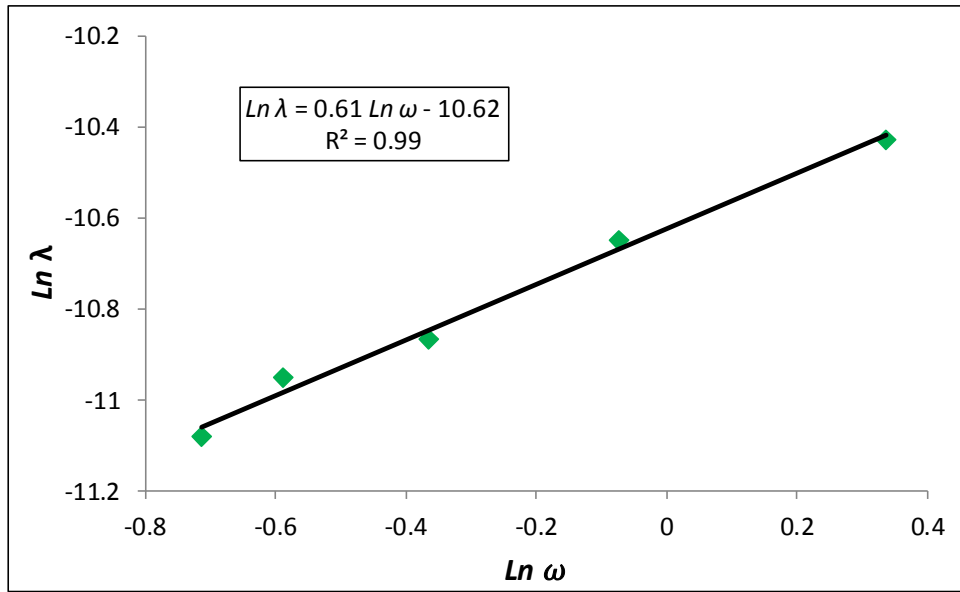


Figure 3-4: Calibrating model parameters for Test 2 ($i=0.39$)

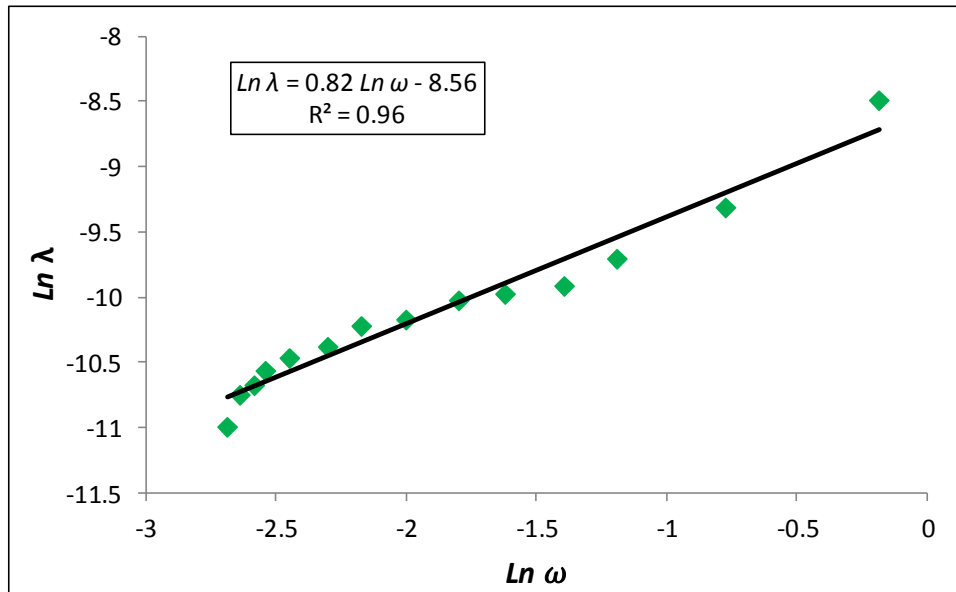


Figure 3-5: Calibrating model parameters for Test 3 ($i=0.55$)

As observed, the plot of $\ln \lambda$ versus $\ln \omega$ for these tests follows a linear trend.

Table 3-2 shows a summary of calibration parameters for Tests 1, 2 and 3.

Table 3-2: Summary of calibration parameters for Tests 1, 2 and 3

Test #	Hydraulic gradient	α	β
1	0.18	1.1E-5	0.38
2	0.39	2.4E-5	0.61
3	0.55	1.9E-4	0.82

After calibrating the erosion coefficient, λ , for each test, Eq. (3-15), Eq. (3-17) and Eq. (3-31) were used together to obtain an analytical relationship for the secant rate of erosion. After rearrangement and knowing that for secant erosion rate, $(\varphi - \varphi_0)$ and $\Delta\varphi$ are equivalent expressions, we have:

$$\frac{\Delta\varphi}{\Delta t} = \alpha \left[\frac{G_s(Rp - Rp_{cr})}{\Delta\varphi} \right]^\beta \frac{(v_f - v_{cr})}{D_p} \quad (3-37)$$

After simplification, an analytical relationship for porosity variation, $\Delta\varphi$, is obtained in the following form:

$$\Delta\varphi = \left[\frac{\alpha G_s^\beta (Rp - Rp_{cr})^\beta (v_f - v_{cr}) \Delta t}{D_p} \right]^{\frac{1}{(\beta+1)}} \quad (3-38)$$

By substituting Eq. (3-38) in Eq. (3-17), the following relationship is obtained for m' :

$$m' = \rho_s \left[\frac{\alpha G_s^\beta (Rp - Rp_{cr})^\beta (v_f - v_{cr})}{D_p} \right]^{\frac{1}{(\beta+1)}} \Delta t^{\frac{-\beta}{(\beta+1)}} \quad (3-39)$$

Data from Tests 1, 2 and 3 were used for model calibration and a summary of the calibrated parameters for these tests is given in Table 3-2. Comparisons between the experimental and calculated values of secant erosion rate for these 3 tests are shown in Figure 3-6 to Figure 3-8. In these figures, analytical values of erosion rate were calculated by using Eq. (3-39) and the data given in Table 3-1 and Table 3-2.

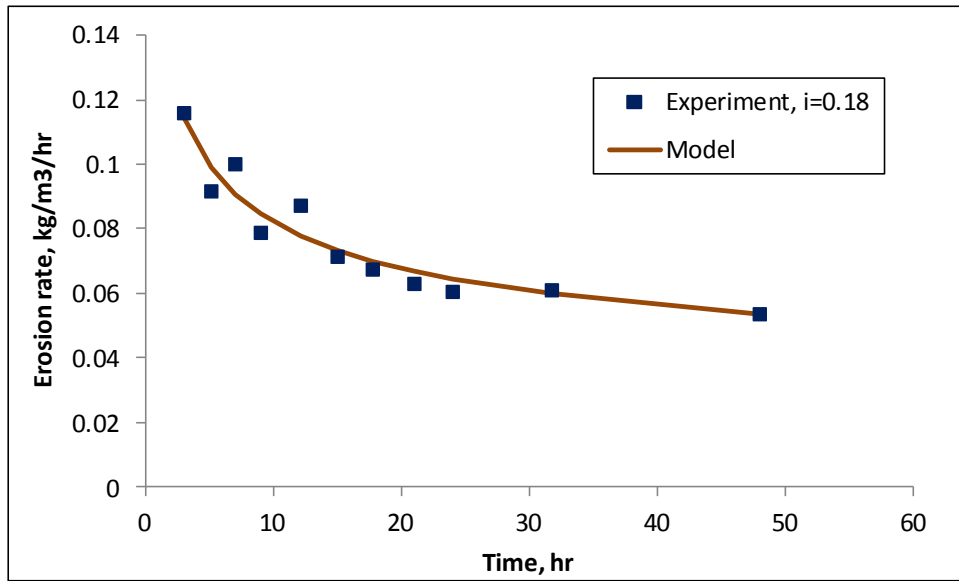


Figure 3-6: Comparison between experimental and calculated values of secant erosion rate, $i=0.18$

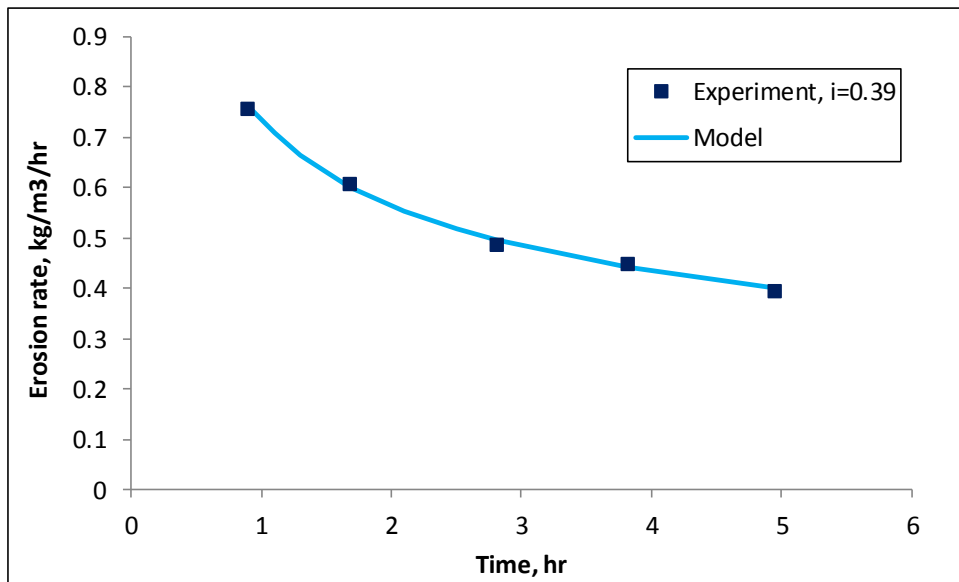


Figure 3-7: Comparison between experimental and calculated values of secant erosion rate, $i=0.39$

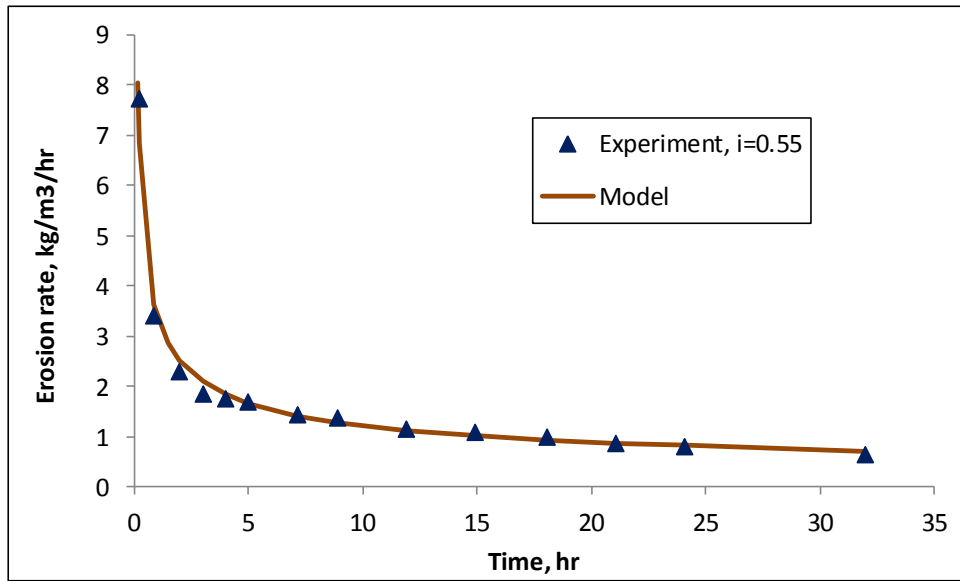


Figure 3-8: Comparison between experimental and calculated values of secant erosion rate, $i=0.55$

3.5 Model validation

Table 3-2 shows that α and β vary with hydraulic gradient. We used the data given in this table to examine the relationship between α and β and hydraulic gradient for Tests 1, 2 and 3 and the results are shown in Figure 3-9 and Figure 3-10.

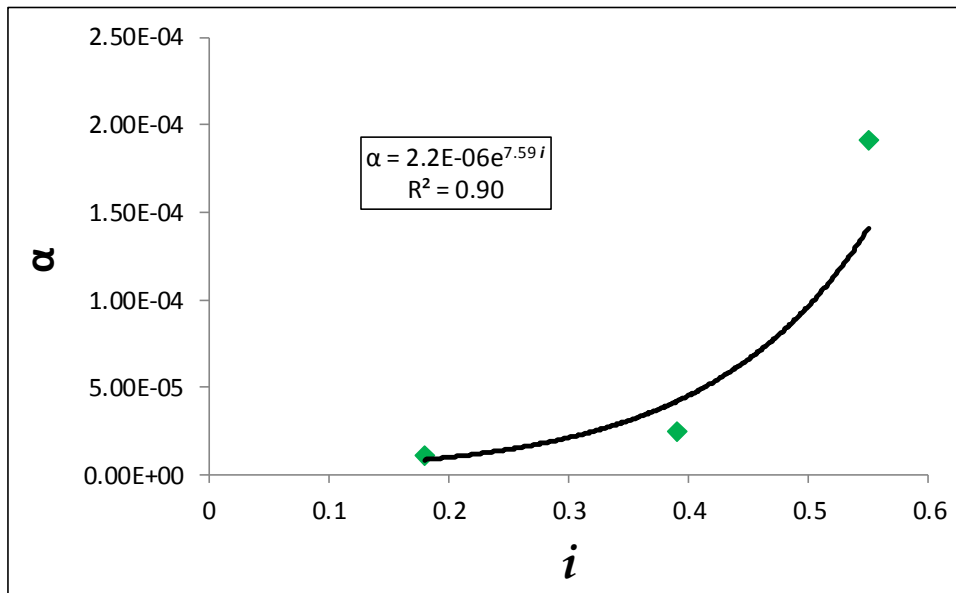


Figure 3-9: Variation of α with hydraulic gradient for Tests 1, 2 and 3 and best fit (solid line)

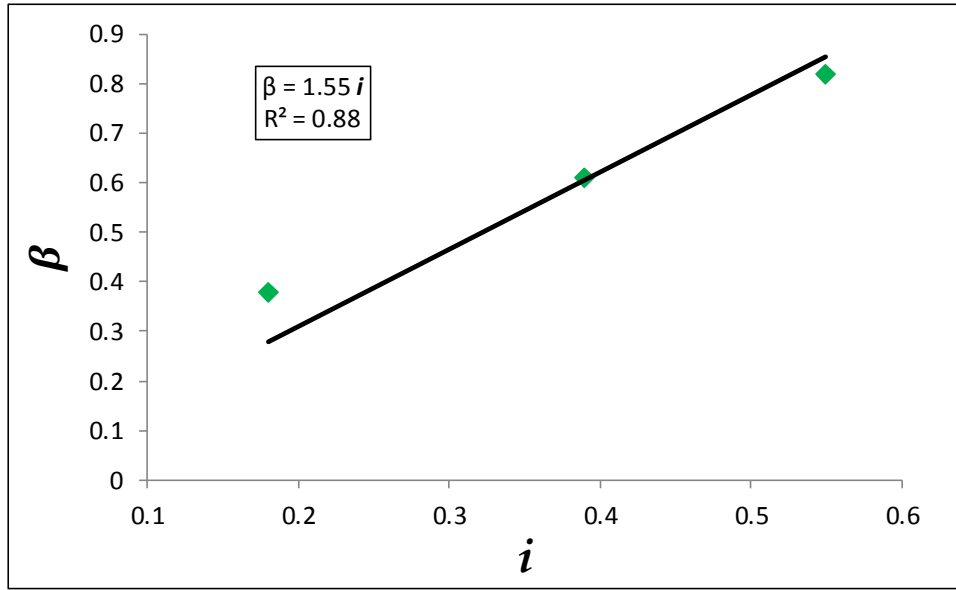


Figure 3-10: Variation of β with hydraulic gradient for Tests 1, 2 and 3 and best fit (solid line)

Figure 3-9 shows that α varies exponentially with hydraulic gradient and Figure 3-10 suggests that the relationship between β and hydraulic gradient is linear. Therefore, based on the trends observed in figures above, the following relationships are suggested for the variation of α and β with hydraulic gradient.

$$\alpha = \gamma_1 e^{\gamma_2 i} \quad (3-40)$$

$$\beta = \gamma_3 i \quad (3-41)$$

In Eq. (3-40) and Eq. (3-41), γ_1 , γ_2 and γ_3 are model constants which (based on Figure 3-9 and Figure 3-10) are calibrated to be 2.2E-6, 7.59 and 1.55, respectively.

The proposed analytical model, which is shown in Eq. (3-39) through (3-41), is validated by predicting the experimental results of Tests 4 and 5 (with the hydraulic gradients of 0.60 and 0.75, respectively). In the validation process, first the values of α and β for tests 4 and 5 were calculated by using the calibrated values of γ_1 , γ_2 and γ_3 in Eq. (3-40) and Eq. (3-41) and by using their corresponding hydraulic gradients. Table 3-3 shows a summary of calculated values of α and β for Tests 4 and 5. In this table, the calculated values of α and β were obtained by using Eq. (3-40) and Eq. (3-41).

Table 3-3: Calculated values of α and β for Tests 4 and 5

Test #	Hydraulic gradient	α	β
4	0.60	2.1E-4	0.93
5	0.75	6.5E-4	1.16

Next, values of secant erosion rate for these tests were calculated using Eq. (3-39) and the data given in Table 3-3. The comparisons between experimental and predicted values of erosion rate for these two tests are presented in Figure 3-11 and Figure 3-12, respectively. These figures show that the model predictions show a reasonable agreement with the experimental results.

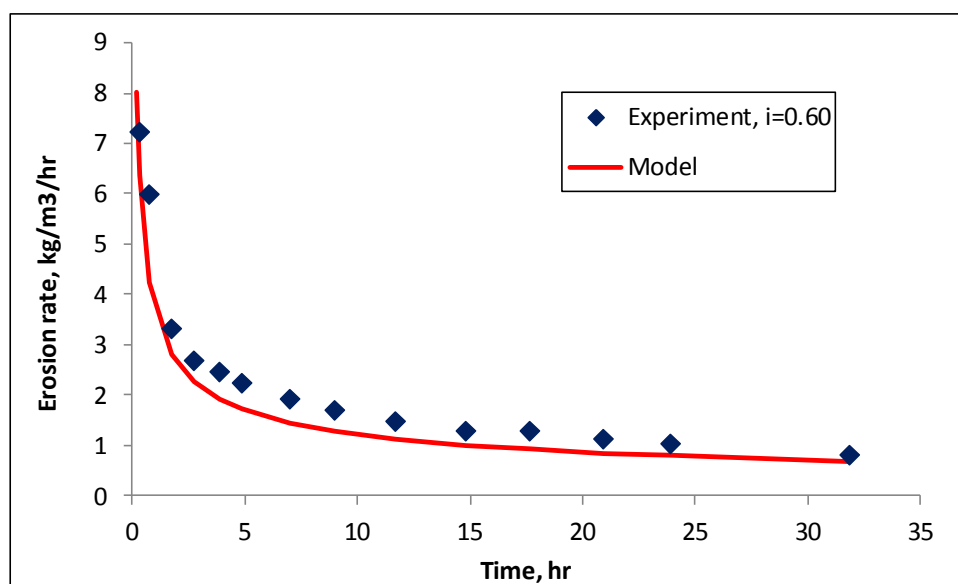


Figure 3-11: Comparison between experimental results and model prediction of secant erosion rate, $i=0.60$

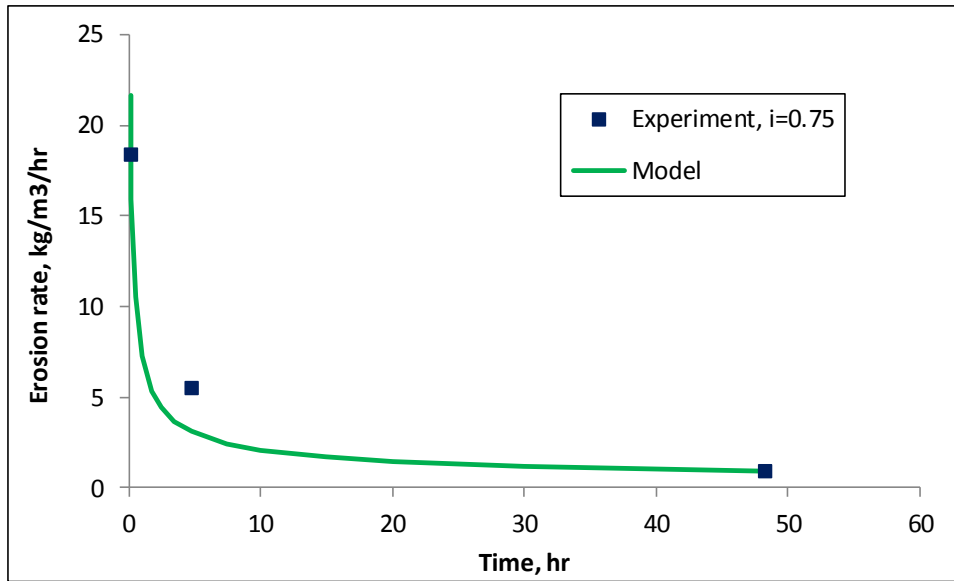


Figure 3-12: Comparison between experimental results and model prediction of secant erosion rate, $i=0.75$

3.6 Discussion and concluding remarks

Using the principles of dimensional analysis, an erosion model is proposed to calculate the rate of internal erosion in an assembly of particles. This model associates vanishing erosion rate to changes in porosity. In other words, for any given hydraulic gradient, there is only a portion of the particle assembly that is erodible. The porosity increases slowly as particles are being washed away to the point where the entire erodible portion has been eroded at which point internal erosion stops due to a couple of reasons. First, at a certain hydraulic gradient, hydrodynamic forces are only able to mobilize particles of a certain size. In a well graded assembly of particles, the lower the hydraulic gradient the smaller the percentage of erodible particles. This notion is equivalent to the concept of critical fluid velocity, which was discussed before. The second reason for the decreasing internal erosion rate can be related to the processes of particle redeposition and pore clogging which limit the available flow paths for loose particles to migrate.

One of the limitations of this model is that erosion is assumed to be uniform throughout the test specimen. In other words, this model assumes that porosity changes homogeneously in the test sample. However, it is very likely that erosion will be more intense close to the free surface of the test sample resulting in an

inhomogeneous porosity distribution. Erosion experiments on test specimens of different heights are required to assess the severity of this phenomenon and its effect on the test results and model predictions. To the best of our knowledge, such tests have not been performed so far.

Also, it was assumed in this work that the parameter D_p , which is the average size of the eroded particles, is constant for all hydraulic gradients. This may not be a realistic assumption since higher hydraulic gradients can mobilize larger size particles and generally, D_p can vary from one test to another. The reason for this assumption is that we do not know the value of D_p *a priori* unless we perform the erosion experiments and analyze the size of eroded particles. To overcome this limitation, a relationship can be established, experimentally, between fluid velocity (hydraulic gradient) and the average size of the eroded particles. The average size of eroded particles can be estimated by collecting all the eroded particles for each tests and by using an apparatus (such as a Coulter counter) to obtain the median size of the particles. Then such a correlation can be used to assign more realistic values of the D_p parameter in the proposed erosion model.

The advantage of the proposed model, shown in Eq. (3-15) and Eq. (3-31), is that it offers a functional form for the erosion coefficient. This functional form accounts for the effect of parameters such as grain specific density, particle Reynolds number and porosity variations on erosion coefficient, which had not been explicitly addressed in previous works. The proposed model has three calibration parameters [Eq. (3-40)-(3-41)] and is calibrated and validated using experimental data. The validation results show that the model is able to predict the erosion rates with reasonable accuracy.

3.7 Nomenclature

A, B	Parameters used to estimate critical fluid velocity
A_{cs}	Cross sectional area of an immersed body projected in the direction of flow
C_D	Drag coefficient
D_p	Particle diameter or average particle diameter

F_{Dn}	Drag force of fluid exerted on the particle in direction n
F_{Gn}	Resistive gravitational force in direction n
F_{PGn}	Pressure gradient force exerted on the particle in direction n
G_s	Specific gravity of the solid particles
i	Hydraulic gradient
k	Permeability
K	Hydraulic conductivity
m	Eroded mass
\dot{m}	Tangent erosion rate per unit volume
m'	Secant erosion rate per unit volume
m_t	Total mass of the test specimen
n	A symbol representing an arbitrary direction
n_p	Number of particles
p	Percentage of the eroded fine particles
p_i	i^{th} component of the pressure gradient vector
p_{if}	Initial percentage of the fine particles
Rp	Particle Reynolds number
Rp_{cr}	Particle Reynolds number calculated at critical fluid velocity
t	Time
t_0	Time at which erosion starts
v_{An}	Actual fluid velocity in direction n
v_{crn}	Critical fluid velocity in direction n
v_{fn}	Apparent (Darcy) fluid velocity in direction n
v_i	i^{th} component of the fluid velocity vector

V_{EB}	Volume of the erosion boundary
V_p	Volume of particle
V_t	Total volume of the sample
$\alpha, \beta, \gamma_1, \gamma_2, \gamma_3$	Dimensionless calibration parameters
Δh	Hydraulic head difference
ΔL	Sample length
θ_n	Angle between direction n and vertical upward direction
λ	Erosion coefficient
μ	Fluid viscosity
ρ_f	Fluid density
ρ_s	Grain density
Φ	Fluid potential
φ	Porosity
φ_0	Original porosity of the assembly of particles

3.8 References

- Abrams, A., 1977. Mud Design to Minimize Rock Impairment Due to Particle Invasion, JPT, pp. 586-592.
- Asgian, M.I., Cundall, P.A., and Brady, B.H.G., 1995. The mechanical stability of propped hydraulic fractures; a numerical study, J. of Pet. Tech., March, pp. 203-208.
- Charlez, Ph. A., 1997. Rock Mechanics: Petroleum Applications. Vol. 2, Editions Technip.
- David, F. W. and Nolle, H., 1982. Experimental Modelling in Engineering, Butterworths.
- Detournay, C. Tan, C., and Wu, B., 2006. Modeling the mechanism and rate of sand production using FLAC, The 4th International FLAC Symposium on Numerical Modeling in Geomechanics, paper: 08-10.

- Hornung, H., G., 2006. Dimensional Analysis: Examples of the Use of Symmetry, Dover publications, ISBN: 0486446050
- Kovacs, G., 1981. Seepage hydraulics, Elsevier Scientific.
- Papamichos, E., and Malmanger, E.M, 1999. A sand erosion model for volumetric sand predictions in a North Sea reservoir, SPE Latin American and Caribbean Petroleum Engineering Conference, Caracas, Venezuela, 21-23 April.
- Sterpi, D., 2003. Effects of the erosion and transport of fine particles due to seepage flow. *Int. J. Geomech.*, Vol. 31, pp. 111–122.
- Uno, T., Kamiya, K., Matsushima, T., 1996. The Relationships between Particle Size and Void Diameter for Sand, Proceedings of the Second International Geofilters Conference, pp. 67-74.
- Vardoulakis, I., 2006. Sand production, *Rev. Europ. de Génie Civil*, Vol. 10, No. 6-7, pp. 817-828.

Chapter 4

Experimental Investigation of Internal Erosion in Unconsolidated Porous Media

4.1 Introduction

This chapter contains the details of our experimental program. The specifications of the experimental apparatus and data acquisition methods are given first. Then, the details of preparation, packing and saturation of the test specimens as well as testing plan are explained. At the end, tests results and a brief discussion of the results are presented. It should be noted that internal erosion experiments can be conducted on both consolidated (rocks) and unconsolidated (soils/sands) porous media. Since the internal erosion mechanism is the same in both classes of porous media and due to simplicity of the required experimental apparatus, we decided to conduct our erosion experiments using unconsolidated test specimens.

4.2 Experimental set-up

Inspired by the experimental works explained in the literature review chapter, an apparatus was designed and set up to conduct erosion tests in unconsolidated porous media. Schematic and photograph of this apparatus are shown in Figure 4-1 and Figure 4-2 respectively. The main reason for conducting the erosion tests was that we couldn't find sufficient data in the literature about the mass of

the eroded particles and its variation with time, fluid velocity and grain size distribution.

The apparatus consists of a clear PVC cylinder 30 cm high with inner diameter (ID) of 15.24 cm (6 inches). A permeable gravel layer (aquarium gravel, 0.5-1 cm in average diameter) was placed at the bottom of the tube. The purpose of this layer, which was approximately 7 cm thick, was to slow down and distribute the incoming fluid flow across the cross section of the test specimen. The test specimen, which was 16 cm high, was placed on top of the gravel layer. The gravel layer and the test specimen were separated by an ASTM standard sieve #200 (with 0.074 mm opening diameter). A disk of filter paper with high permeability was placed on the wire mesh to prevent finer sand and silt particles from falling into the gravel layer. The inner diameter of the inflow line was 1 cm. Six outflow ports (each having 0.8 cm ID) directed the fluid and eroded particles out of the cylinder. The outflow ports were drilled at the same height and were 60° apart from each other around the periphery of the cylinder. Outflow ports were positioned at the top surface of the test specimen (see Figure 4-3) to facilitate the discharge of eroded particles and reduce the potential settlement of the particles due to the low vertical fluid velocity.

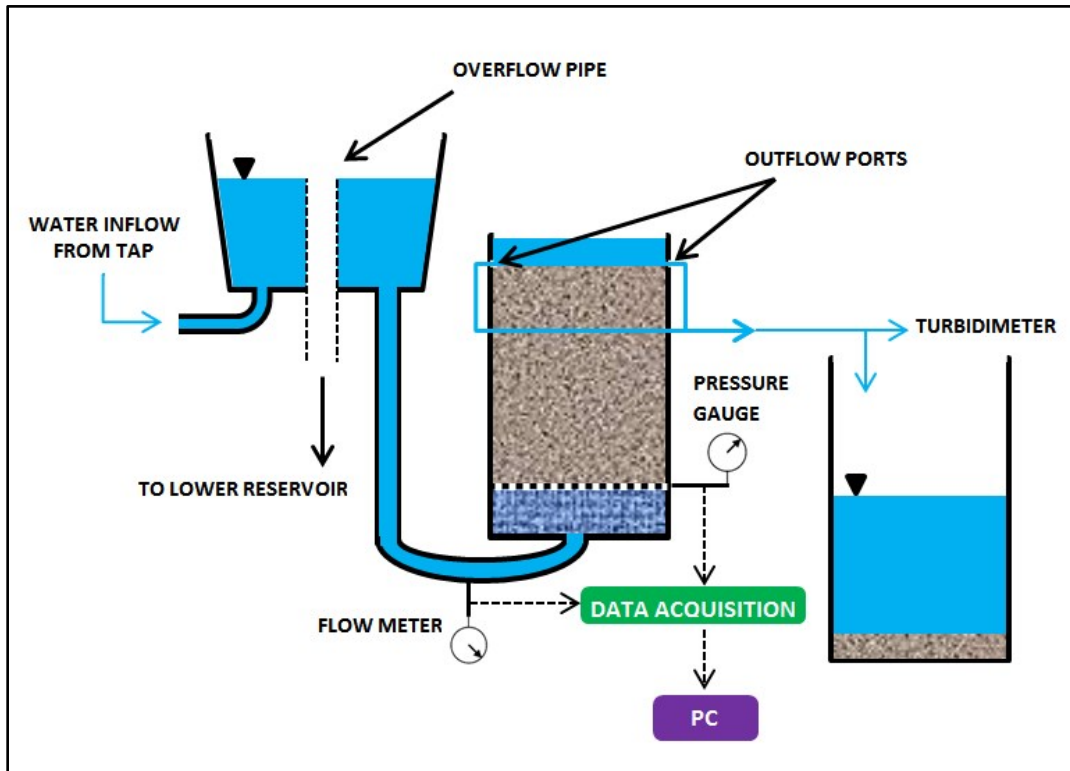


Figure 4-1: Schematic of the experimental set-up (not to scale)

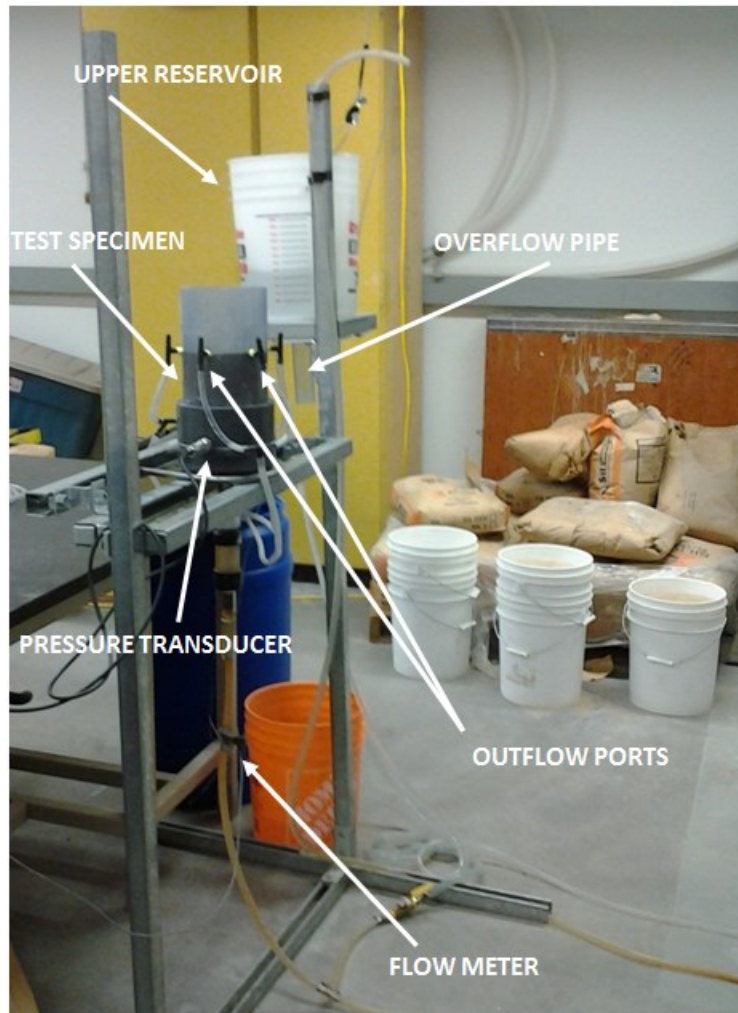


Figure 4-2: Photograph of the experimental apparatus

The outflow lines directed the fluid and eroded particles to a water tank where samples were taken for turbidity measurements.

Hydraulic gradient was generated in the test specimens by using an upper water reservoir which was placed on a metal frame. The height of this metal frame could be varied and, in this way, different hydraulic gradients were applied to test specimens. Tap water was continuously flowed to the upper reservoir. To keep the water level constant in the upper reservoir, an overflow pipe with an ID of 3.8 cm was placed at the center of the reservoir. The excess water in the upper reservoir was discharged through the overflow pipe into a lower reservoir.

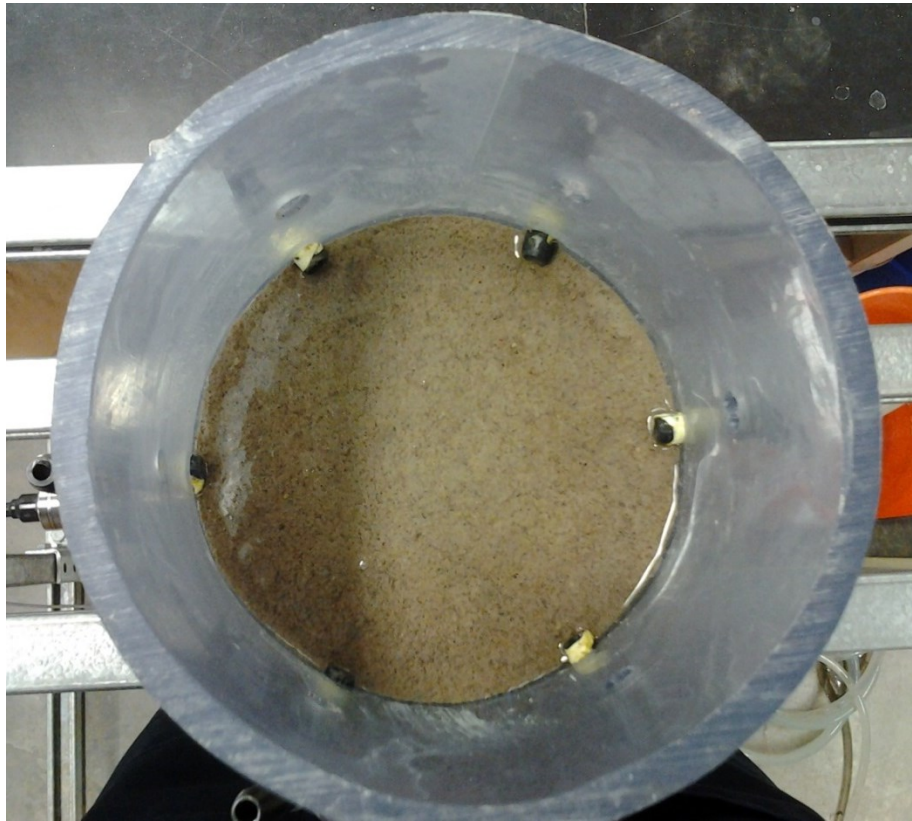


Figure 4-3: Position of outflow ports with relation to the test specimen

4.2.1 Data Acquisition

Fluid pressure, fluid flow rate and turbidity of the effluent were the main parameters recorded during each test. A manual portable turbidimeter (HF Scientific, Model DRT-15CE; see Figure 4-4) was used to measure the turbidity. Turbidimeters are used to measure the concentration of suspended particles in fluids. These devices employ a light source that shines a beam of light through the liquid sample contained in a vial. A light detector, which is usually placed at 90° to the light source, detects the light reflected by the suspended particles. The amount of light received by the light detector is used as a measure of solid concentration in the fluid. Turbidity is usually measured in Nephelometric Turbidity Units (NTU).

Since turbidimeters are sensitive to the shape, color and reflection properties of the suspended particles, it is necessary to calibrate the device for different types of materials separately to find the conversion factor from NTU to concentration.

Calibration of the turbidimeter for a specific material is done by creating solutions of known concentration values (by diluting a certain mass of the specific material in a certain volume of water). Then turbidity of these solutions is measured and corresponding values of turbidity and concentration are plotted against each other. The slope of such a line is the conversion factor for that type of material.

For the type of material used in our experiments, the calibration curve is shown in Figure 4-5. This calibration plot corresponds to the silt component used in the preparation of artificial test specimens. To calculate solid concentration from turbidity values, we used the conversion factor of $0.0022 \text{ kg/m}^3/\text{NTU}$.



Figure 4-4: Portable turbidimeter used in the experiments. Picture from manufacturer's website (<http://www.hfscientific.com>)

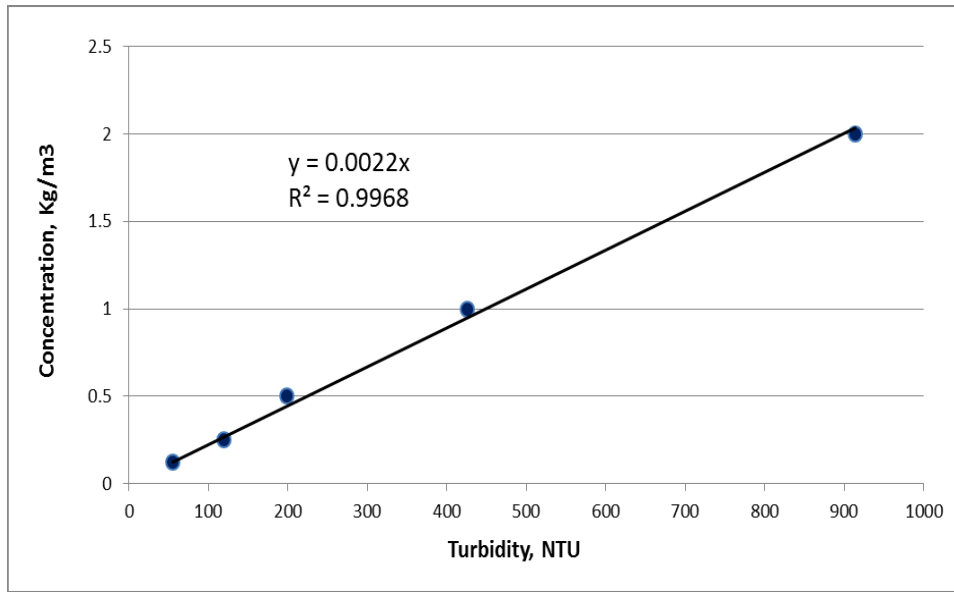


Figure 4-5: Calibration curve for the turbidity meter used in the experiments

The turbidimeter used in our experiments had three measuring ranges of 0-10 NTU with $\pm 1\%$ accuracy, 0-100 NTU with $\pm 5\%$ accuracy and 0-1000 NTU with $\pm 10\%$ accuracy. Repeatability of the device was $\pm 1\%$ of full scale for all measuring ranges.

To accurately measure the inflow fluid pressure, a pressure transducer (Omegadyne, Model PX309) was installed right under the wire mesh separating the gravel layer from the test specimen. The transducer had an operating range of 0-5 psig with $\pm 0.25\%$ of full scale accuracy. This device was calibrated using the data sheet provided by the manufacturer. To determine the pressure loss across the wire mesh and filter paper, which were placed under the test specimen, a test was conducted without having any specimen in the cylinder. The recorded pressure drop was negligible even for high flow rates.

Fluid flow rate was measured using an inline turbine flow meter (Omega, Model FTB-421). This device was installed on the water injection line into the specimen. The flow meter had an operating range of 0.1-2.5 lit/min with $\pm 3\%$ accuracy and $\pm 0.5\%$ repeatability for the full scale. This device was also calibrated using the data sheet provided by the manufacturer.

The pressure transducer and the flow meter were hooked up to a data acquisition device (National Instruments, Model USB-6009). Data from these devices were monitored and recorded through LabView SignalExpress software.

During each test, samples were collected from the outflow stream in certain intervals and their turbidity was determined in NTU. Then, the flow rate obtained from the flow meter and the conversion factor obtained from the turbidimeter calibration process were used to calculate the mass of the eroded particles for that time interval.

4.3 Test specimen preparation

Artificial samples used in our experiments were made by mixing different proportions of coarse sand, fine sand and silt. The corresponding grain size distribution (GSD) of each of these components is shown in Figure 4-6. In this figure, GSD of coarse and fine sands were obtained by routine sieve analysis and the GSD of the silt sample was obtained by the Hydrometer test following the procedure suggested in ASTM D422 Standard. Coarse and fine sand components had a density of 2650 kg/m³ and the silt component had a density of 1950 kg/m³.

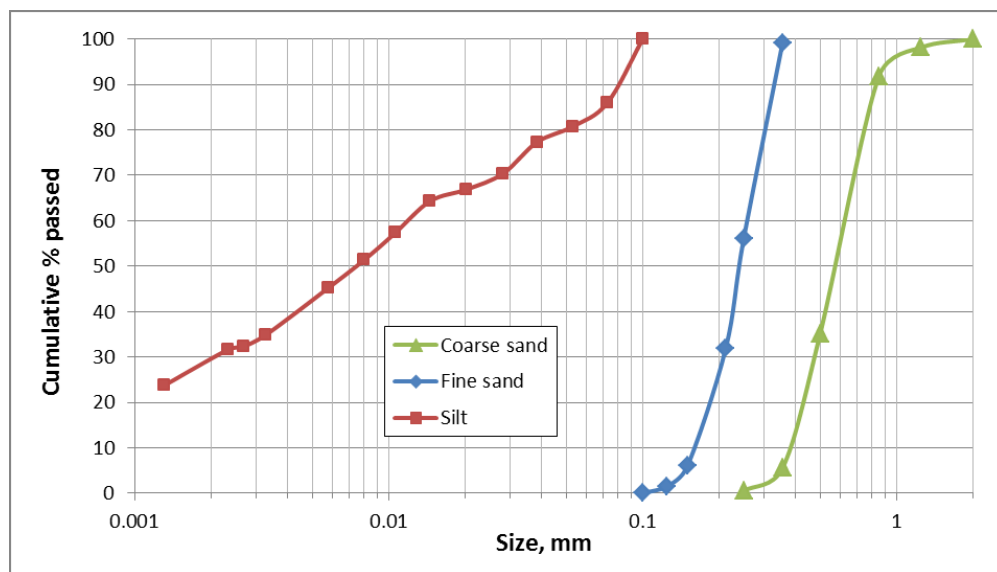


Figure 4-6: Grain size distribution of coarse sand, fine sand and silt, used to make artificial samples

Three different GSD's are designed to study the effect of GSD on the internal erosion behaviour of artificial sand pack samples. The properties of these grain size distributions are shown in Table 4-1. These GSD's were designed in a way to result a wide range for the coefficient of uniformity (from well-graded to poorly-graded samples). For the sake of brevity, these grain size distributions are referred to as GSD1, GSD2 and GSD3 throughout this chapter.

Table 4-1: Properties of the three GSD's used in the erosion experiments

GSD #	1	2	3
Coarse sand %	70	70	70
Fine sand %	15	20	25
Silt %	15	10	5
d_e^* , micron	17	24	41

In Table 4-1, d_e^* is the average pore throat diameter and is obtained using the following formula (Uno et al. 1996):

$$d_e^* = \frac{1}{2} \frac{\varphi}{1 - \varphi} D_w \quad (4-1)$$

In Eq. (4-1), φ is the porosity of the sand pack and D_w is the mean diameter of the particles calculated using the formula below:

$$D_w = \frac{1}{\sum \frac{\Delta S_i}{D_i}} \quad (4-2)$$

To use this method, the GSD of the material is usually divided into certain intervals. In Eq. (4-2), D_i is the average grain diameter for each interval and ΔS_i is the percentage by mass of the GSD in that interval. Further detail regarding this method can be found in Uno et al. (1996). As evident in Table 4-1, the percentage of coarse sand component is kept constant for all GSD' and only the percentage of fine sand and silt components are varied. The corresponding grain size distributions for GSD1, GSD2 and GSD3 are shown in Figure 4-7.

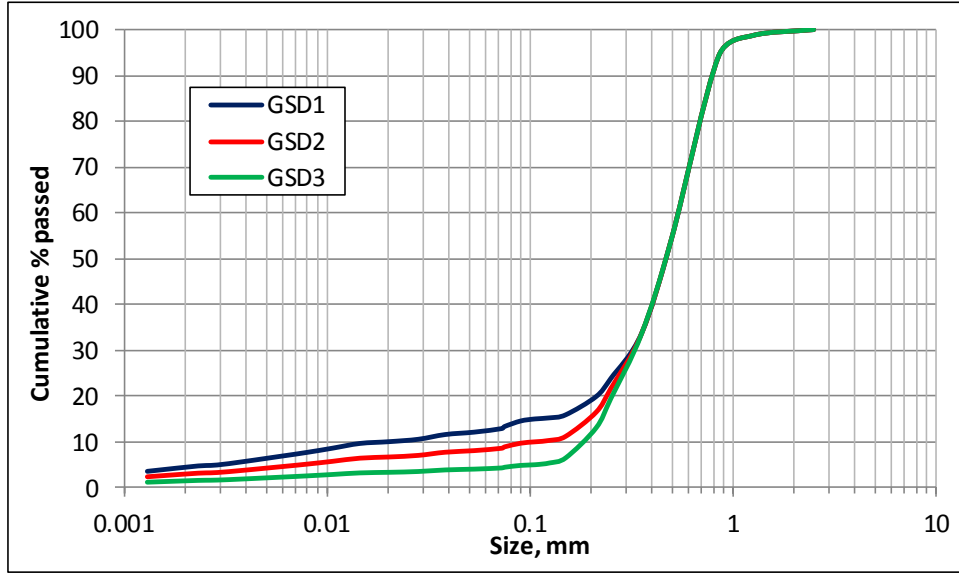


Figure 4-7: Grain size distribution of artificial test materials

Equivalent grain density for each GSD is calculated using the following formula:

$$\rho_{s,eq} = \frac{m_{cs} + m_{fs} + m_s}{V_{cs} + V_{fs} + V_s} = \frac{m_{cs} + m_{fs} + m_s}{\left[\frac{m_{cs}}{\rho_{cs}} + \frac{m_{fs}}{\rho_{fs}} + \frac{m_s}{\rho_s} \right]} \quad (4-3)$$

In Eq. (4-3), m_{cs} , m_{fs} and m_s are the mass of coarse sand, fine sand and silt, V_{cs} , V_{fs} and V_s are the volume of coarse sand, fine sand and silt and ρ_{cs} , ρ_{fs} and ρ_s are the density of coarse sand, fine sand and silt, respectively. For each GSD, we know the mass (Table 4-1) and density of each component and by using Eq. (4-3), the equivalent grain density is calculated for each GSD. All samples were given an initial porosity of 40%. Table 4-2 summarizes these data along with some other properties of the GSD's used in the experiments. In this table, mass of the specimens was obtained based on the calculated density [Eq. (4-3)] and an initial porosity of 40%. As mentioned earlier, all tests specimens had a diameter of 15.24 cm and a height of 16 cm.

Table 4-2: Properties of the test specimens used in the erosion experiments

GSD #	1	2	3
Initial porosity	40	40	40
$\rho_{s,eq}$, kg/m ³	2514	2558	2603
Mass of specimen, kg	4.40	4.50	4.55
C_u	27.4	5.2	3
C_c	9.1	1.8	1.1

In Table 4-2, C_u is coefficient of uniformity and C_c is coefficient of curvature and are defined in the following equations.

$$C_u = \frac{D_{60}}{D_{10}} \quad (4-4)$$

$$C_c = \frac{D_{30}^2}{D_{60} \times D_{10}} \quad (4-5)$$

In Eq. (4-4) and (4-5), D_{60} is a mesh opening that allows 60% of the material to pass through. Similar definitions apply to D_{10} and D_{30} . C_u and C_c are among very popular parameters in geotechnical engineering used to characterize a grain size distribution curve. These values in Table 4-2 were calculated using the data presented in Figure 4-7.

4.4 Test specimen packing method

Sand pack samples were prepared following the moist tamping procedure suggested by Ladd (1978). In this procedure, the sample is placed in several layers using the undercompaction technique. This method is employed to avoid over compaction of bottom layers while the upper layers are being compacted. The method prevents particle segregation and results in uniform and consistent test specimens with a uniform density along the height of the sample. To achieve this purpose, the layers at bottom are compacted to a lower density compared to layers

at top. The percent of undercompaction, U_n , for each layer is computed using the following formula:

$$U_n = U_{ni} - \left[\frac{(U_{ni} - U_{nt})}{n_t - 1} \times (n - 1) \right] \quad (4-6)$$

In Eq. (4-6), U_n is the degree of undercompaction for the n^{th} layer, U_{ni} is the degree of undercompaction for the first layer, U_{nt} is the degree of undercompaction for the last layer and n_t is the total number of layers. U_{ni} can vary between 0% for very dense specimens and 15% for very loose specimens and U_{nt} is usually set to zero. The height of the sample at the end of n^{th} layer, h_n , is calculated using the following formula:

$$h_n = \frac{h_t}{n_t} \left[(n - 1) + \left(1 + \frac{U_n}{100} \right) \right] \quad (4-7)$$

In Eq. (4-7), h_n is the height of sample at the end of n^{th} layer and h_t is the total height of the test specimen.

In our experiments, U_{ni} was selected to be 7.5%. Test specimens had a height of 16 cm and a diameter of 15.24 cm and were placed in seven layers. In the compaction method suggested by Ladd (1978), the degree of initial saturation was recommended to vary from 20% to 70%. An initial saturation of 40% was used for our tests. Because of different average grain density for different GSD's in our experiments, the dry mass was calculated for an initial porosity of 40% for all tests (Table 4-2). For each test specimen, the dry mass of each component (coarse sand, fine sand and silt) was calculated based on the data from Table 4-1 and Table 4-2. Then the dry components were added to each other and were well mixed. Next, the required mass of water (based on data from Table 4-2 and an initial saturation of 40%) was added to the dry mix and well mixed to achieve a uniform saturation in the sample. Then, the test specimen was placed in the test cylinder according to the procedure explained above. A flat bottom tamper was used to apply tamping and flatten each layer after placement.

Before starting the tests, all the flow lines were filled and all air bubbles were driven out. Also, the gravel layer at the bottom of the cylinder was fully saturated. The filter paper was also soaked before being placed on the wire mesh which separated the gravel layer and test specimen. Also, as shown in Figure 4-1, during the tests, the injected water was drained from the bottom of upper reservoir to exclude the possibility of trapped air bubbles being injected into the test specimen.

4.4.1 Sample saturation

Before applying the hydraulic gradient, the samples were saturated at a constant fluid flow rate. While saturating, it is important to avoid any disturbance to the pore structure of the samples. Also, the saturation flow rate had to be selected in a way to lower the possibility of fluid fingering and channeling to ensure a uniform saturation across the cross section and height of the sample. Given these requirements and using the experience obtained from several trial tests, the saturation flow rate was selected to be about 20 cc/min.

4.5 Testing plan

The internal erosion tests were carried out according to the plan in Table 4-3. Before carrying out the main tests, a multitude of trial tests were carried out for tuning the apparatus and calibrating the devices used in the experiments. Also, the trial tests results were used to select the initial saturation, saturation flow rate, and hydraulic gradients.

Table 4-3: Testing plan

Test #	1	2	3	4	5	6	7	8	9
Gradient	i_1	i_2	i_3	i_2	i_3	i_2	i_3	i_2	i_2
GSD	GSD1	GSD1	GSD1	GSD2	GSD2	GSD3	GSD3	GSD1	GSD2

The values of hydraulic gradients i_1 , i_2 and i_3 were selected to be 0.30, 0.50 and 0.70 respectively. Higher hydraulic gradients were not used to avoid the risk of piping and sample fluidization. Hydraulic gradient i_1 was only used with GSD1 due to its high permeability and was not applied to GSD2 and GSD3 because it

wouldn't generate considerable flow rates and erosion, within the time frame of the experiments (please refer to test results).

Test repeatability is part of any experimental investigation to ensure reliability of the apparatus and consistency of the testing procedures. In this work, test repeatability was examined for GSD1 and GSD2 at a hydraulic gradient of 0.7. As shown in Table 4-3, Test #8 was a repetition of Test #2 and Test #9 was a repetition of Test #4.

4.5.1 Trial tests

A series of erosion tests was conducted on the fine sand component (Figure 4-6) and the result is shown in Figure 4-8. This figure shows the recorded fluid velocity as a function of applied hydraulic gradient. The tests were carried out for six different hydraulic gradients ranging from 0.17 up to 0.78. No particle erosion was observed for any of the tests. The solid line in this figure shows the best linear fit (which is obtained using method of least squares) the slope of which is the hydraulic conductivity of the material. The hydraulic conductivity of this material was estimated to be around 0.6 mm/sec which is equivalent to 62 Darcy. Due to piping and fluidization, no gradients above 0.78 were applied to the test specimens. The maximum flow rate in this test (corresponding to gradient of 0.78) was 0.53 lit/min and the minimum grain size in the sand pack was about 100 microns. Therefore, it was concluded that the sand particles would not be mobilized even for the highest applied gradient. In this way, it was ensured that there was no possibility for the occurrence of surface erosion and that internal erosion remained the dominant form of erosion in the main experiments. Based on these results, it was decided to use 0.70 as the maximum value of the applied hydraulic gradients in the main tests to avoid the possibility of fluidization.

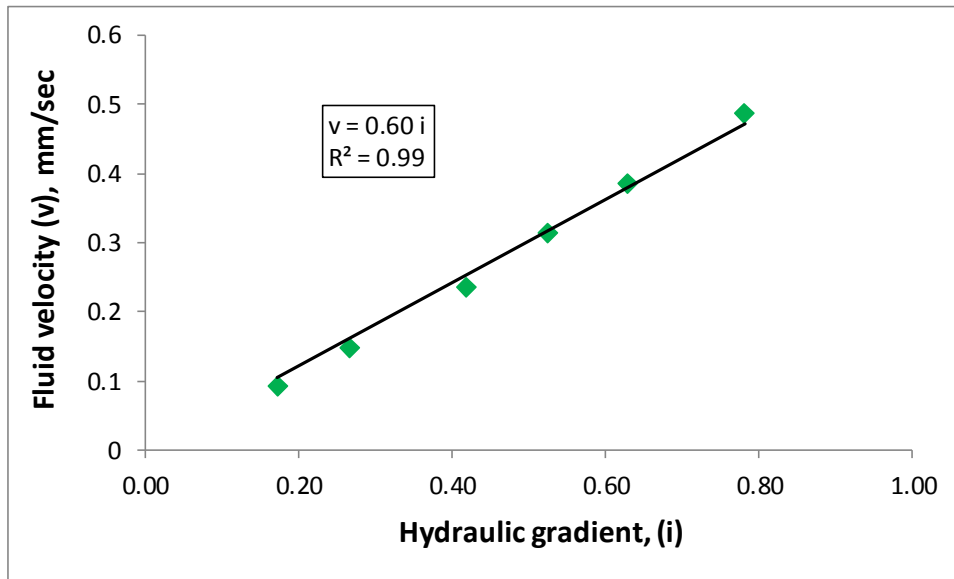


Figure 4-8: Fluid velocity vs. hydraulic gradient for fine sand component

Another series of trial tests were conducted to determine the critical hydraulic gradient required to initiate particle erosion. In these tests, particle erosion was observed for hydraulic gradients as low as 0.05. Having this observation and knowing that our test specimens (Figure 4-7) have between 1.5% to 5% clay content (particles with a diameter of 2 microns or smaller), it seemed reasonable to assume that particle erosion will happen for any non-zero hydraulic gradient.

4.6 Results of main erosion tests

The erosion tests were carried out according to the testing plan discussed in the previous section. As mentioned before, two of the tests were repeated to verify the accuracy of the measurements and consistency of sample making and test execution. In this section, first, the results of test repeatability examination are discussed. Next, the results of the main experiments (Tests #1 to #7) are presented.

4.6.1 Test repeatability

Test repeatability was examined for GSD1 and GSD2 at a hydraulic gradient of 0.7. For these tests, all the material and test parameters were the same. The eroded mass and permeability for each GSD are compared and the results are

presented in Figure 4-9 to Figure 4-12. In these figures, the legend shows the GSD number, the applied hydraulic gradient and the test number, respectively.

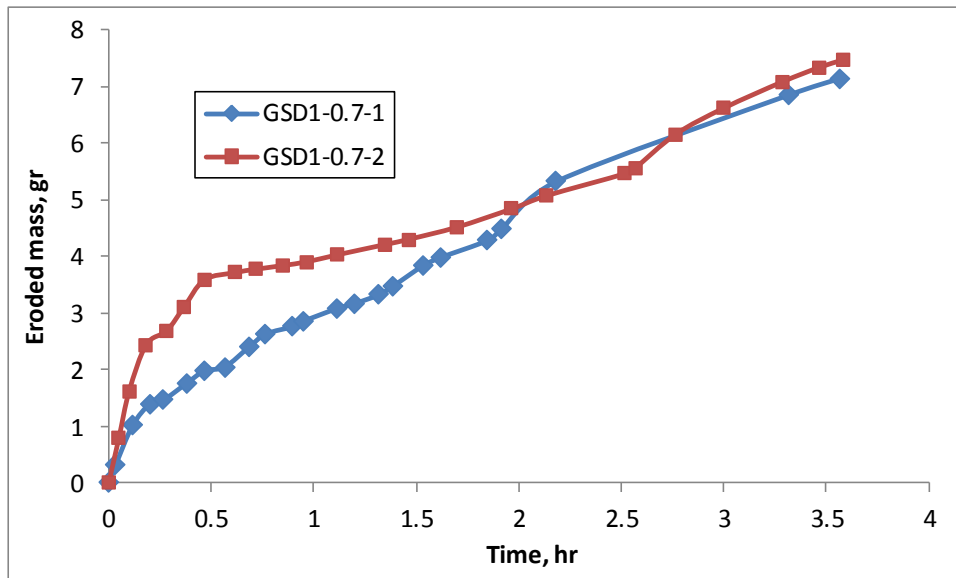


Figure 4-9: Test repeatability for GSD1 at hydraulic gradient of 0.7, comparison of eroded mass

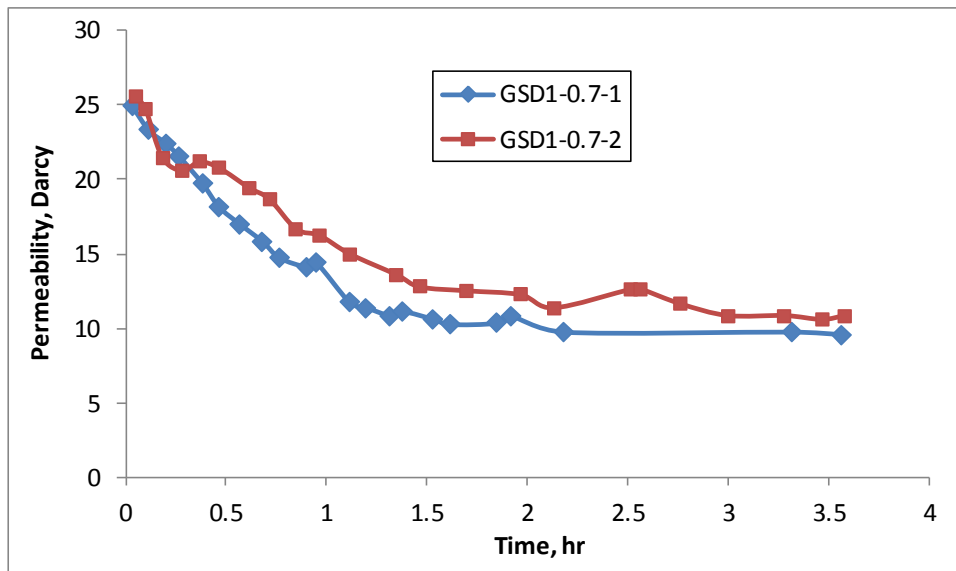


Figure 4-10: Test repeatability for GSD1 at hydraulic gradient of 0.7, comparison of permeability

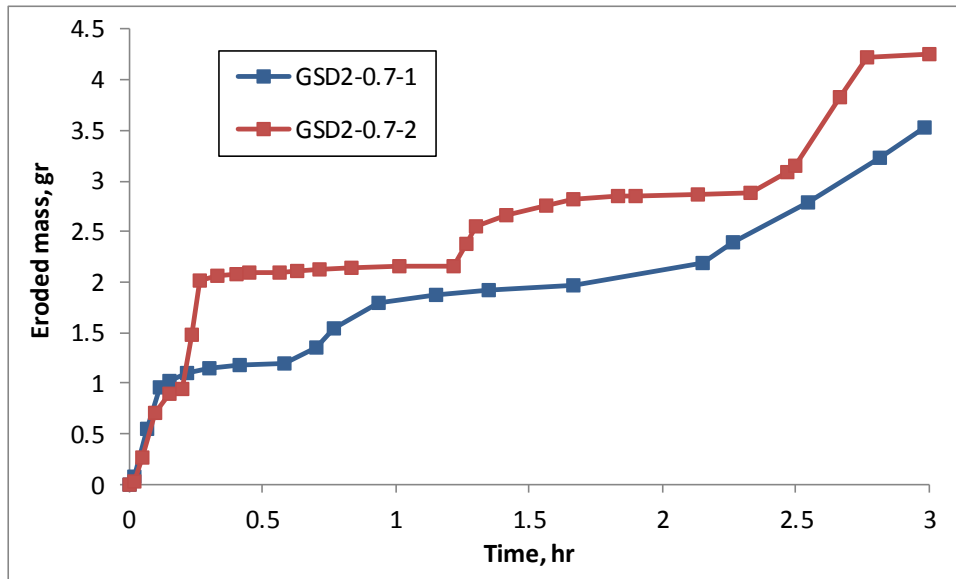


Figure 4-11: Test repeatability for GSD2 at hydraulic gradient of 0.7, comparison of eroded mass

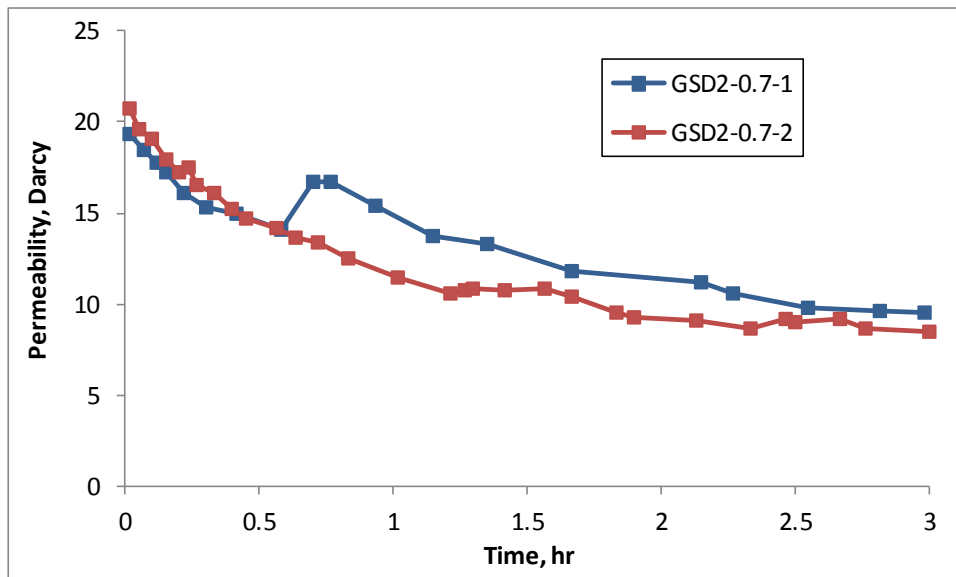


Figure 4-12: Test repeatability for GSD2 at hydraulic gradient of 0.7, comparison of permeability

Figure 4-9 through Figure 4-12 indicate reasonable agreement between the eroded mass and permeability for the repeated tests. Also, the numeric values of total eroded mass, initial and final permeability are compared for these tests in Table 4-4 and Table 4-5.

Table 4-4: Comparison of repeatability tests for GSD1

Test #	Total eroded mass (gr)	Initial permeability (Darcy)	Final permeability (Darcy)
GSD1-0.7-1	7.1	24.9	9.6
GSD1-0.7-2	7.5	25.6	10.9

For GSD1, the percentage differences for total eroded mass, initial permeability and final permeability between the repeated tests are 5.5%, 2.8% and 12.7%, respectively.

Table 4-5: Comparison of repeatability tests for GSD2

Test #	Total eroded mass (gr)	Initial permeability (Darcy)	Final permeability (Darcy)
GSD2-0.7-1	3.5	19.3	9.5
GSD2-0.7-2	4.2	20.7	8.5

The percentage differences for total eroded mass, initial permeability and final permeability for GSD2 tests are 18.2%, 7% and 11.1%, respectively. The percentage difference between the values was calculated as the ratio of their absolute difference divided by their arithmetic mean. These differences in the test results can be attributed to inevitable differences in the pore structure of the test specimens.

4.6.2 Test results

In the section, the experimental results corresponding to Test #1 to Test #7 are presented. First, the erosion test results for different GSD's at the same hydraulic gradient are compared. Next, the experimental results for each GSD at different hydraulic gradients are presented. We would stop the experiment if the test specimen didn't show significant erosion for an extended period of time. That is why some of the tests have a shorter duration compared to others.

4.6.2.1 Different GSD's and same hydraulic gradient

Comparison of eroded mass and permeability for all GSD's at the gradient of 0.5 is shown in Figure 4-13 and Figure 4-14, respectively.

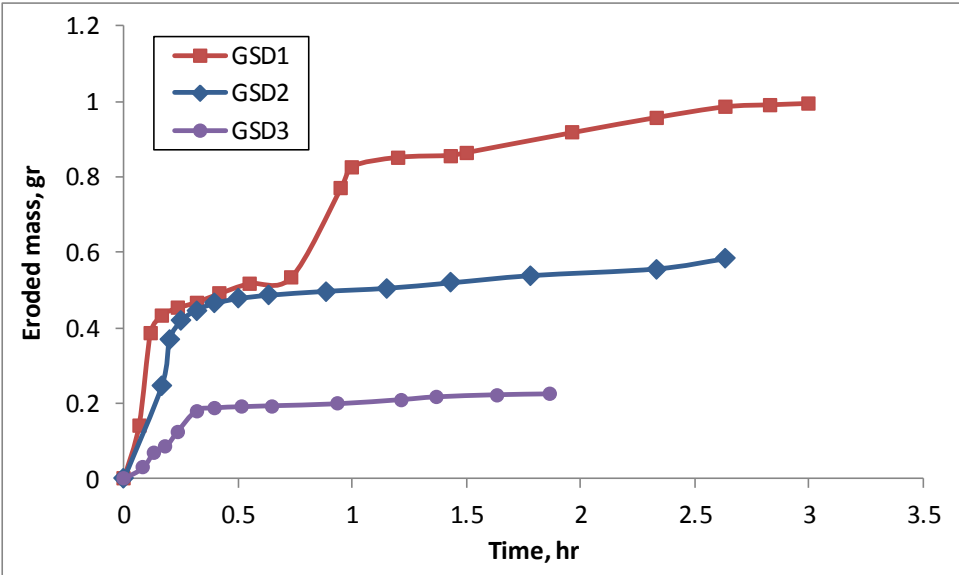


Figure 4-13: Comparison of eroded mass for all GSD's at hydraulic gradient of 0.5

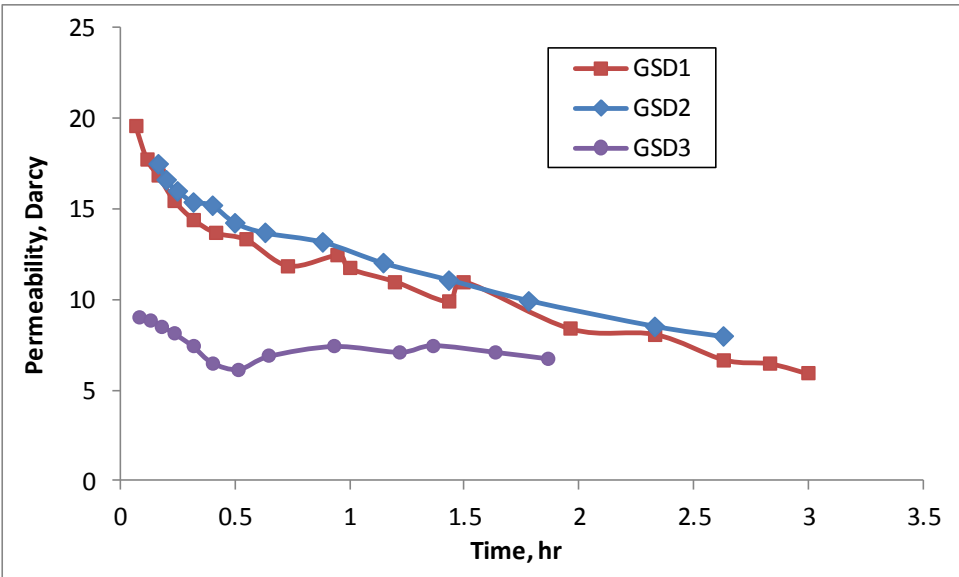


Figure 4-14: Comparison of permeability for all GSD's at hydraulic gradient of 0.5

Comparison of eroded mass and permeability for all GSD's at the gradient of 0.7 is shown in Figure 4-15 and Figure 4-16, respectively. In these figures, for a better comparison, data related to GSD1 test are cut off after 3.3 hours

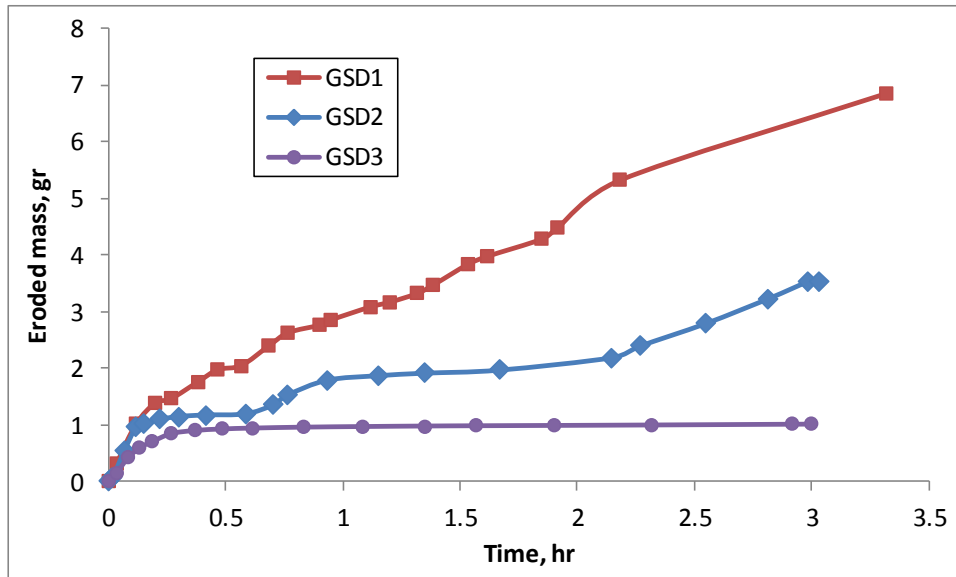


Figure 4-15: Comparison of eroded mass for all GSD's at hydraulic gradient of 0.7

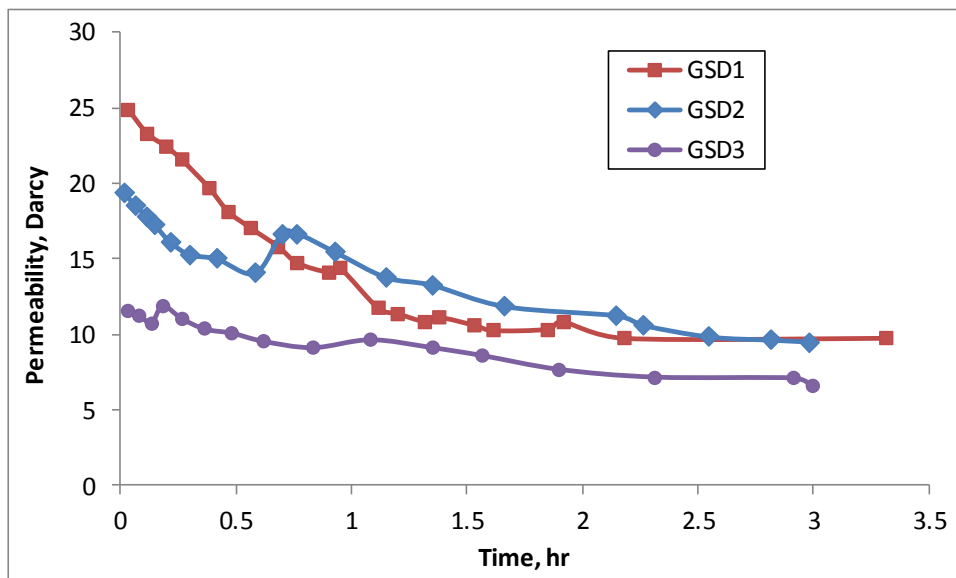


Figure 4-16: Comparison of permeability for all GSD's at hydraulic gradient of 0.7

4.6.2.2 Same GSD and different hydraulic gradients

Comparison of eroded mass and permeability for GSD1 at 3 different gradients (0.3, 0.5 and 0.7) are shown in Figure 4-17 through Figure 4-19, respectively. Since there is a high difference between the eroded mass for different hydraulic gradients, erosion test results related to GSD1 are displayed in two separate figures. As, expected, for the same GSD, a higher hydraulic gradient causes higher erosion.

The tests exhibit stress dependent permeability, i.e., higher pore pressure results in higher permeability and vice versa (Figure 4-19). This behavior is expected since the test specimens are not confined. Higher pores pressures push the grains away and cause permeability to increase. The stress dependent permeability is more pronounced initially but as the erosion process continues, the differences decrease. In case of the test conducted at the gradient of 0.3, the test was stopped after 1.6 hours since no appreciable erosion was observed.

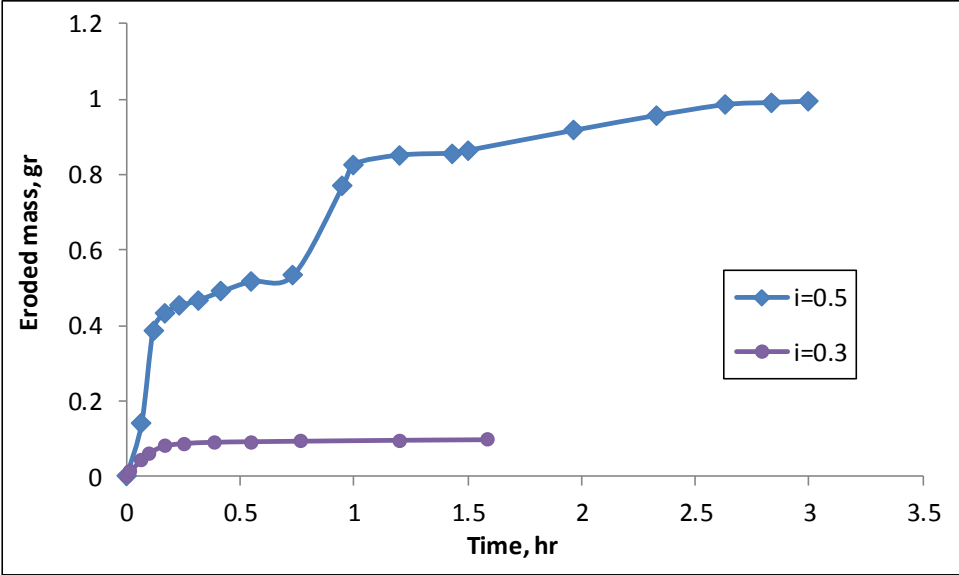


Figure 4-17: Comparison of eroded mass for GSD1 at hydraulic gradients of 0.3 and 0.5

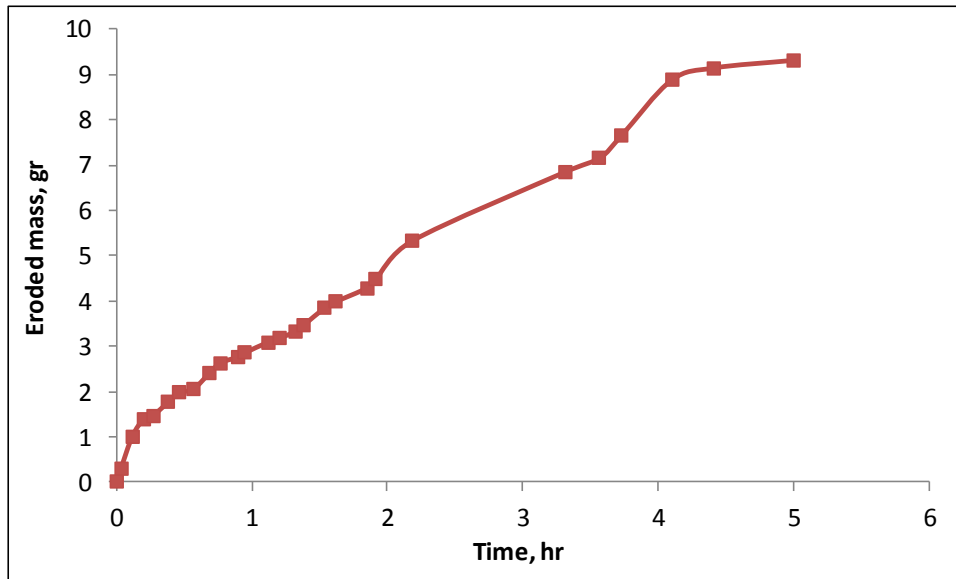


Figure 4-18: Eroded mass for GSD1 at hydraulic gradient of 0.7

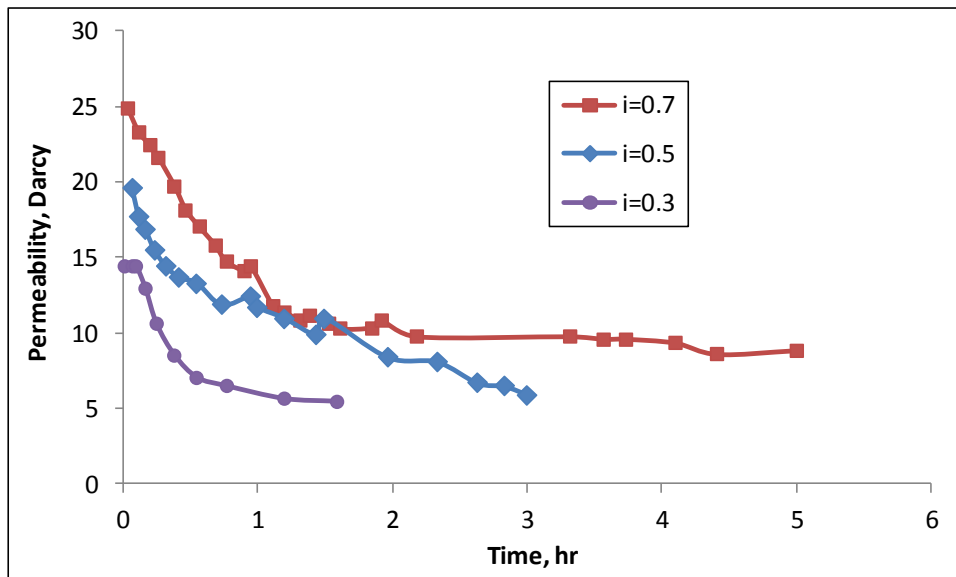


Figure 4-19: Comparison of permeability for GSD1 at different hydraulic gradients.

Comparison of eroded mass and permeability for GSD2 at two different gradients (0.5 and 0.7) is shown in Figure 4-20 and Figure 4-21 respectively. Similar to GSD1, higher gradient resulted in higher erosion. Further, stress dependent permeability was observed (although the permeability values were almost similar

at the beginning of the tests). Same plots for GSD3 are shown in Figure 4-22 and Figure 4-23.

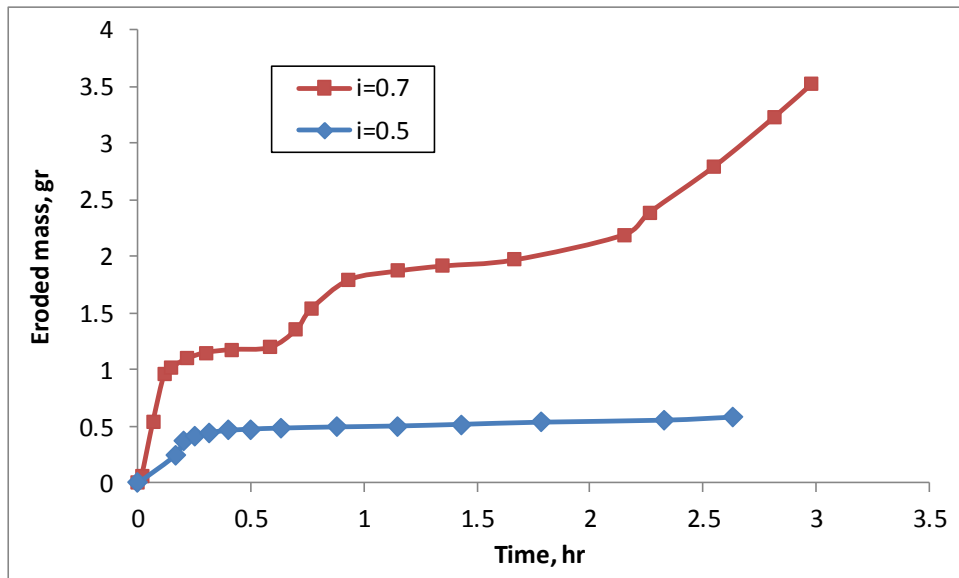


Figure 4-20: Comparison of eroded mass for GSD2 at different hydraulic gradients.

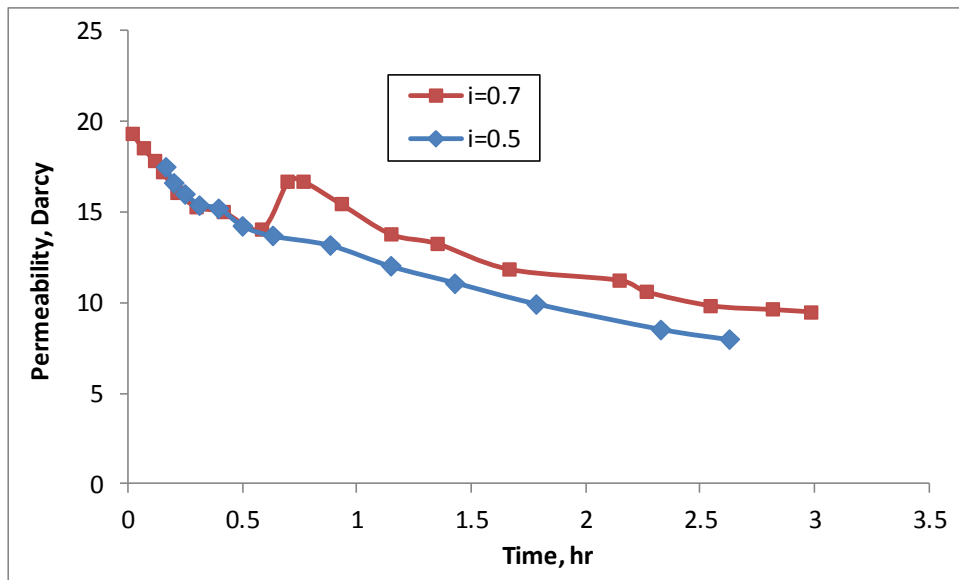


Figure 4-21: Comparison of permeability for GSD2 at different hydraulic gradients

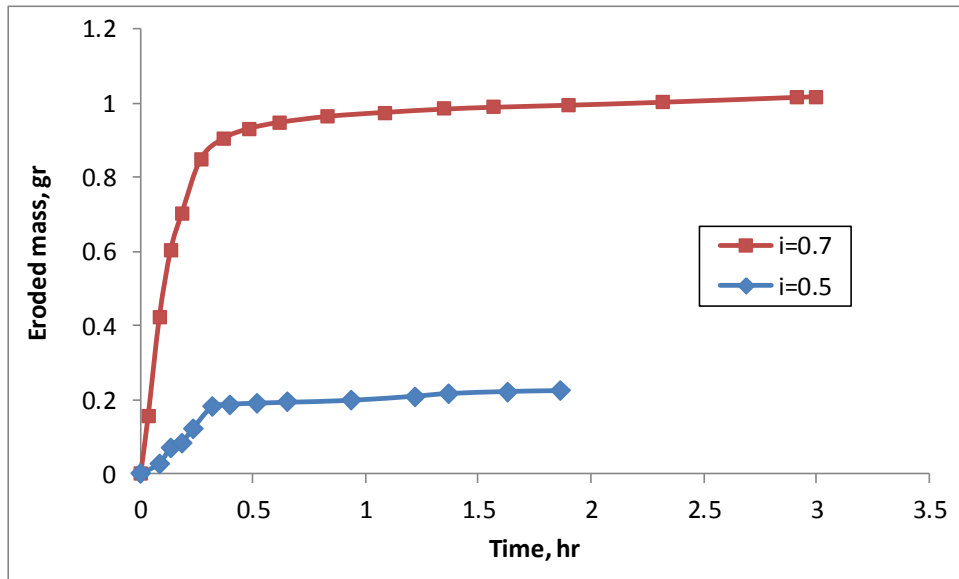


Figure 4-22: Comparison of eroded mass for GSD3 at different hydraulic gradients.

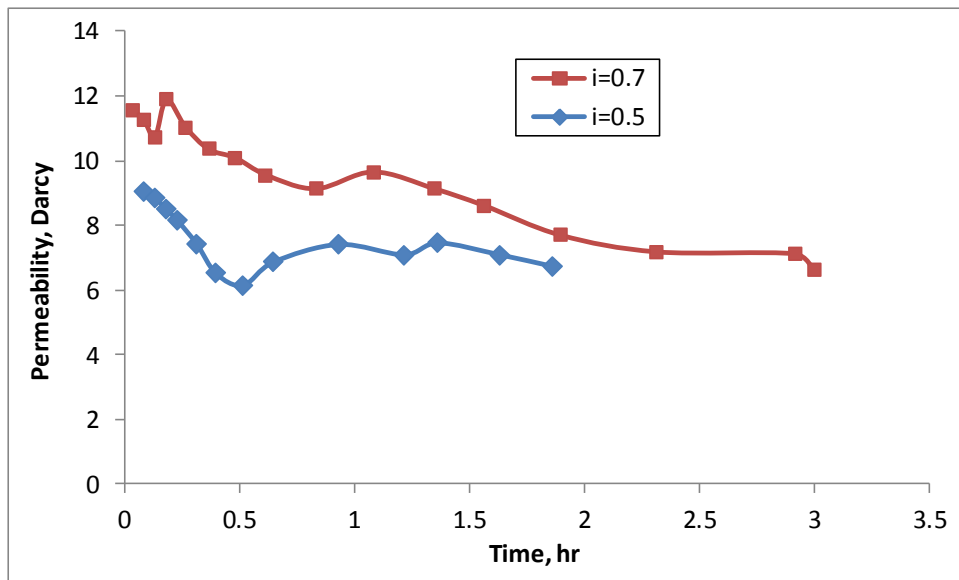


Figure 4-23: Comparison of permeability for GSD3 at different hydraulic gradients

4.7 Discussion

We conducted a series of internal erosion tests on three different grain size distributions (Figure 4-7) at different hydraulic gradients. The purpose of our experimental program was to obtain the required data to calibrate the constitutive law that we have proposed for the description of internal erosion in porous media (Chapter 5).

We designed and built an experimental apparatus to conduct the internal erosion tests. We used unconsolidated test specimens which were prepared by mixing different proportions of coarse sand, fine sand and silt. The grain size distributions of the test specimens were designed to resemble typical hydrocarbon-bearing formations. The coefficient of uniformity, C_u , for test specimens cover a wide range (Table 4-2), allowing us to observe the effect of this parameter on the internal erosion behaviour.

Referring to Table 4-1, it is observed that higher silt content results in lower average pore throat diameter. This is consistent with our expectations as smaller particles fill in the space created by larger particles and that will reduce the average pore throat size. Also, we observe that higher silt content increases the coefficients of uniformity and curvature (Table 4-2) which is again consistent with expectations.

Our test results show consistent trends. We get more erosion from poorly graded (with high coefficients of uniformity) GSD's (GSD1) compared to well-graded sand packs (GSD3). In poorly graded assemblies of particles, the difference between the smallest and the largest particles is usually a few orders of magnitude. This enables the smaller particles to migrate through the pore network formed by the larger particles. On the other hand, in well-graded grain size distributions, the average pore throat diameter is smaller than the majority of the particles and hence, the possibility of internal erosion is reduced significantly.

Also, the eroded mass is consistently higher for higher hydraulic gradients. This is also another expected result since higher hydraulic gradients result in higher fluid velocities and, consequently, stronger drag forces. When it comes to internal erosion, drag force of the flowing fluid plays a major role in particle mobilization and erosion.

In some of our tests, plots of eroded mass vs. time show periods of stabilization and destabilization. Stabilization periods can be attributed to formation of particle bridges in front of pore openings. These particle bridges limit the available cross section for particle flow and hence lower the internal erosion rate. This effect appears as plateaus in eroded mass vs. time curves for these tests. These bridge

structures formed by particles of various sizes may not remain stable and breakdown after sometime resulting in sudden release of trapped particles. This sudden jump in the number of eroded particles shows itself as a considerable increase in internal erosion rate for such tests.

Our tests exhibit stress dependent permeability behaviour. Higher hydraulic gradients increase pore pressure and as a result, reduce the effective stress within the sand pack. Since the test specimens are not confined in our experiments, higher pore pressure pushes the grains away from each other which results to an increase in permeability. Such behaviour for unconsolidated porous media has been reported by other researchers as well (e.g. Skempton and Brogan, 1994).

Another observation that we have from the experimental results is that the eroded mass shows a decaying trend with time. In other words, the rate of internal erosion decreases with time for all grain size distributions and all hydraulic gradients. This behaviour can be attributed to a process known as “pore clogging”. Pore clogging happens when some of the mobilized particles are trapped behind pore throats that are smaller than their diameters (particle entrapment). Pore clogging is a well-known cause of diminishing erosion rates in the internal erosion process. This important characteristic behavior of internal erosion forms the foundation of the constitutive law that we have offered for this phenomenon (Chapter 5).

4.8 Nomenclature

C_c Coefficient of curvature

C_u Coefficient of uniformity

d_e^* Average pore throat diameter

D_{10} The diameter through which 10% of the material can pass

D_{30} The diameter through which 30% of the material can pass

D_{60} The diameter through which 60% of the material can pass

D_i	Average diameter of i^{th} interval of grain size distribution
D_w	Average diameter of the assembly of particles
h_n	Height of the test specimen at the end of n^{th} layer
h_t	Total height of the test specimen
m_{cs}	Mass of coarse sand
m_{fs}	Mass of fine sand
m_s	Mass of silt
n_t	Total number of layers
U_n	Percentage of undercompaction for n^{th} layer
U_{ni}	Percentage of undercompaction for the first layer
U_{nt}	Percentage of undercompaction for the last layer
V_{cs}	Volume of coarse sand
V_{fs}	Volume of fine sand
V_s	Volume of silt
ΔS_i	Ratio of mass of i^{th} interval of grain size distribution to total mass
ρ_{cs}	Density of coarse sand
ρ_{fs}	Density of fine sand
ρ_s	Density of silt
$\rho_{s,eq}$	Equivalent solid density

4.9 References

- Ladd, R. S., 1978. Preparing test specimen using under compaction, *Geotech. Testing J.*, Vol. 1, No. 1, pp. 16–23.

- Skempton, A. W. and Brogan, J. M., 1994. Experiments on piping in sandy gravels, *Geotechnique*, Vol. 44, No. 3, pp. 449–460.
- Uno, T., Kamiya, K. and Matsushima, T., 1996. The Relationships between Particle Size and Void Diameter for Sand, *Proceedings of the Second International Geofilters Conference*, pp. 67-74.

Chapter 5

Modeling Internal Erosion in Porous Media as an Exponential Decay Phenomenon

5.1 Introduction

In Chapter 3, a mathematical model for predicting the rate of internal erosion was presented based on dimensional analysis approach. Working on the model in Chapter 3 was a preliminary step towards the development of a more encompassing erosion model which takes into account the physics of the erosion process. In this chapter, we try to model the internal erosion in porous media as an exponential decay phenomenon. The experimental data from Chapters 3 and 4 are used to show the validity of this idea.

5.2 Mathematical modeling

An important observation from the erosion tests presented in Chapters 3 and 4 is that the eroded mass shows a decaying trend with time. In other words, the rate of internal erosion decreases with time for all grain size distributions and all hydraulic gradients. This important characteristic of internal erosion forms the

foundation in the development of the constitutive law that we present in this chapter.

It is assumed here that the internal erosion process can be modeled as an exponential decay phenomenon. Contrary to the approach we took in Chapter 3, instead of modeling the rate of eroded solids, we model the rate of decay of the initial erodible mass in the material. During erosion, the porosity of the material increases from an initial value of φ_0 to the final (maximum) value of φ_f . The characteristic property of an exponential decay phenomenon is that the rate of decay of the decaying quantity is proportional to its current value. Therefore, the governing equation for the internal erosion process based on exponential decay assumption can be written as follows:

$$\frac{dm_r}{dt} = -\lambda m_r = -\lambda \rho_s (\varphi_f - \varphi) \quad (5-1)$$

where m_r is the remaining erodible mass per unit volume, λ is decay coefficient (or erosion coefficient) with the dimension of inverse of time, ρ_s is solid density and φ is the porosity of the medium. The initial erodible mass per unit volume, m_{r0} , can be calculated using the following equation:

$$m_{r0} = \rho_s (\varphi_f - \varphi_0) \quad (5-2)$$

In internal erosion, the law of conservation of mass for the solid phase can be simplified into the following form:

$$\frac{d\varphi}{dt} = \frac{1}{\rho_s} \frac{dm_{er}}{dt} \quad (5-3)$$

In Eq. (5-3), m_{er} is the mass of the eroded solids per unit volume and $\frac{dm_{er}}{dt}$ represents the mass generation term and expresses solid erosion rate per unit volume. Using Eq. (5-3) and knowing that the rate of decay is negative of rate of erosion, we have:

$$\frac{dm_r}{dt} = -\frac{dm_{er}}{dt} = -\rho_s \frac{d\varphi}{dt} \quad (5-4)$$

By combining the Eq. (5-1) and Eq. (5-4), we arrive at the governing equation of the internal erosion process:

$$\frac{d\varphi}{dt} = \lambda(\varphi_f - \varphi) \quad (5-5)$$

By rearranging Eq. (5-5) and integrating we have:

$$\int_{\varphi_0}^{\varphi} \frac{d\varphi}{(\varphi_f - \varphi)} = \lambda \int_{t_0}^t dt \quad (5-6)$$

In Eq. (5-6), φ_0 and t_0 are the initial porosity and starting time of the erosion process respectively. By integrating and rearranging, we arrive at the following equation for the variation of porosity with time.

$$\varphi = \varphi_f - [(\varphi_f - \varphi_0)e^{-\lambda(t-t_0)}] \quad (5-7)$$

Using Eq. (5-3), the rate of eroded mass per unit volume can be calculated using the following equation:

$$\frac{dm_{er}}{dt} = \rho_s \frac{d\varphi}{dt} = \rho_s \lambda(\varphi_f - \varphi_0)e^{-\lambda(t-t_0)} \quad (5-8)$$

By integrating the equation above from the starting time of erosion t_0 to an arbitrary time t , we arrive at the following relationship for the calculation of total eroded mass as a function of time:

$$m_{er} = \rho_s(\varphi_f - \varphi_0)(1 - e^{-\lambda(t-t_0)}) \quad (5-9)$$

We can see from Eq. (5-9) that at a sufficiently long time, the eroded mass will be equal to the initial erodible mass given in Eq. (5-2).

5.3 Determining model parameters

We propose that internal erosion is an exponential decay phenomenon. Experimental data given in Chapters 3 and 4 are used to show the validity of this idea. The proposed relationship for the variation of the eroded mass with time, which is shown in Eq. (5-9), has two model parameters, namely, the final value of porosity φ_f and the decay coefficient λ . The first step in showing the validity of the model is to determine the model parameters φ_f and λ .

We use the following equation to estimate the value of φ_f for each experiment:

$$m_f = \rho_s(\varphi_f - \varphi_0) \quad (5-10)$$

In Eq. (5-10), m_f is the final eroded mass per unit volume which is estimated using experimental data. For each experiment, value of m_f is estimated when the eroded mass reaches a plateau at the end of the experiment (with the exception of Test 2 of grain size distribution #2). Except φ_f , all other parameters in Eq. (5-10) can be obtained from experimental data. Therefore, the value of φ_f can be easily calculated using this equation.

If we rearrange Eq. (5-7) and take the natural log of both sides of the equation, we arrive at:

$$\ln(\varphi_f - \varphi) = \ln(\varphi_f - \varphi_0) - \lambda(t - t_0) \quad (5-11)$$

Therefore, if we plot $\ln(\varphi_f - \varphi)$ versus $(t - t_0)$, the is λ . In Eq. (5-11), we use the values of φ_f calculated using Eq. (5-10). Values of φ in Eq. (5-11) are calculated from experimental data following the same procedure for the calculation of φ_f .

5.4 Applying the model to constant velocity erosion tests

A series of constant velocity erosion tests were used in Chapter 3 to develop a constitutive model for internal erosion based on the dimensional analysis approach. In this section, the same tests are used to examine the validity of the proposed erosion law based on the exponential decay formulation. Figure 5-1

shows the results of these tests (Sterpi 2003). This figure shows the eroded mass vs. time for five different hydraulic gradients. In Figure 5-1, i is the hydraulic gradient applied on the test specimens.

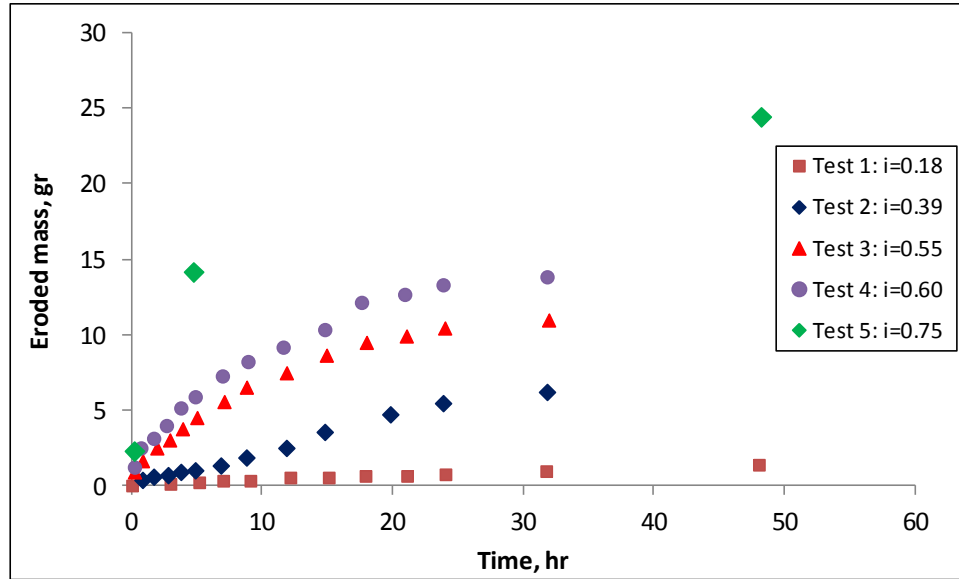


Figure 5-1: Eroded mass vs. time for constant velocity erosion tests, (Sterpi 2003)

Table 5-1 shows the properties of the tests specimens used in Sterpi (2003) experiments which are necessary for model calibration.

Table 5-1: Parameters of the erosion experiments in Sterpi (2003)

Parameter	Value
Sample diameter, m	0.07
Sample height, m	0.14
φ_0 , %	33.8
ρ_s , kg/m ³	2720

The value of φ_f for each test in Figure 5-1 is calculated using Eq. (5-10). Then Eq. (5-11) is used to calculate values of λ for all the tests using the procedure explained above. The following figures show the plots of $\ln(\varphi_f - \varphi)$ versus $(t - t_0)$ for all the tests in Figure 5-1. In these figures, the value of t_0 , which is the starting time of erosion, is set to zero. For these tests (Figure 5-1), values of λ are selected

to be the slope the linear fit. For all the plots in this chapter, linear regression lines are obtained using the method of least squares.

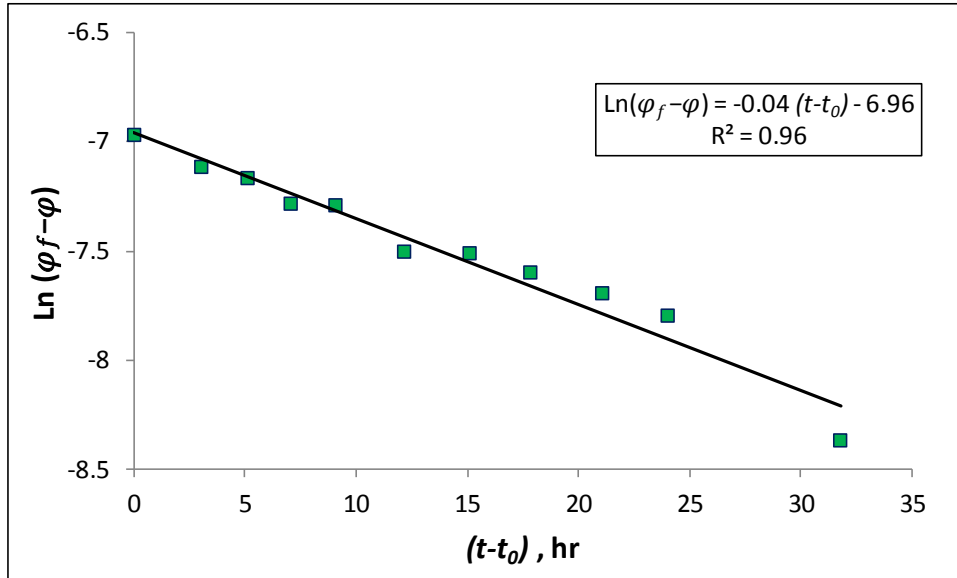


Figure 5-2: Calibration of λ for Test 1 ($i=0.18$)

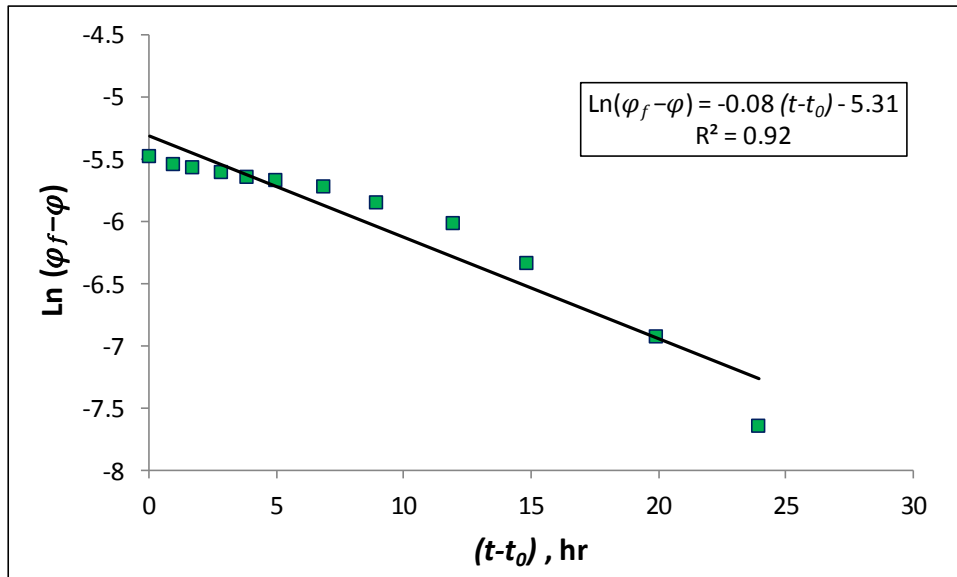


Figure 5-3: Calibration of λ for Test 2 ($i=0.39$)

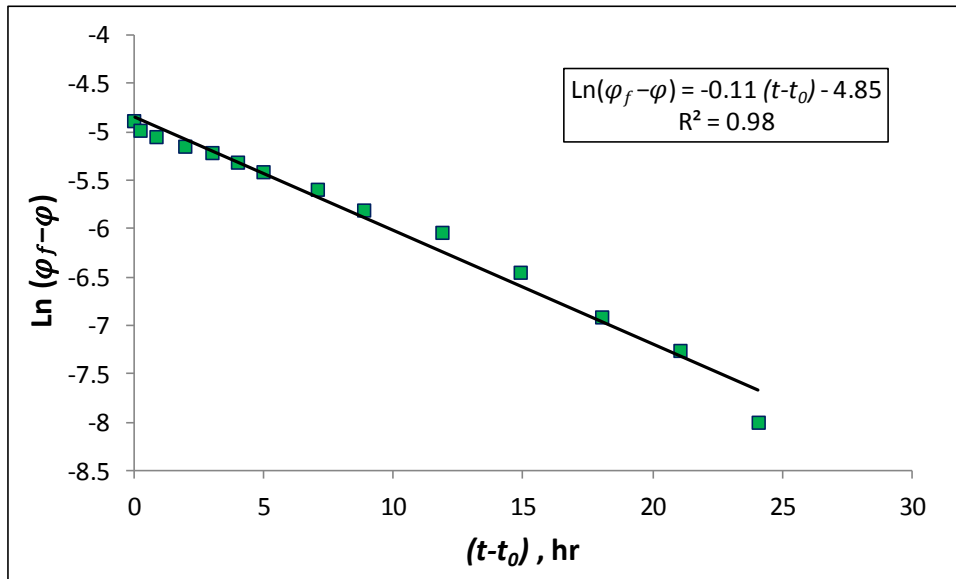


Figure 5-4: Calibration of λ for Test 3 ($i=0.55$)

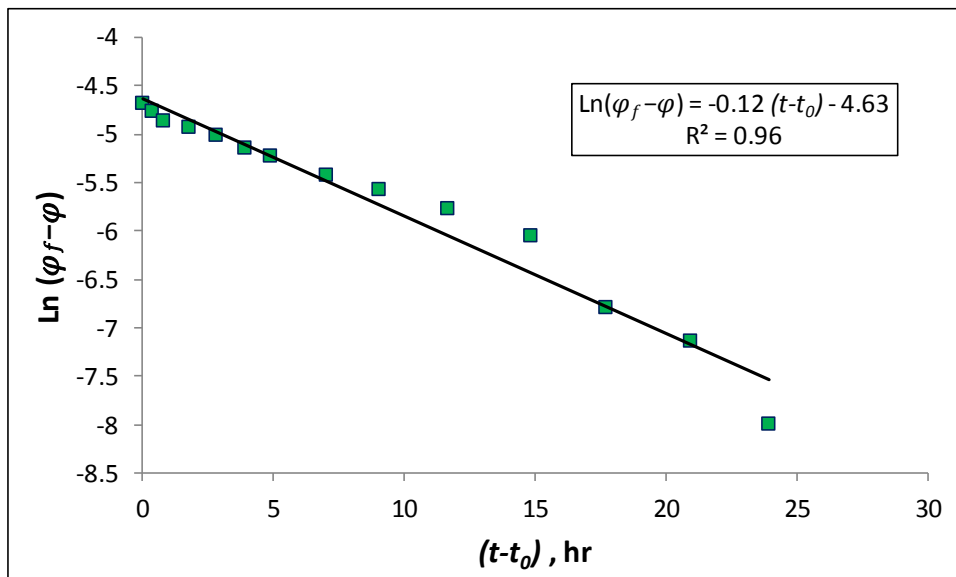


Figure 5-5: Calibration of λ for Test 4 ($i=0.60$)

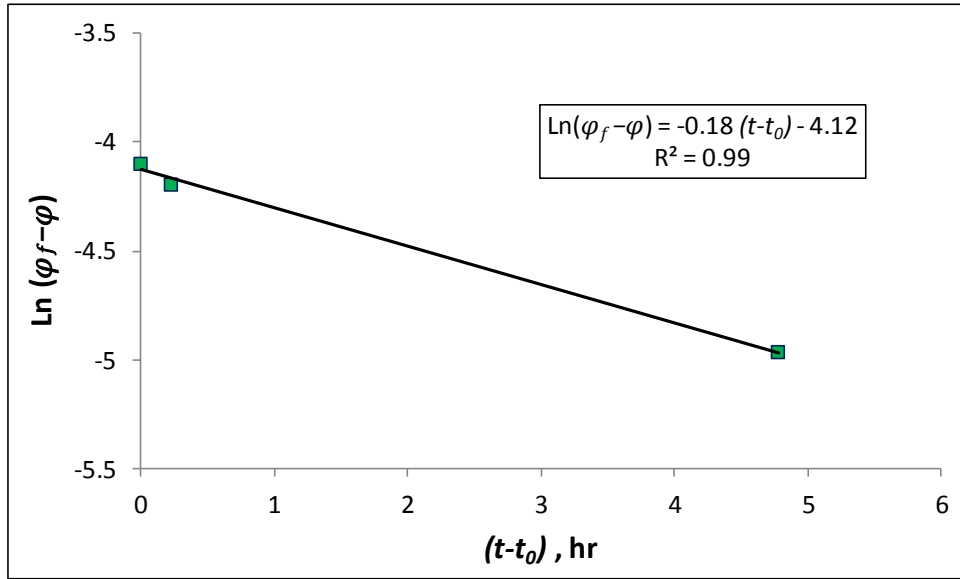


Figure 5-6: Calibration of λ for Test 5 ($i=0.75$)

Table 5-2 summarizes the calibration parameters for the constant velocity tests (Sterpi, 2003).

Table 5-2: Summary of calibration parameters for constant velocity tests

Test #	Hydraulic gradient	φ_f , %	λ , 1/hr
1	0.18	33.89	0.04
2	0.39	34.22	0.08
3	0.55	34.55	0.11
4	0.60	34.74	0.12
5	0.75	35.46	0.18

The following figures show the reproduction of experimental data with the calibrated model. Comparison between the model values and experimental data for all the constant velocity tests (Figure 5-1) are shown in Figure 5-7 to Figure 5-11. In these figures, the model values have been computed using Eq. (5-9) and the calibrated values of φ_f and λ given in Table 5-2. Also in these figures, t_0 is set to zero.

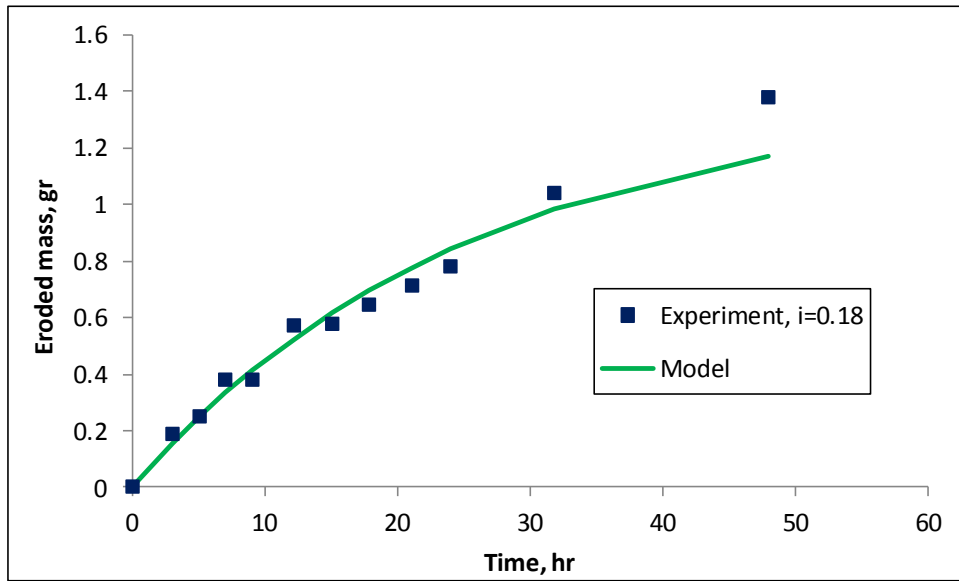


Figure 5-7: Comparison between model and experiment, Test 1

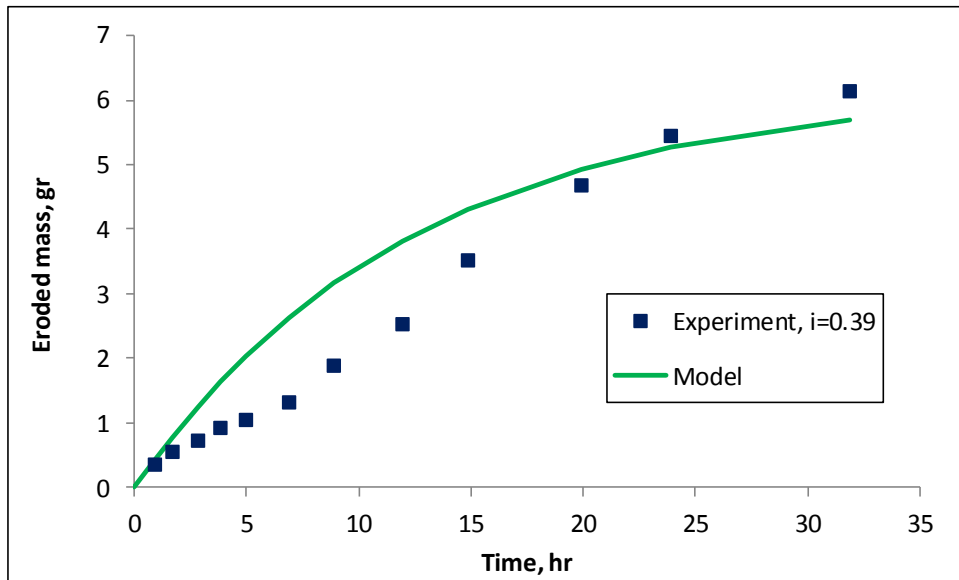


Figure 5-8: Comparison between model and experiment, Test 2

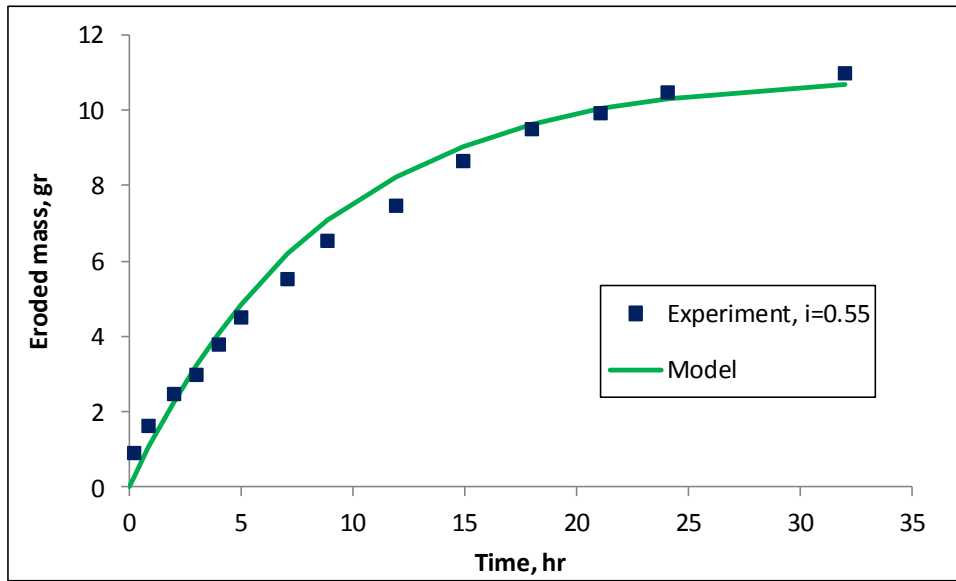


Figure 5-9: Comparison between model and experiment, Test 3

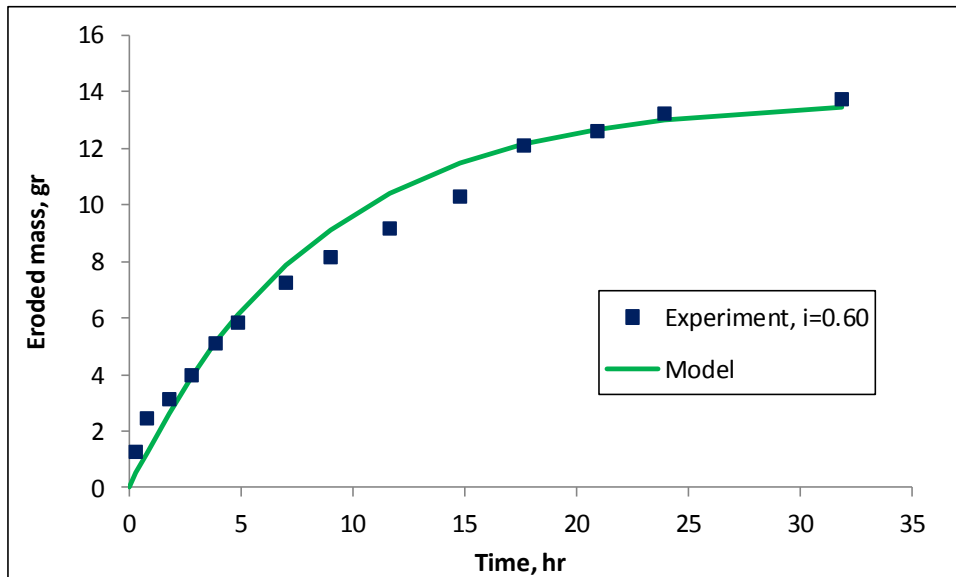


Figure 5-10: Comparison between model and experiment, Test 4

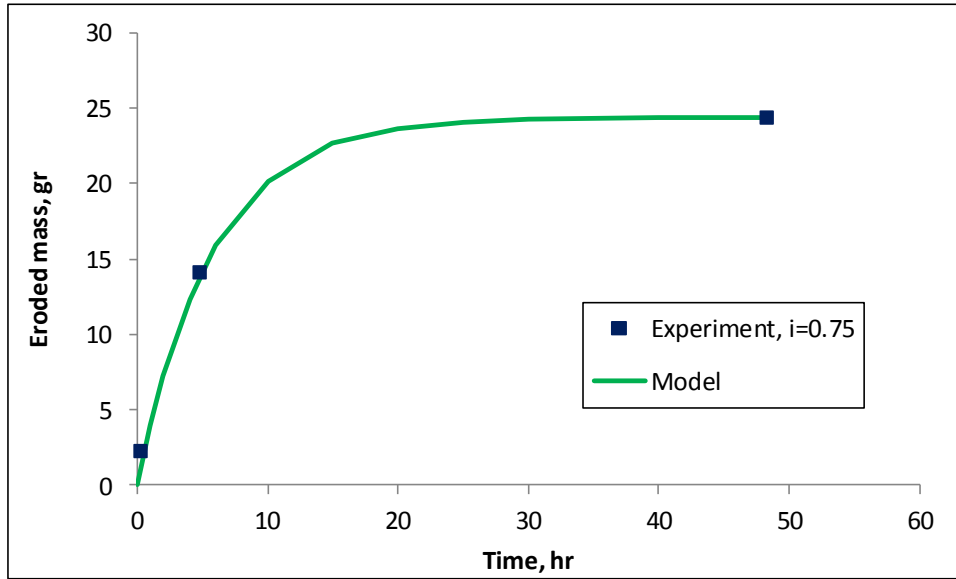


Figure 5-11: Comparison between model and experiment, Test 5

It is observed that, once values of φ_f and λ are known, experimental and calculated values of eroded mass show a very good agreement for all the Sterpi (2003) tests.

5.5 Applying the model to variable velocity tests

In this section, we follow the same procedure as the previous section in order to calibrate the exponential decay erosion model parameters using the variable velocity erosion tests. We conducted the variable velocity erosion tests on three different grain size distributions. In these tests, specimens were unconsolidated and had a diameter of 15.24 cm and a height of 16 cm. More detail on sample preparation and testing procedure is presented in Chapter 4. Table 5-3 presents a summary of the properties of these three GSD's required for the model calibration.

Table 5-3: Properties of the test specimens used in variable velocity erosion experiments

GSD #	1	2	3
Sample diameter, m	0.152	0.152	0.152
Sample height, m	0.16	0.16	0.16
φ_0 , %	40	40	40
ρ_s , kg/m ³	2514	2558	2603

Results of the erosion tests, calibration process and comparison between experimental and calculated values of eroded mass for all three GSD's are presented below.

5.5.1 Grain size distribution #1 (GSD1)

Figure 5-12 shows the result of erosion tests conducted on specimens of GSD1.

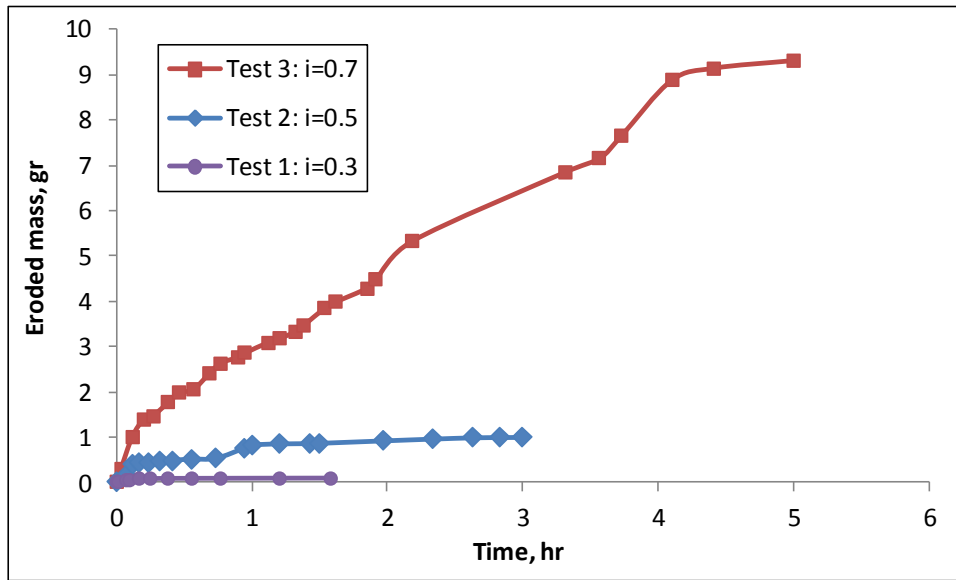


Figure 5-12: Eroded mass vs. time for GSD1

The value of φ_f for each test in Figure 5-12 was calculated using Eq. (5-10). Then Eq. (5-11) was used to calibrate values of λ for all the tests using the procedure explained above. The following figures show the plots of $\ln(\varphi_f - \varphi)$ versus $(t - t_0)$ for all the tests in Figure 5-12. For these tests, parameter λ was calibrated from the slope the linear fit.

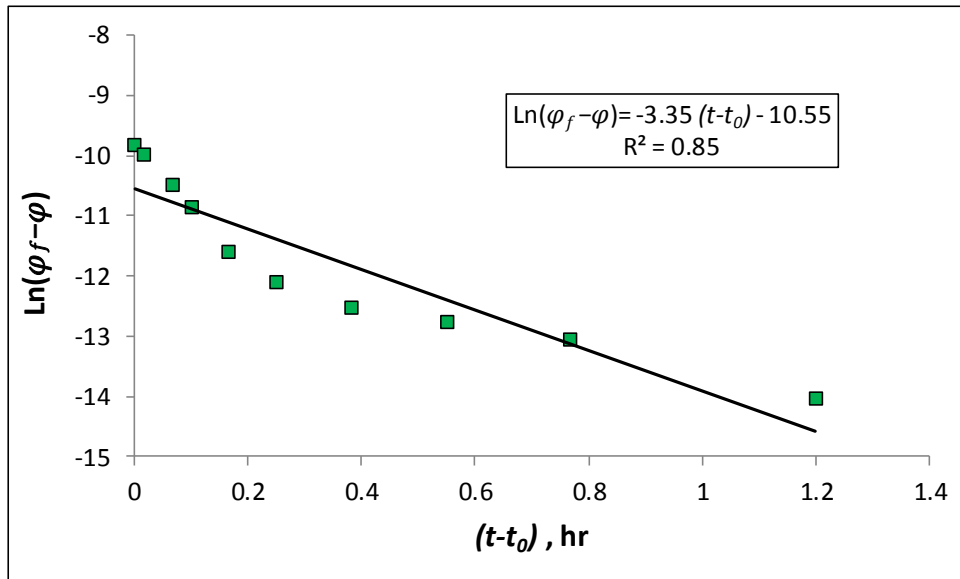


Figure 5-13: Calibration of λ for Test 1 ($i=0.30$), GSD1

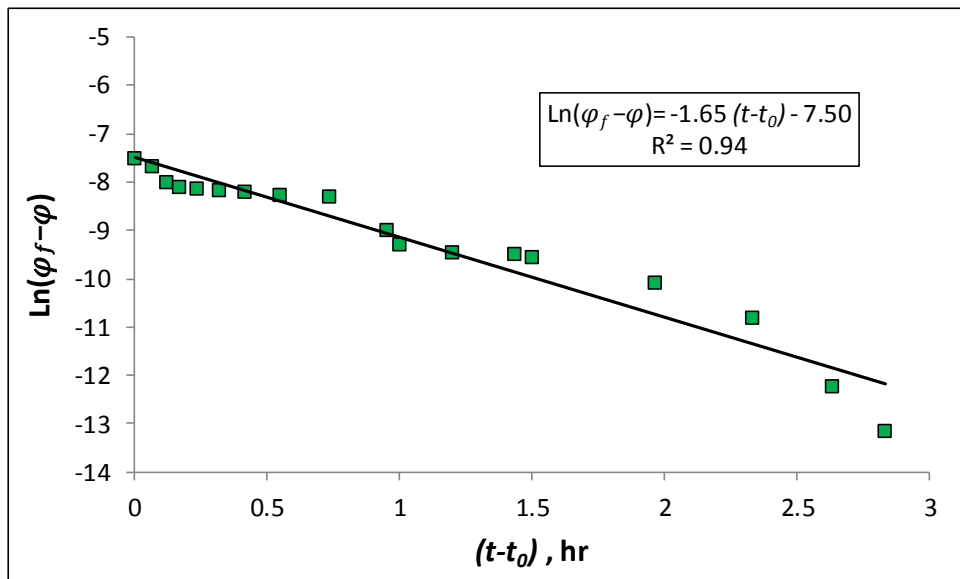


Figure 5-14: Calibration of λ for Test 2 ($i=0.50$), GSD1

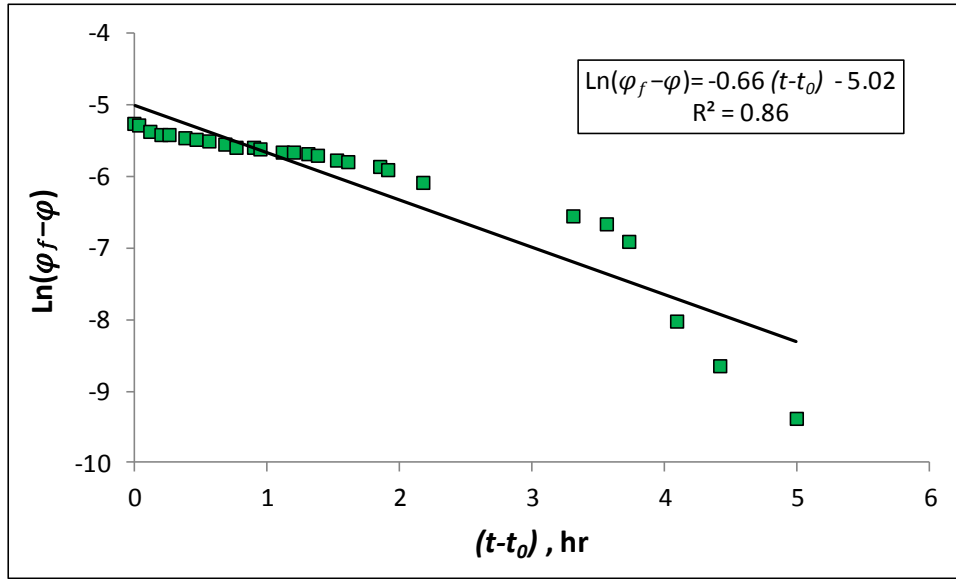


Figure 5-15: Calibration of λ for Test 3 ($i=0.70$), GSD1

Table below shows a summary of the calibration process for GSD1 tests.

Table 5-4: Summary of calibration parameters for GSD1 tests

Test #	Hydraulic gradient	φ_f , %	λ , 1/hr
1	0.30	40.0053	3.35
2	0.50	40.0542	1.65
3	0.70	40.5158	0.66

Comparison between the model calculations and experimental data for all GSD1 tests are shown in Figure 5-16 to Figure 5-18. In these figures, the model values have been calculated using Eq. (5-9) and the calibrated values of φ_f and λ given in Table 5-4. Also in these figures, t_0 is set to zero.

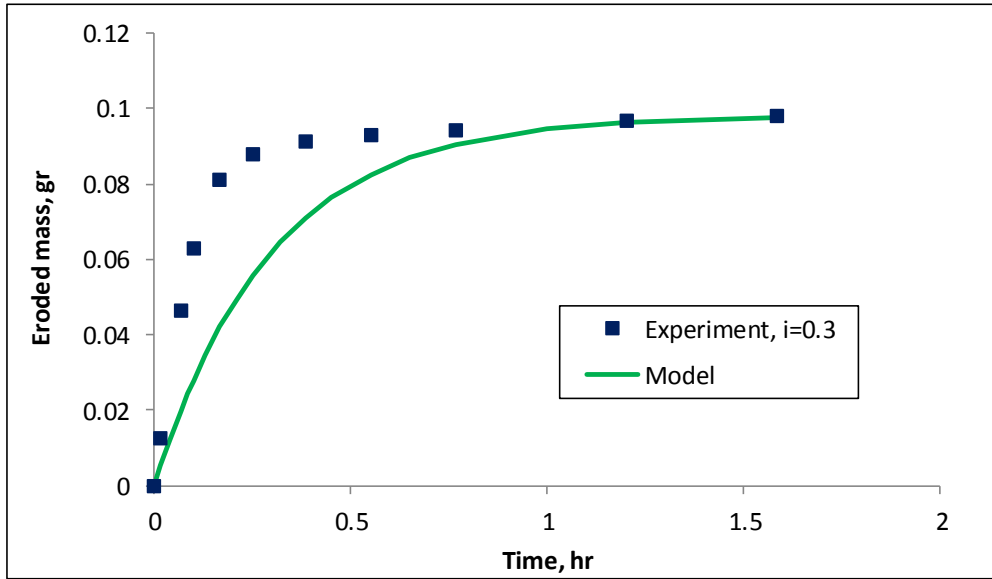


Figure 5-16: Comparison between model and experiment, Test 1, GSD1

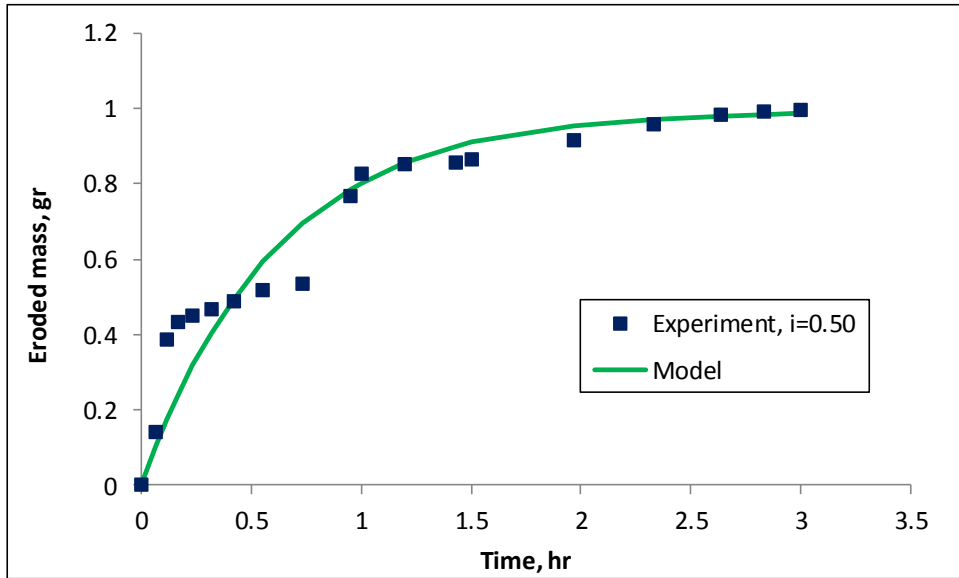


Figure 5-17: Comparison between model and experiment, Test 2, GSD1

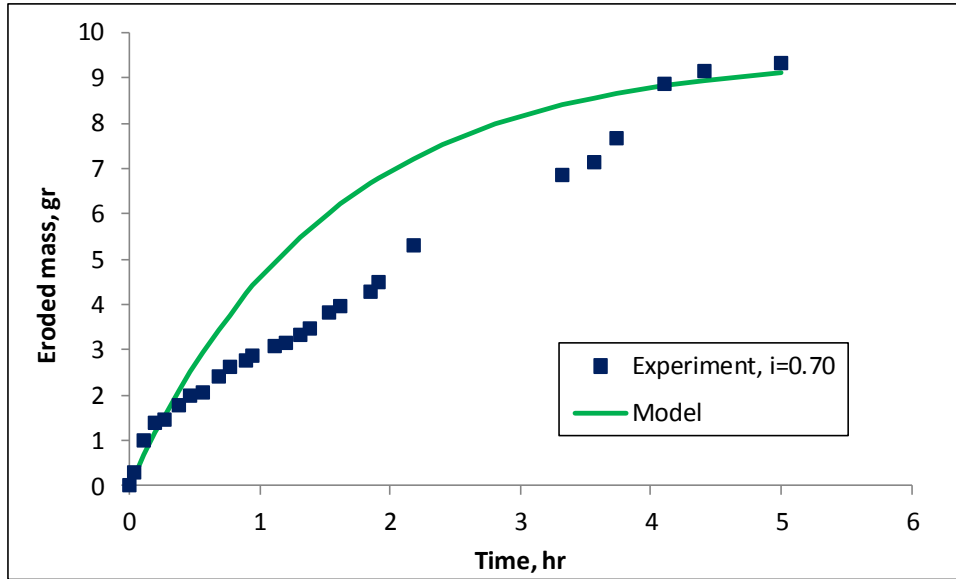


Figure 5-18: Comparison between model and experiment, Test 3, GSD1

5.5.2 Grain size distribution #2 (GSD2)

Figure 5-19 shows the result of variable velocity erosion tests conducted on specimens of GSD2. For this grain size distribution, Test 2 was terminated prematurely. The value of φ_f for this test (with gradient of 0.7) was calculated using the maximum value of eroded mass at the end of the test.

The value of φ_f for each test in Figure 5-19 is calculated using Eq. (5-10). Next, Eq. (5-11) is used to calculate values of λ for all the tests using the procedure explained for previous tests. The following figures show the plots of $\ln(\varphi_f - \varphi)$ versus $(t - t_0)$ for GSD2 tests in Figure 5-19. For these tests, values of λ are selected to be the slope the linear fit. Also in these figures, t_0 is set to zero.

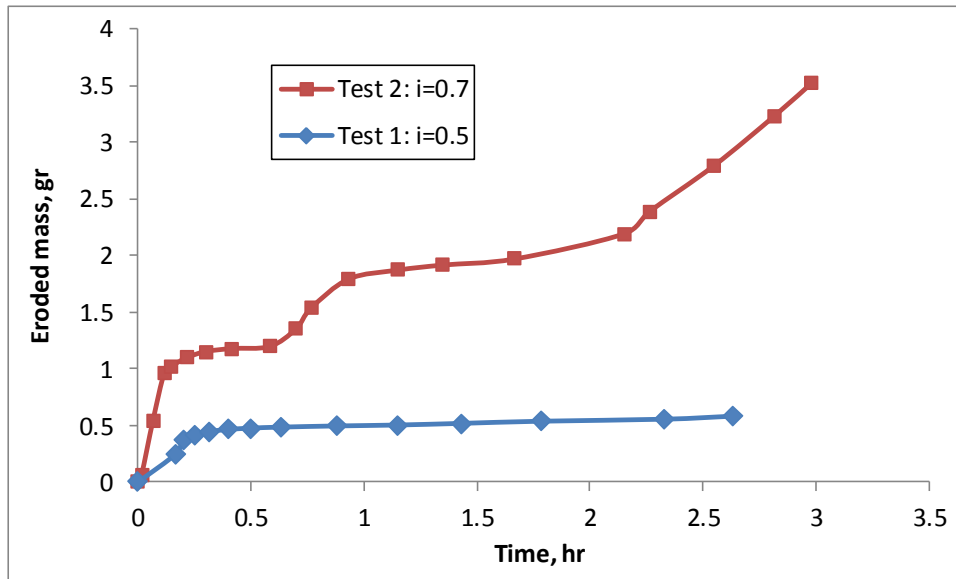


Figure 5-19: Eroded mass vs. time for GSD2

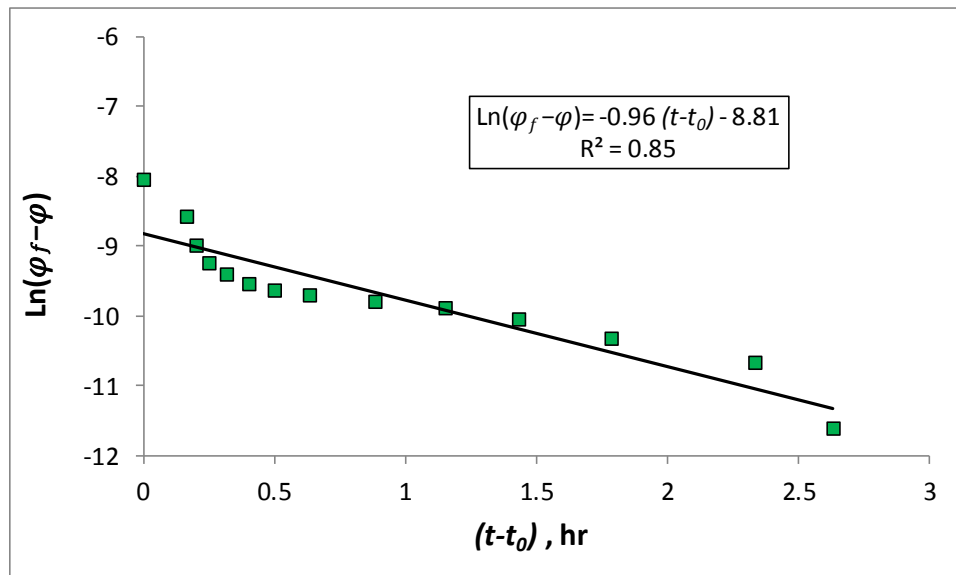


Figure 5-20: Calibration of λ for Test 1 ($i=0.50$), GSD2

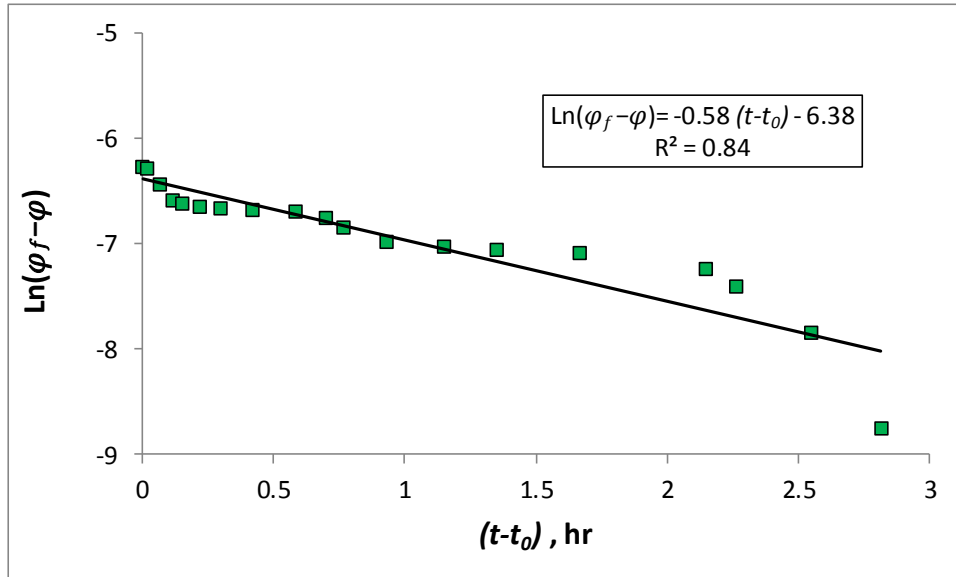


Figure 5-21: Calibration of λ for Test 2 ($i=0.70$), GSD2

Table below shows a summary of the calibration process for GSD2 tests.

Table 5-5: Summary of calibration parameters for GSD2 tests

Test #	Hydraulic gradient	φ_f , %	λ , 1/hr
1	0.50	40.0321	0.96
2	0.70	40.1888	0.58

Comparison between the model values and experimental data for GSD2 tests are shown in Figure 5-22 and Figure 5-23. In these figures, the model values have been computed using Eq. (5-9) and the calibrated values of φ_f and λ given in Table 5-5. Also in these figures, t_0 is set to zero.

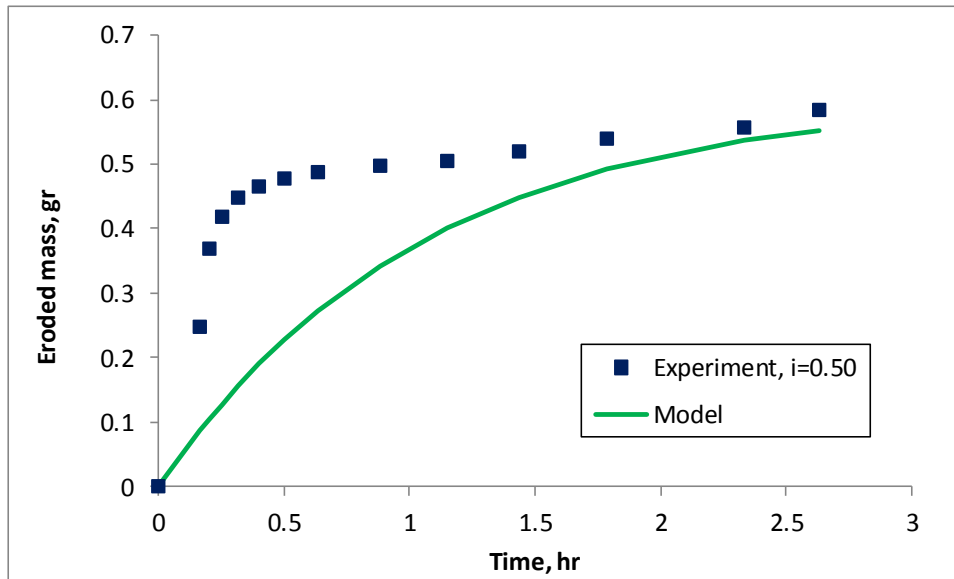


Figure 5-22: Comparison between model and experiment, Test 1, GSD2

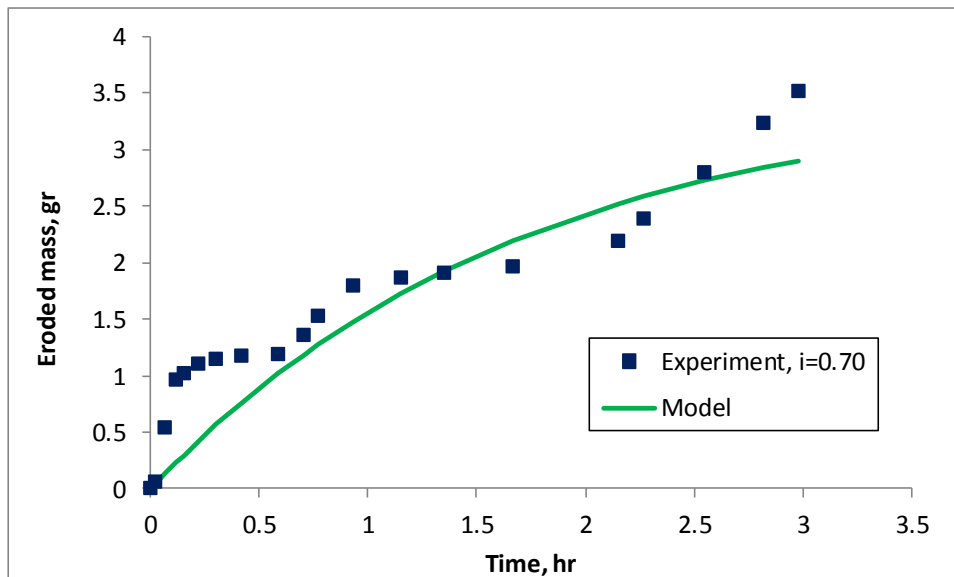


Figure 5-23: Comparison between model and experiment, Test 2, GSD2

5.5.3 Grain size distribution #3 (GSD3)

Figure 5-24 shows the result of variable velocity erosion tests conducted on specimens of GSD3.

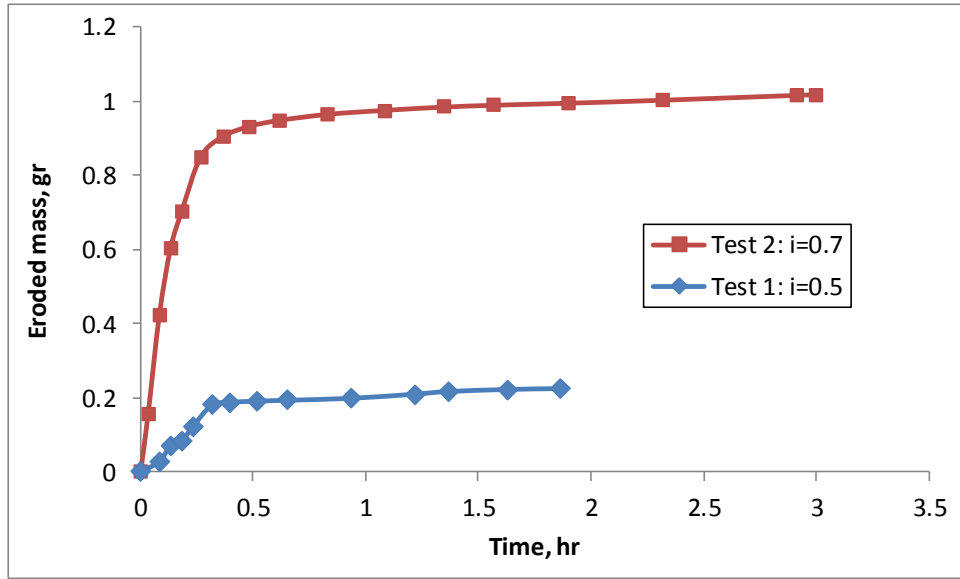


Figure 5-24: Eroded mass vs. time for GSD3

The value of φ_f for each test in Figure 5-24 was calculated using Eq. (5-10). Then Eq. (5-11) was used to calculate values of λ for all the tests using the procedure explained before. The following figures show the plots of $\ln(\varphi_f - \varphi)$ versus $(t - t_0)$ for GSD3 tests (Figure 5-24). For these tests, values of λ were obtained from the slope the linear fit. In these figures, t_0 is set to zero.

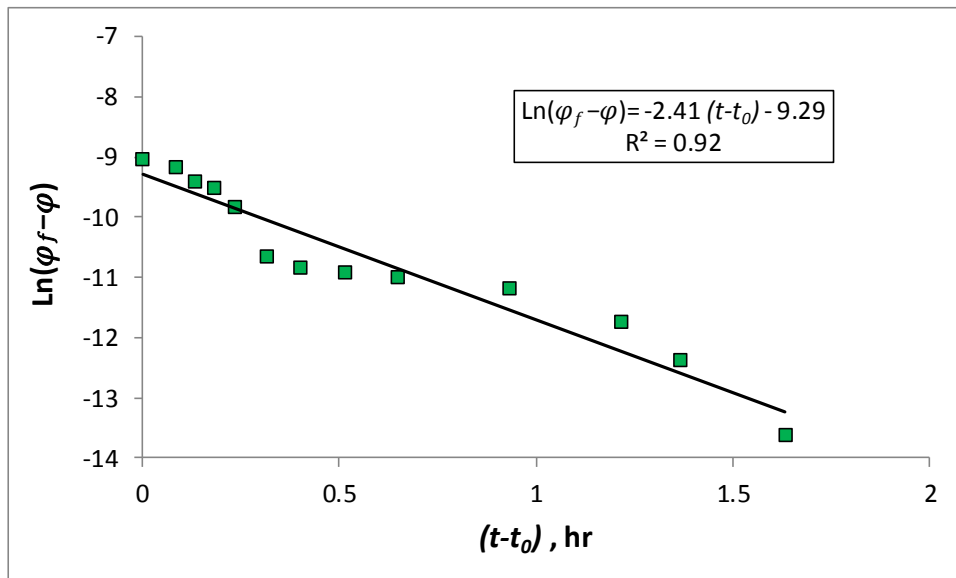


Figure 5-25: Calibration of λ for Test 1 ($i=0.50$), GSD3

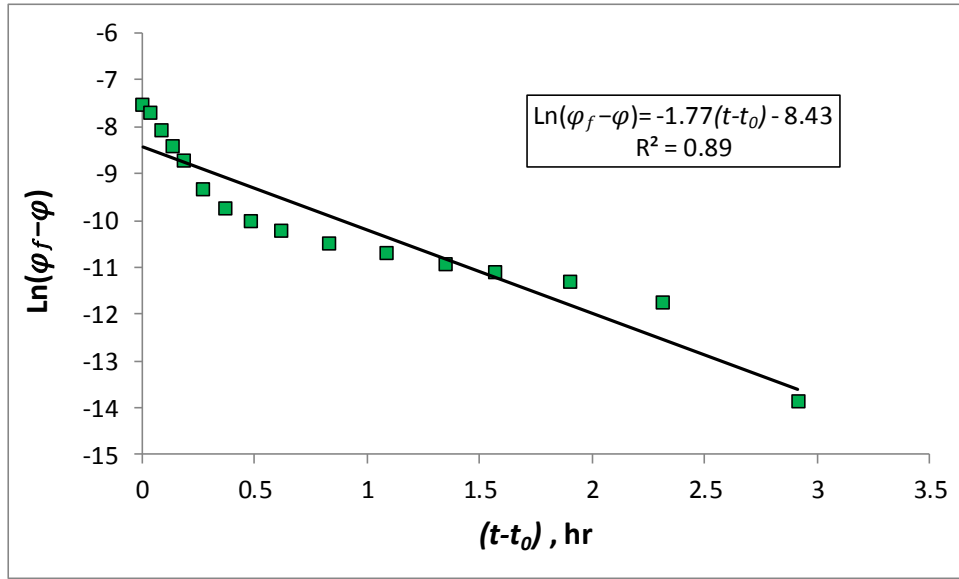


Figure 5-26: Calibration of λ for Test 2 ($i=0.70$), GSD3

Table below shows a summary of the calibration process for GSD3 tests.

Table 5-6: Summary of calibration parameters for GSD3 tests

Test #	Hydraulic gradient	φ_f , %	λ , 1/hr
1	0.50	40.0118	2.41
2	0.70	40.0535	1.77

Comparison between the model values and experimental data for both GSD3 tests are shown in Figure 5-27 and Figure 5-28. In these figures, the model values have been computed using Eq. (5-9) and the calibrated values of φ_f and λ given in Table 5-6.

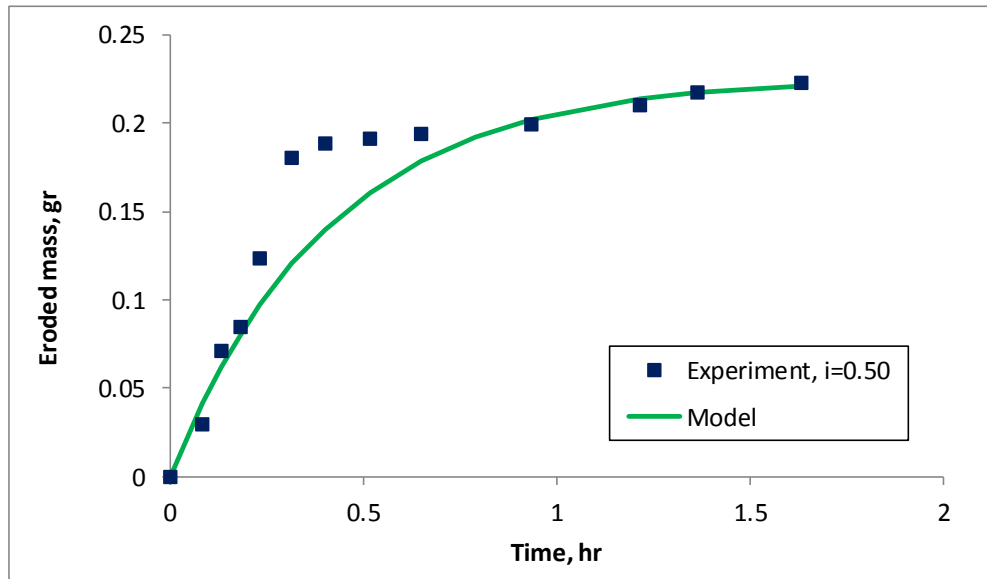


Figure 5-27: Comparison between model and experiment, Test 1, GSD3

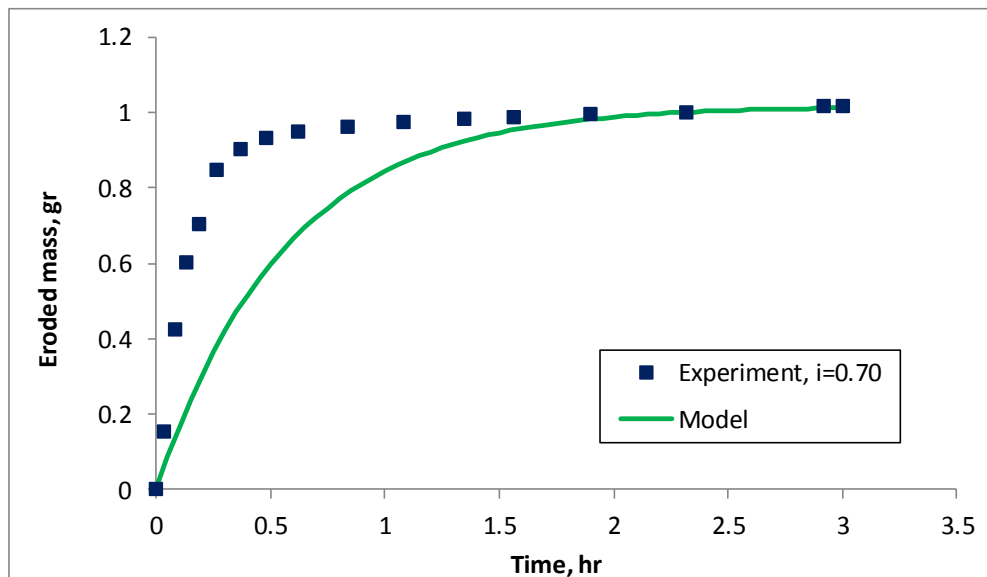


Figure 5-28: Comparison between model and experiment, Test 2, GSD3

It should be noted that quality of match between experimental and calculated values of eroded mass depends not only on the final value of porosity, φ_f , but also on the fact that how representative the calibrated decay coefficient, λ , is of the whole erosion process. For example, in Figure 5-13, we see that the calibrated value of λ for the whole test duration is smaller than the value we would get for

the initial points (up to 0.4 hours). The same trend is observed in Figure 5-20 and Figure 5-26. Therefore, for these tests, the calculated eroded mass using the model is smaller than the experimental data at the beginning of the tests. We observe the opposite of this trend in Figure 5-15. In this figure, the calibrated value of λ for the whole test duration is higher than the value we would get for the points up to 3.7 hours. That is why we observe higher calculated eroded mass compared to experimental values for most of the points of this test (Figure 5-18).

Similar to constant velocity tests, it is observed that once we have the values of φ_f and λ , experimental and calculated values of eroded mass show a reasonable agreement for all variable velocity tests.

5.6 Discussion and concluding remarks

Based on the observations from available experimental data on internal erosion, we developed a constitutive law to model internal erosion as an exponential decay phenomenon. The proposed constitutive law was calibrated using 12 different tests and four different grain size distributions. In all cases, the comparison between calculated and experimental values of eroded mass show a relatively good agreement. The results of this analysis show that, indeed, erodible mass within the test specimens decays exponentially with time.

The constitutive law for erosion which we propose based on exponential decay formulations has two calibration parameters. These parameters are the final value of porosity, φ_f and the decay coefficient (or erosion coefficient), λ . In order to use this model as a predictive tool, one needs to develop relations for φ_f and λ as functions of independent experimental and material parameters such as hydraulic gradient (fluid velocity), hydraulic conductivity (permeability) and parameters representing the particle size distribution. We have used the dimensional analysis approach (similar to the procedure used in Chapter 3) to develop such relationships for the estimation of these parameters. The results are presented in the next chapter.

5.7 Nomenclature

i	Hydraulic gradient
m_{er}	Eroded mass per unit volume
m_f	Final value of eroded mass per unit volume
m_r	Remaining mass of erodible particles per unit volume
m_{r0}	Initial mass of erodible particles per unit volume
t	Time
t_0	Starting time of erosion
λ	Decay coefficient (Erosion coefficient)
ρ_s	Grain density
φ	Porosity
φ_0	Initial porosity
φ_f	Final porosity

5.8 References

Sterpi, D., 2003. Effect of the erosion and transport of fine particles due to seepage flow. *Int. J. Geomech.*, Vol. 3, No., 1, pp. 111–122.

Chapter 6

Developing Relationships for the Prediction of φ_f and λ Using Dimensional Analysis Technique

6.1 Introduction

In Chapter 5, we developed a constitutive law to model internal erosion as an exponential decay phenomenon. This model predicts the eroded mass per unit volume using the following relationship:

$$m_{er} = \rho_s(\varphi_f - \varphi_0)(1 - e^{-\lambda(t-t_0)}) \quad (6-1)$$

This constitutive law has two calibration parameters. These parameters are the final value of porosity, φ_f and the decay coefficient (or erosion coefficient), λ . In order to use this model as a predictive tool, one needs to develop relations for φ_f and λ as functions of independent experimental and material parameters such as hydraulic gradient, hydraulic conductivity, fluid viscosity, grain density and mean diameter of eroded particles.

In this chapter, we followed the same procedure used in Chapter 3 to develop the relationships for φ_f and λ using the principles of dimensional analysis. The relationships relate φ_f and λ to material and test parameters. We used the experimental data presented in Chapters 3 and 4 to calibrate and validate the proposed relationships and the validation results show that the proposed relationships can predict φ_f and λ with reasonable accuracy.

6.2 Mathematical modeling

In this section, we develop relationships for the prediction of φ_f and λ using the principles of dimensional analysis. This procedure is similar to the approach presented in Chapter 3. First, the proposed relationship for φ_f is given. Next, we present the formulation for the estimation of decay coefficient, λ .

6.2.1 Final porosity, φ_f

Upon internal erosion, the porosity of the porous medium increases from an initial value of φ_0 to a final value of φ_f . The value of φ_f can be affected by the initial hydraulic conductivity, hydraulic gradient and fluid viscosity, among others. To derive the relationship, we use m_f (final value of eroded mass per unit volume) to represent φ_f . We can show the general form of the relationship between m_f and the most relevant parameters in the following form:

$$m_f = f[i, K_0, D_p, \mu, \rho_s] \quad (6-2)$$

where, m_f is the *final* (maximum) eroded mass per unit volume, i is the hydraulic gradient, K_0 is the initial hydraulic conductivity (with the dimension of velocity), D_p is the mean diameter of the *eroded* particles, μ is the fluid viscosity and ρ_s is the density of the eroded particles.

The list of arguments in Eq. (6-2) has been selected based on the following criteria:

- **Dimensional requirements:** The dependent parameter in this model has the dimension of mass per unit volume. In order to make this parameter dimensionless, there should be parameters on the right-hand side with

dimensions of mass and length or combinations of these dimensions. This requirement justifies the existence of $[D_p, \rho_s]$ or $[D_p, \mu]$ group of parameters on the right-hand side of this equation.

- **Physics of the problem:** Particle mobilization and erosion is due to the action of drag and kinetic forces of the flowing fluid. Parameters μ and i represent these two forces, respectively.
- **Experimental observations:** Our experimental results (Chapter 4) show that a higher initial hydraulic conductivity results in a higher eroded mass. K_0 has been used in Eq. (6-2) to represent this fact.

By applying dimensional analysis technique to Eq. (6-2), it is possible to gain some insight into the functional form of the relationship among the parameters.

There are six parameters in Eq. (6-2) but there are only three independent dimensions, namely; mass $[M]$, length $[L]$, and time $[T]$. Infinite number of dimensionless parameters can be formed using the parameters given in Eq. (6-2) but using the Buckingham's π theorem, only three of them will be independent (Hornung 2006).

Using the parameter given in Eq. (6-2), the following relationships are formed to represent the three standard physical measures when forming the dimensionless groups. Different combinations of these parameters can be used to form the basic standard measures but at the end, the resulting functional relationship can be reduced to the same form. Therefore, Eq. (6-3) through (6-5) are used to represent mass, length and time, respectively.

$$[\rho_s D_p^3] = [M] \tag{6-3}$$

$$[D_p] = [L] \tag{6-4}$$

$$\left[\frac{D_p}{K_0}\right] = [T] \tag{6-5}$$

Using the relationships above, the parameters in Eq. (6-2) are nondimensionalized one by one.

$$[m_f] = [ML^{-3}] = [(\rho_s D_p^3)(D_p^{-3})] = [\rho_s] \quad (6-6)$$

$$[\mu] = [ML^{-1} T^{-1}] = \left[(\rho_s D_p^3)(D_p)^{-1} \left[\frac{D_p}{K_0} \right]^{-1} \right] = [\rho_s D_p K_0] \quad (6-7)$$

The third dimensionless parameter is selected to be hydraulic gradient, i .

Using Eq. (6-6) and Eq. (6-7) and the parameter i , Eq. (6-2) can be written in the following form:

$$\frac{m_f}{\rho_s} = f \left[\frac{\rho_s D_p K_0}{\mu}, i \right] \quad (6-8)$$

where $f[\]$ denotes the function of the variables in the bracket.

From the law of conservation of mass (Chapter 3), we know that $\frac{m_f}{\rho_s}$ is equivalent to the difference between the final (maximum) porosity and the initial porosity, $\varphi_f - \varphi_0$. Therefore, Eq. (6-8) can be further simplified into the following form:

$$\varphi_f - \varphi_0 = f \left[\frac{\rho_s D_p K_0}{\mu}, i \right] \quad (6-9)$$

The actual functional form in Eq. (6-9) is unknown but based on experimental observations (Chapters 3 and 4), we know that $\varphi_f - \varphi_0$ is directly proportional to both i and K_0 parameters. Having these observations and using the approximation theory (David and Nolle 1982), the functional form of Eq. (6-9) can be approximated using the equation below:

$$\varphi_f - \varphi_0 = \alpha \left[\frac{\rho_s D_p K_0 i}{\mu} \right]^\beta \quad (6-10)$$

where α and β are dimensionless calibration parameters which will be determined using experimental data.

6.2.2 Decay coefficient, λ

The decay coefficient determines how slowly or how quickly the erosion process occurs. The general functional relationship between the decay coefficient and the most relevant material and test parameters can be shown as follows:

$$\lambda = g[i, K_0, D_p] \quad (6-11)$$

The parameters in Eq. (6-11) have the same definitions as those given in the previous section and are selected based on dimensional requirements (D_p), and experimental observations (i and K_0).

There are four parameters in Eq. (6-11) but there are only two independent dimensions, namely; length [L] and time [T]. Infinite number of dimensionless parameters can be formed using the parameters given in Eq. (6-11) but using the Buckingham's π theorem, only two of them will be independent (Hornung 2006).

Using the parameters listed in Eq. (6-11), we use Eq. (6-12) and Eq. (6-13) to represent length and time, respectively.

$$[D_p] = [L] \quad (6-12)$$

$$\left[\frac{D_p}{K_0}\right] = [T] \quad (6-13)$$

Using the relationships above, the decay coefficient can be nondimensionalized as follows:

$$[\lambda] = [T^{-1}] = \left[\left(\frac{D_p}{K_0}\right)^{-1}\right] \quad (6-14)$$

The second dimensionless parameter is selected to be the hydraulic gradient, i .

Using Eq. (6-14) and the parameter i , Eq. (6-11) can be written in the following form:

$$\frac{\lambda D_p}{K_0} = g[i] \quad (6-15)$$

where $g[]$ denotes the function of the variables in the bracket.

We don't know the functional relationship of the equation above but using the approximation theory (David and Nolle 1982), the functional form of Eq. (6-15) can be approximated using the following relationship:

$$\frac{\lambda D_p}{K_0} = \gamma_1 i^{\gamma_2} \quad (6-16)$$

where γ_1 and γ_2 are dimensionless calibration parameters which have to be determined using experimental data.

6.3 Experimental data

Internal erosion experiments presented in Chapters 3 and 4 are used to find the calibration parameters in Eq. (6-10) and Eq. (6-16). These experiments include constant velocity erosion tests (Sterpi 2003) and variable velocity erosion tests conducted on three different grain size distributions (GSD1, GSD2 and GSD3) which were presented in Chapter 4. Figure 6-1 shows the results of the constant velocity erosion experiments conducted by Sterpi (2003). Figure 6-2 through Figure 6-5 show the results of variable velocity erosion tests which we conducted for different grain size distributions. These plots show the eroded mass vs. time for different hydraulic gradients. Since there is a big difference between the eroded mass for different hydraulic gradients, test results related to GSD1 are displayed in two separate figures.

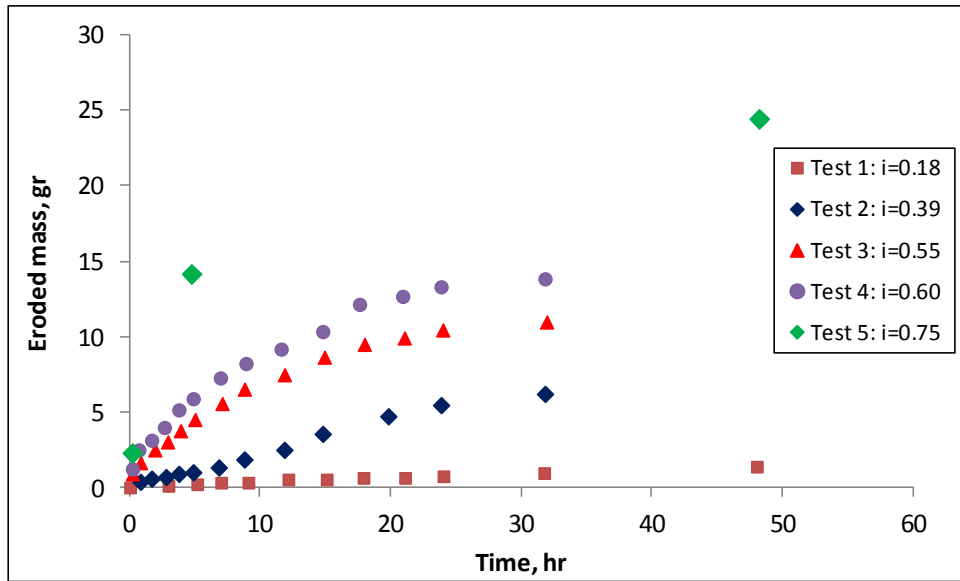


Figure 6-1: Results of erosion tests for different hydraulic gradients, Sterpi (2003)

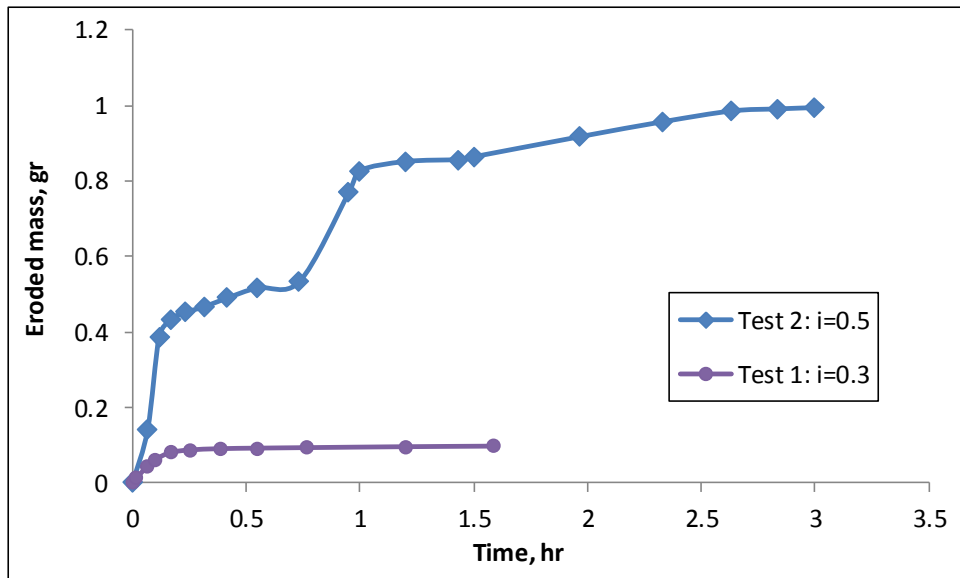


Figure 6-2: Eroded mass vs. time for GSD1, Tests 1 and 2

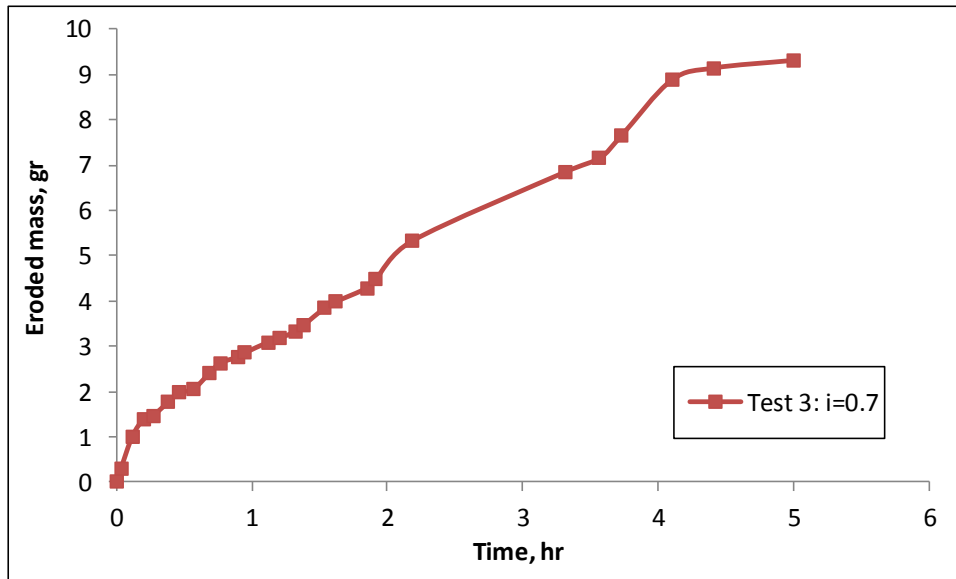


Figure 6-3: Eroded mass vs. time for GSD1, Test 3

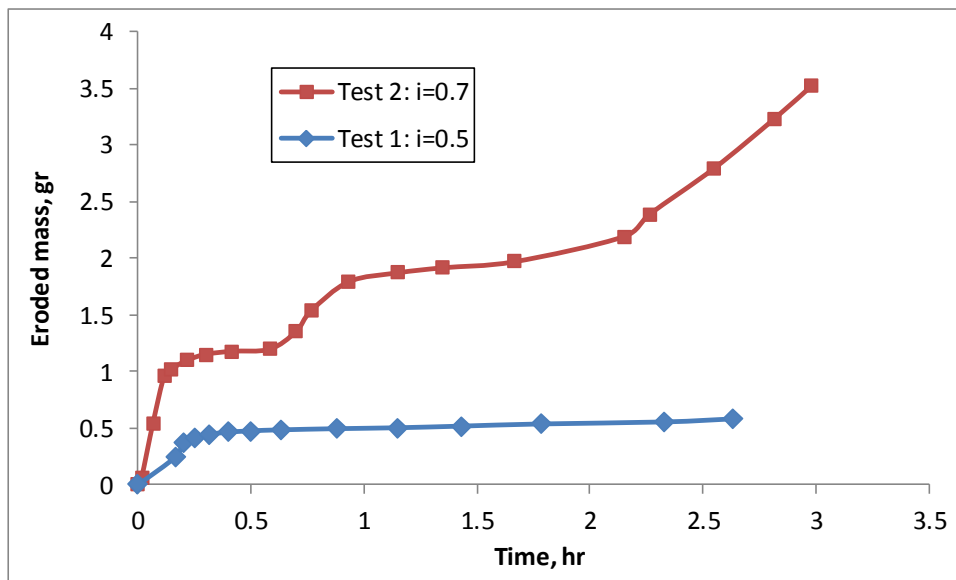


Figure 6-4: Eroded mass vs. time for GSD2

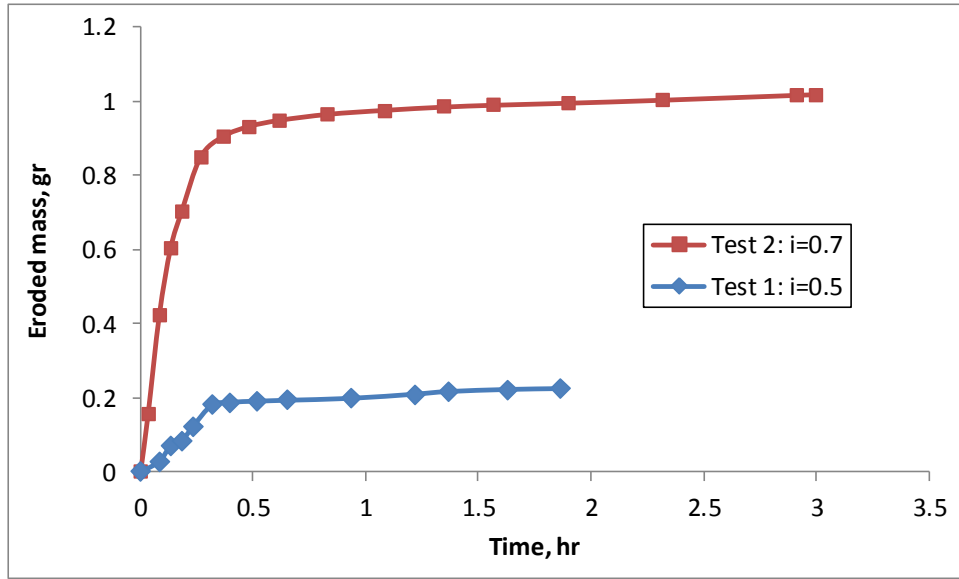


Figure 6-5: Eroded mass vs. time for GSD3

Table 6-1 shows a summary of the required parameters for model calibration for the above tests. In this table, values of parameter D_p for GSD2, GSD2 and GSD3 are calculated using the procedure explained in Chapter 3.

Table 6-1: Required parameters for model calibration for Sterpi (2003), GSD1, GSD2 and GSD3 experiments

Parameter	Sterpi (2003)	GSD1	GSD2	GSD3
Sample diameter, m	0.07	0.152	0.152	0.152
Sample height, m	0.14	0.16	0.16	0.16
Initial porosity, ϕ_0	0.338	0.40	0.40	0.40
Grain density, ρ_s , kg/m ³	2720	2514	2558	2603
Mean diam. of eroded particles, D_p , micron	3.7	3	3.1	3.8
Fluid viscosity, μ , Pa.sec	0.001	0.001	0.001	0.001

6.4 Model calibration

The proposed relationships for determining ϕ_f and λ are given by Eq. (6-10) and Eq. (6-16), respectively. There are four calibration parameters in these equations namely; α , β , γ_1 and γ_2 .

If we take the natural log from both sides of Eq. (6-10), we have:

$$\ln(\varphi_f - \varphi_0) = \ln \alpha + \beta \ln \left(\frac{\rho_s D_p K_0 i}{\mu} \right) \quad (6-17)$$

Therefore, if we plot $\ln(\varphi_f - \varphi_0)$ versus $\ln \left(\frac{\rho_s D_p K_0 i}{\mu} \right)$, $\ln \alpha$ will be the intercept and β will be the slope of the line.

Similarly, if we take the natural log from both sides of Eq. (6-16), we have:

$$\ln \left(\frac{\lambda D_p}{K_0} \right) = \ln \gamma_1 + \gamma_2 \ln i \quad (6-18)$$

Therefore, if we plot $\ln \left(\frac{\lambda D_p}{K_0} \right)$ versus $\ln i$, $\ln \gamma_1$ will be the intercept and γ_2 will be the slope of the line. In this section, we use the experimental results presented in the previous section to determine α , β , γ_1 and γ_2 parameters for constant and variable velocity erosion tests.

6.4.1 Constant velocity tests

Experimental data given in Figure 6-1 were used to estimate the values of α , β , γ_1 and γ_2 for Sterpi (2003) experiments. Tests 1, 2 and 3 (with hydraulic gradients of 0.18, 0.39 and 0.55, respectively) were used to determine the material parameters and Tests 4 and 5 (with the hydraulic gradients of 0.60 and 0.75, respectively) were used to validate the proposed relationships. Table 6-2 shows other necessary parameters for the calibration of α , β , γ_1 and γ_2 for Tests 1, 2 and 3. In this table, m_{final} is the final value of eroded mass which is estimated from Figure 6-1 for each test. Also in this table, values of the decay coefficient, λ , were estimated using the procedure explained in Chapter 5.

Table 6-2: Required parameters for model calibration, Sterpi (2003) tests

Test #	Hydraulic gradient	m_{final} , gr	λ , 1/hr	K_0 , m/sec
1	0.18	1.4	0.04	0.0001
2	0.39	6.1	0.08	0.0001
3	0.55	11	0.11	0.0001

Using the data given in Table 6-1 and Table 6-2, we calculated the values of $(\varphi_f - \varphi_0)$, $\left(\frac{\rho_s D_p K_0 i}{\mu}\right)$ and $\left(\frac{\lambda D_p}{K_0}\right)$. Then we plotted the lines corresponding to Eq. (6-17) and Eq. (6-18) to estimate α , β , γ_1 and γ_2 for Tests 1, 2 and 3. Results are shown in Figure 6-6 and Figure 6-7.

In Figure 6-6 and Figure 6-7, the green squares represent experimental data and the solid line represents the best linear fit. For all the plots in this chapter, linear regression lines were obtained using the method of least squares. The corresponding equation for the linear fit is also shown in these plots along with the value of the coefficient of determination, R^2 .

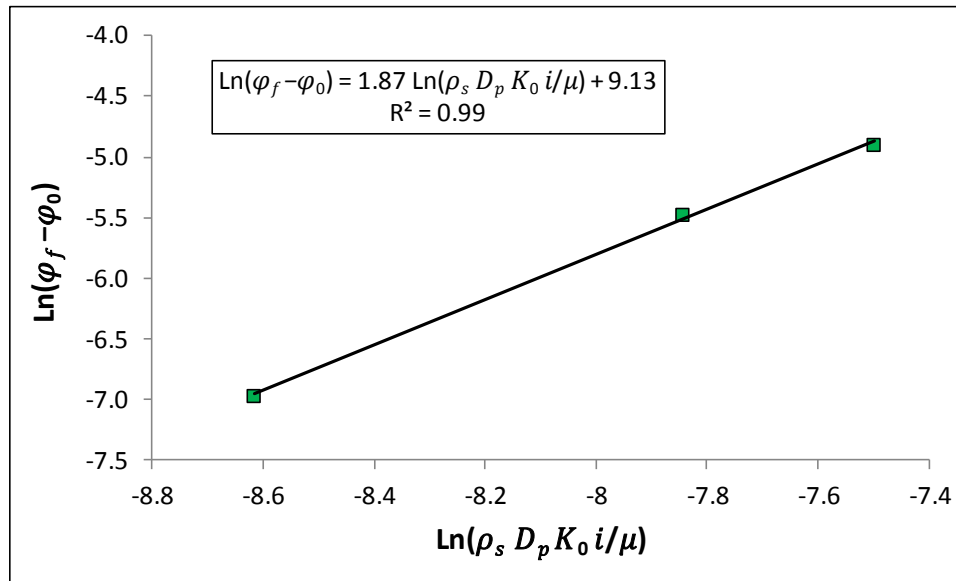


Figure 6-6: Calibrating α and β for Tests 1, 2 and 3, Sterpi (2003)

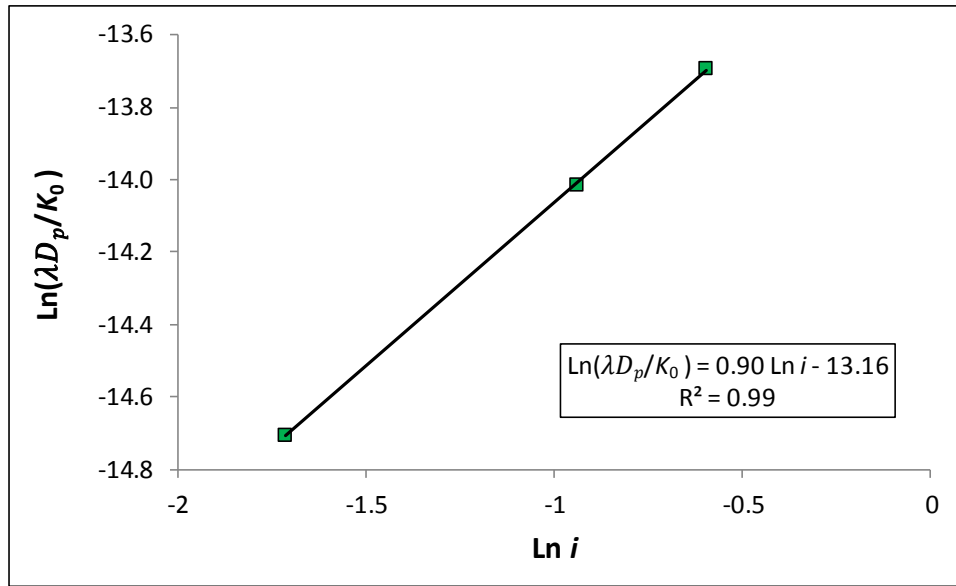


Figure 6-7: Calibrating γ_1 and γ_2 for Tests 1, 2 and 3, Sterpi (2003)

Table 6-3 shows a summary of calibration parameters for Tests 1, 2 and 3.

Table 6-3: Summary of calibration parameters for Tests 1, 2 and 3, Sterpi (2003)

Parameter	Value
α	9228
β	1.87
γ_1	1.93E-6
γ_2	0.90

6.4.2 Variable velocity tests

Experimental data given in Figure 6-2 through Figure 6-5 were used to estimate the values of α , β , γ_1 and γ_2 for variable velocity erosion experiments (GSD1, GSD2 and GSD3). There were seven tests in total for all GSD's. During a preliminary analysis, we realized that the plots related to Eq. (6-17) and Eq. (6-18) for all the variable velocity tests follow the same trend. This could be due to the fact that all the tests have relatively similar grain size distributions. Because of this observation, we decided to calibrate only one set of α , β , γ_1 and γ_2 parameters for all the variable velocity erosion experiments. We used two tests form GSD1 (with hydraulic gradient of 0.30 and 0.7), one tests form GSD2 (with hydraulic

gradient of 0.50) and two tests from GSD3 (with hydraulic gradient of 0.5 and 0.70) for calibrating α , β , γ_1 and γ_2 parameters. The remaining two tests from GSD1 and GSD2 (with the gradients of 0.5 and 0.70, respectively) were used for model validation. Table 6-4 shows other necessary parameters for the estimation of α , β , γ_1 and γ_2 for the tests used in the calibration. In this table, m_{final} is the final value of eroded mass which is estimated from Figure 6-2 through Figure 6-5 for each test. Also in this table, values of the decay coefficient, λ , were estimated using the procedure explained in Chapter 5.

Table 6-4: Required parameters for model calibration, variable velocity tests (GSD1, GSD2 and GSD3)

Test #	Hydraulic gradient	m_{final} , gr	λ , 1/hr	K_0 , m/sec
GSD1-1	0.30	0.1	3.35	0.00014
GSD1-3	0.70	9.5	0.66	0.00024
GSD2-1	0.50	0.6	0.96	0.00017
GSD3-1	0.50	0.23	2.41	0.00009
GSD3-2	0.70	1	1.77	0.00011

Using the data given in Table 6-1 and Table 6-4, we calculated the values of $(\varphi_f - \varphi_0)$, $\left(\frac{\rho_s D_p K_0 i}{\mu}\right)$ and $\left(\frac{\lambda D_p}{K_0}\right)$ for each test. Then we plotted the lines corresponding to Eq. (6-17) and Eq. (6-18) to estimate α , β , γ_1 and γ_2 for the tests listed in Table 6-4. Results are shown in Figure 6-8 and Figure 6-9.

In Figure 6-8 and Figure 6-9, the green squares represent experimental data and the solid line represents the best linear fit. For these figures, linear regression lines were obtained using the method of least squares. The corresponding equation for the linear fit is also shown in these plots along with the value of the coefficient of determination, R^2 .

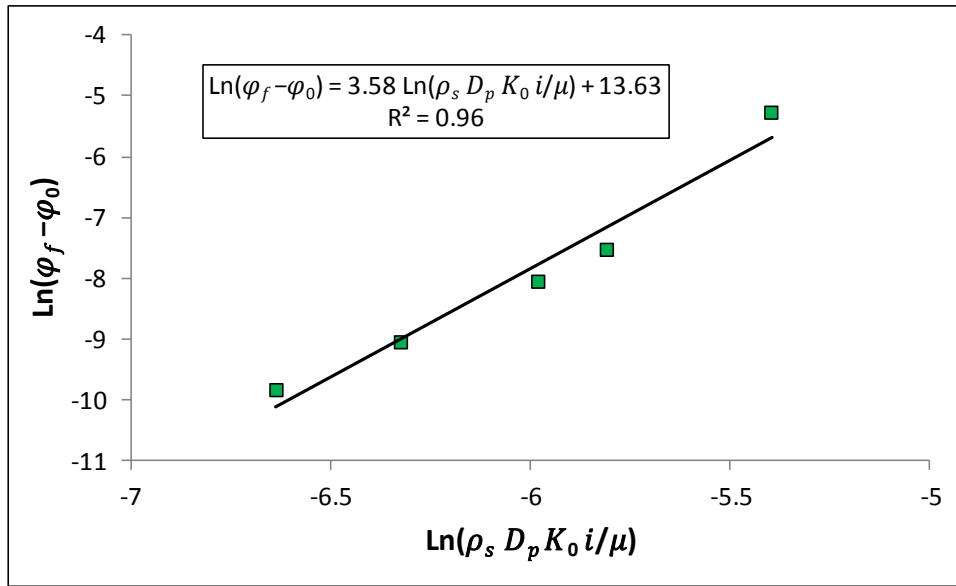


Figure 6-8: Calibrating α and β for variable velocity tests

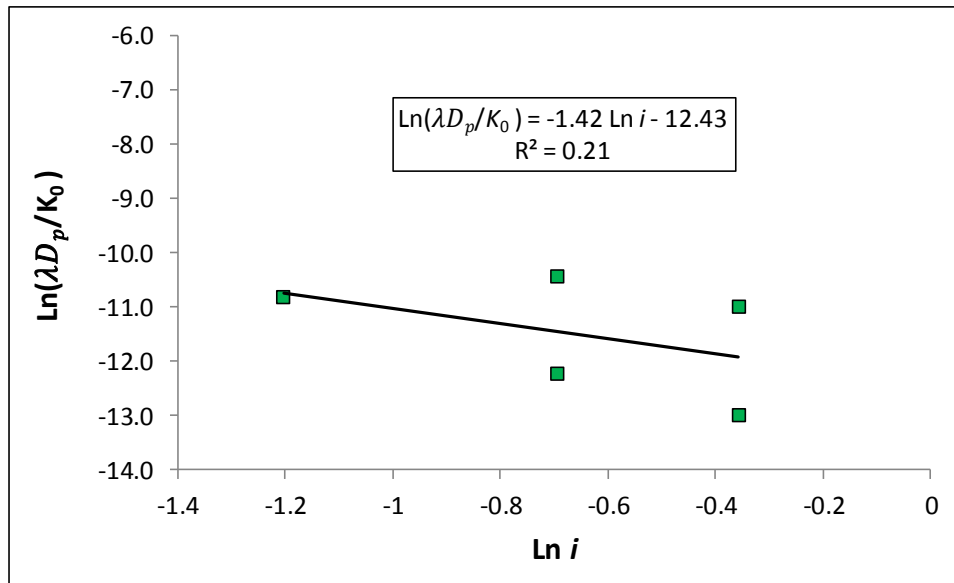


Figure 6-9: Calibrating γ_1 and γ_2 for variable velocity tests

Table 6-5 shows a summary of calibration parameters for variable velocity tests listed in Table 6-4.

Table 6-5: Summary of calibration parameters for variable velocity tests listed in Table 6-4

Parameter	Value
α	830680
β	3.58
γ_1	4.00E-6
γ_2	-1.42

6.5 Model validation

After calibrating the parameters of α , β , γ_1 and γ_2 ; we used Eq. (6-10) and Eq. (6-16) to calculate the parameters of the erosion model (φ_f and λ) for the remaining tests. Then the calculated values of φ_f and λ were used along with Eq. (6-1) to predict the eroded mass for the remaining constant and variable velocity experiments. The validation results are presented below.

6.5.1 Constant velocity tests

The calibrated values of α , β , γ_1 and γ_2 for constant velocity tests (shown in Table 6-3) are used along with Eq. (6-10) and Eq. (6-16) to calculate φ_f and λ for Tests 4 and 5 and the results are shown in Table 6-6.

Table 6-6: Calculated values of φ_f and λ for Tests 4 and 5, Sterpi (2003)

Test #	Hydraulic gradient	φ_f	λ
4	0.60	0.347	0.12
5	0.75	0.351	0.15

Then, the calculated values of φ_f and λ (given in Table 6-6) are used along with Eq. (6-1) to predict the experimental results of Tests 4 and 5 and the comparison between model prediction and experimental results for these tests are shown in Figure 6-10 and Figure 6-11, respectively. These figures show that the model can predict the experimental results with reasonable accuracy.

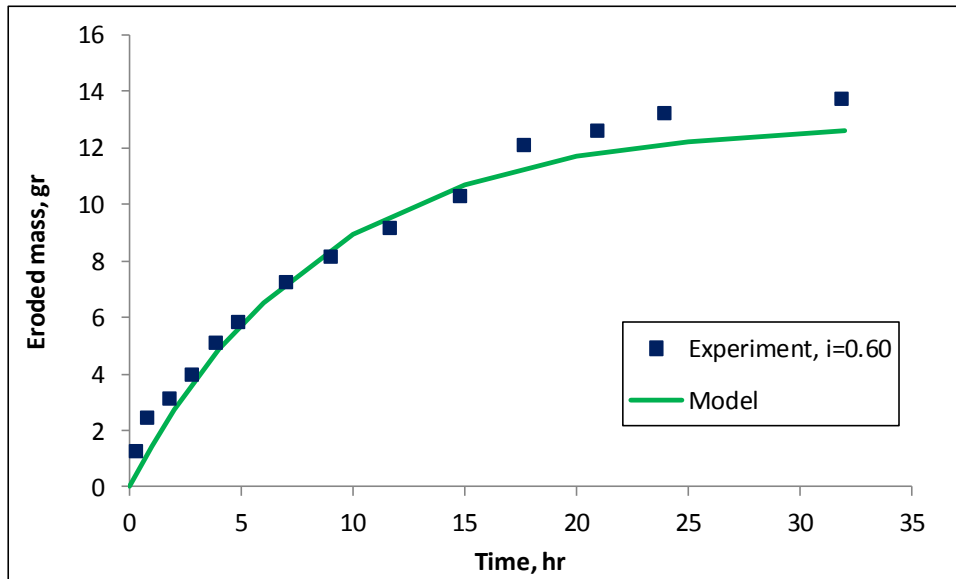


Figure 6-10: Comparison between experimental results and model prediction of eroded mass, Test 4, Sterpi (2003)

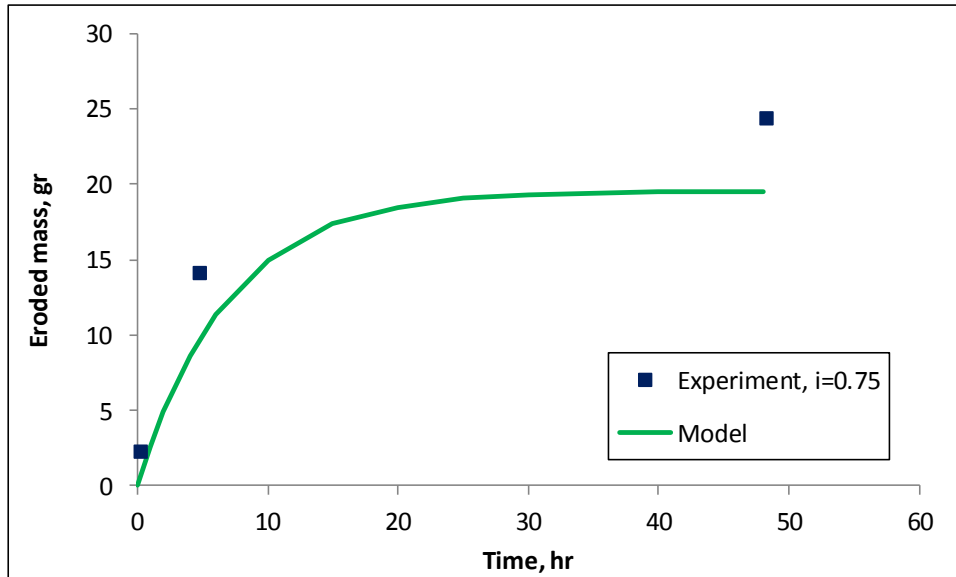


Figure 6-11: Comparison between experimental results and model prediction of eroded mass, Test 5, Sterpi (2003)

6.5.2 Variable velocity tests

Calibrated values of α, β, γ_1 and γ_2 for variable velocity tests (shown in Table 6-5) are used along with Eq. (6-10) and Eq. (6-16) to calculate φ_f and λ for Tests GSD1-2 and GSD2-2 and the results are shown in Table 6-7.

Table 6-7: Calculated values of φ_f and λ for Tests GSD1-2 and GSD2-2

Test #	Hydraulic gradient	φ_f	λ
GSD1-2	0.50	0.4005	2.43
GSD2-2	0.70	0.4021	1.44

Then, the calculated values of φ_f and λ (given in Table 6-7) are used along with Eq. (6-1) to predict the experimental results of Tests GSD1-2 and GSD2-2 and the comparison between model prediction and experimental results for these tests are shown in Figure 6-12 and Figure 6-13 respectively. These figures show that the model can predict the experimental results with reasonable accuracy.

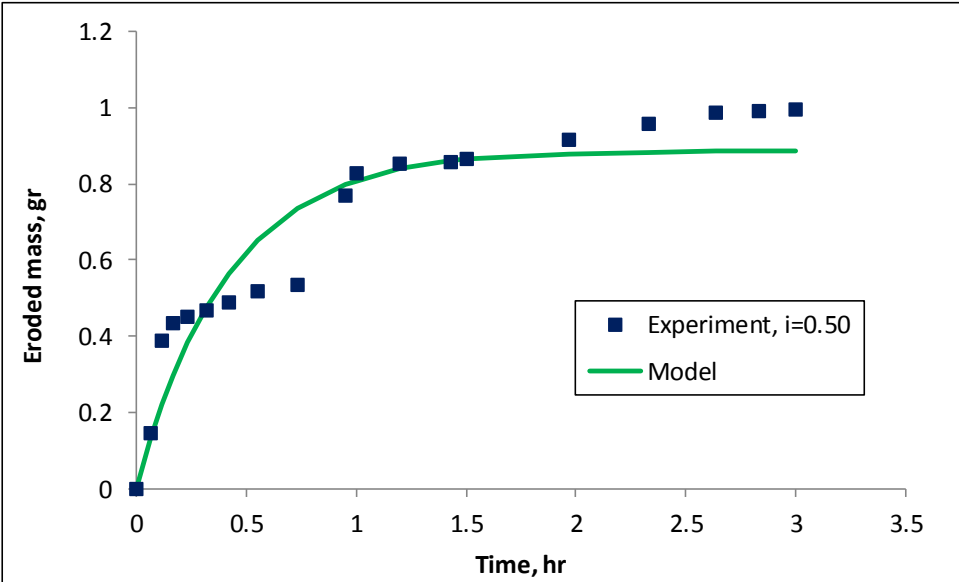


Figure 6-12: Comparison between experimental results and model prediction of eroded mass, Test GSD1-2, $i=0.50$

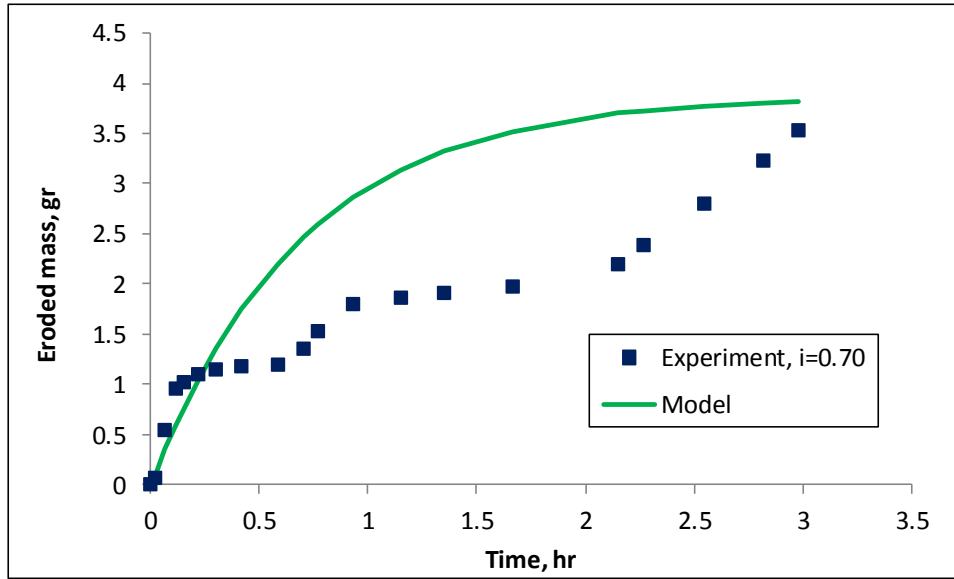


Figure 6-13: Comparison between experimental results and model prediction of eroded mass, Test GDS2-2, $i=0.70$

6.6 Discussion and concluding remarks

Using the principles of dimensional analysis, we developed relationships to estimate the parameters of the erosion model that we proposed in Chapter 5. These parameters are final value of porosity φ_f and decay coefficient λ and the related relationships are shown in Eq. (6-10) and Eq. (6-16), respectively. These relationships have four calibration parameters namely, α , β , γ_1 and γ_2 .

We used two series of experiments for calibration and validation of the proposed relationships. We used constant velocity erosion experiments reported by Sterpi (2003) and also, we used our erosion experiments which were presented in Chapter 4. We calibrated α , β , γ_1 and γ_2 parameters for each group of test separately. After an initial analysis, we decided to calibrate only one set of α , β , γ_1 and γ_2 for variable velocity tests because dimensionless groups in Eq. (6-10) and Eq. (6-16) for these tests would align along the same lines. This could be due to the fact that grain size distributions for all the variable velocity erosion experiments are relatively similar.

The only difference between the calibration results for these two series of tests was that γ_2 had a positive value for Sterpi (2003) tests and a negative value for our experiments. In other words, a higher hydraulic gradient would result in a

higher value of decay coefficient, λ , in Sterpi (2003) experiments and a lower value of λ in our experiments. This result is expected from the experimental observations. By definition, the inverse of λ is the mean lifetime of the erosion process. A higher value of λ implies that the erosion process will end faster and vice versa. As observed in our experiments, higher hydraulic gradients result in an increase in the value of hydraulic conductivity (permeability). A higher hydraulic conductivity means a higher average pore throat diameter which in turn shows itself in the form of a longer erosion process (lower decay coefficient). The reverse of this process is observed for Sterpi (2003) experiments which had a constant hydraulic conductivity for all hydraulic gradients.

As observed above, α , β , γ_1 and γ_2 are material-specific and they need to be calibrated again if we go from one material to another. After calibrating α , β , γ_1 and γ_2 for each series of experiments, the proposed erosion model shown in Eq. (6-1) along with Eq. (6-10) and Eq. (6-16) was validated by predicting the experimental results of Tests 4 and Test 5 of Sterpi (2003) experiments and Tests GSD1-2 and GSD2-2 of our experiments. The validation results show that the model can predict the experimental results with reasonable accuracy.

6.7 Nomenclature

D_p	Average diameter of the eroded particles
i	Hydraulic gradient
K_0	Initial value of hydraulic conductivity
m_{er}	Eroded mass per unit volume
m_f	Final value of eroded mass per unit volume
m_{final}	Final value of eroded mass
t	Time
t_0	Starting time of erosion
$\alpha, \beta, \gamma_1, \gamma_2$	Dimensionless calibration parameters

λ	Decay coefficient (Erosion coefficient)
μ	Fluid viscosity
ρ_s	Grain density
φ_0	Initial porosity
φ_f	Final porosity

6.8 References

- David, F. W. and Nolle, H., 1982. *Experimental Modelling in Engineering*, Butterworths.
- Hornung, H., G., 2006. *Dimensional Analysis: Examples of the Use of Symmetry*, Dover publications, ISBN: 0486446050
- Stepi, D., 2003. Effect of the erosion and transport of fine particles due to seepage flow. *Int. J. Geomech.*, Vol. 3, No., 1, pp. 111–122.

Chapter 7

Concluding Remarks

Our research was focused on the development of a constitutive law for the internal erosion phenomenon in unconsolidated porous media. We used a combination of analytical and experimental modeling approaches to achieve this goal. In this chapter, the main contributions of our research are presented first followed by some recommendations for further research.

7.1 Main contributions

Main contributions of our work are as follows:

1. Using the principles of dimensional analysis, a mathematical relationship was derived for the assessment of the rate of internal erosion in relation to the fluid velocity. This relationship has a proportionality constant called the erosion coefficient (λ) which is proposed to be a function of grain density, particle Reynolds number and porosity changes. We used a series of erosion experiments on a silty-sand, which were available in the literature, to establish the functional relationship between λ and other parameters. The advantage of the proposed erosion model is that it offers a functional form for the erosion coefficient. This functional form shows that erosion coefficient is directly proportional to particle Reynolds number and inversely proportional to porosity variations. These findings had not been explicitly expressed in previous works. The suggested model has three

calibration parameters. The model was calibrated and validated using experimental data. The validation results show that the model is able to predict the experimental erosion rates with reasonable accuracy. Working on this model was a preliminary step towards the development of our main erosion model which we proposed in Chapters 5 and 6.

2. Due to lack of sufficient experimental data for model calibration and validation, we designed and built an experimental apparatus to conduct internal erosion tests. We used unconsolidated test specimens which were prepared by mixing different proportions of coarse sand, fine sand and silt. Our test results show consistent trends. We get more erosion for poorly graded grain size distributions and for higher hydraulic gradients. The key measurements during each test were fluid pressure, fluid flow rate and turbidity of the effluent. In this way, it was possible to measure the eroded mass and, also, the effect of internal erosion on the permeability of the test specimens.
3. Based on the observations from our experimental results, we developed a constitutive law to model internal erosion as an exponential decay process. The proposed constitutive law was calibrated using the test data we gathered in our experimental program as well as some test data that we obtained from literature. The results of this analysis show that internal erosion is, indeed, an exponential decay phenomenon. The advantage of this model, compared to the model that we developed using dimensional analysis technique, is that it has a better description of the *physics* of internal erosion. Many phenomena in nature follow the exponential decay law and such constitutive relationships are well known for scientists and engineers.
4. The constitutive law for erosion based on exponential decay formulations has two calibration parameters. These parameters are the final value of porosity, φ_f and the decay coefficient (or erosion coefficient), λ . In order to use this model as a predictive tool, one needs to develop relations for φ_f and λ as functions of independent experimental and material parameters such as hydraulic gradient (fluid velocity), hydraulic conductivity

(permeability) and mean grain diameter. We have used dimensional analysis approach (similar to the procedure used in Chapter 3) to develop such relationships for the estimation of these parameters. The proposed relationships were calibrated and validated using experimental data and the validation results show that the proposed relationships can predict φ_f and λ with reasonable accuracy.

7.2 Recommendations for further research

This work can be further enhanced from both aspects of analytical and experimental modeling. The following recommendations point out the potential areas of further research on the topic of constitutive modeling of erosion process:

1. One of the limitations of the constitutive law based on dimensional analysis is that erosion is assumed to be uniform throughout the test specimen. In other words, this model assumes that porosity changes homogeneously in the test sample. However, it is very likely that erosion will be more intense close to the free surface of the test sample resulting in an inhomogeneous porosity field. Erosion experiments on test specimens of different heights are required to assess the severity of this phenomenon and its effect on the test results and model predictions.
2. Also, in the constitutive law based on dimensional analysis approach, it was assumed that the parameter D_p , which is the average size of the eroded particles, is constant for all hydraulic gradients. The reason for this assumption is that we do not know the value of D_p *a priori* unless we perform the erosion experiments and analyze the size of eroded particles. This may not be a realistic assumption since higher hydraulic gradients can mobilize larger size particles and generally, D_p can vary from one test to another. To overcome this limitation, a relationship can be established, experimentally, between fluid velocity (hydraulic gradient) and the average size of the eroded particles for materials with different properties (i.e., porosity, permeability, grain size distribution, etc.). Then such a correlation

can be used to assign more realistic values of the D_p parameter in the proposed erosion model.

3. Further improvements to the experimental program can be suggested as follows. This improvements can help us to get a better picture of the physics behind the internal erosion process:

- Local permeability measurements. This means measurement of permeability at different points along the height of the test specimen. By doing so, it is possible to observe the localized impact of erosion on permeability and to see how uniformly permeability changes during the erosion process.
- Post-mortem analysis of the test specimen. After each test, samples can be taken along the height of the specimen to determine the GSD and fine content to come up with the fine concentration or difference thereof from the initial concentration. The results can be used to correlate the severity of erosion in different regions to their respective permeability.
- Experimental quantification of the erosion boundary. It would be interesting to know what distance the particles have to travel in order to erode out of the test specimen. In other words, it would be beneficial to know the depth beyond which erosion doesn't occur. This can be achieved by using differently colored particles at different heights (in the case of a vertical set-up) of the test specimen. This will allow using more realistic values for V_{EB} in the proposed constitutive model in Chapter 3.
- Testing the effect of apparatus orientation on experimental results. This will be helpful to quantify the effect of gravity on experiment outcome and can be achieved by performing erosion tests in horizontal and downward fluid flow conditions.
- Assessing the effect of confining pressure on erosion behavior of porous media. This can be done by performing internal erosion tests in a customized soil/rock triaxial test apparatus.

- Our erosion experiments had durations of a few hours which may not be sufficient to ensure the end of the erosion process. It is recommended to conduct internal erosion experiments for longer durations (several hours to few days) to observe the long-term erosion behavior of the porous media and to ensure that the erosion process is terminated (which is necessary for a realistic assessment of φ_f).
4. It is recommended to experimentally study the validity of the proposed dimensionless groups. In our work, we have only studied the effect of variation of hydraulic gradient on the dependent parameters (eroded mass or porosity). Validity of the proposed dimensionless groups can be studied by changing another independent parameter, such as fluid viscosity, and examining if the same behavior is observed in the dependent parameters or not.
 5. It will be interesting to study, experimentally, the process of particle deposition (which is the opposite of particle erosion) to see if the same trends are observed. It will be of particular interest to observe if particle deposition also follows the exponential decay law or not. Such experiments and analysis will help to complete the picture we have for internal erosion process.

Bibliography

- Abrams, A., 1977. Mud Design to Minimize Rock Impairment Due to Particle Invasion, JPT, pp. 586-592.
- Adel, H. den, Bakker, K. J. and Breteler, M. K. 1988. Internal stability of minestone. Proc. Int. Symp. Modelling Soil-Water-Structure Interaction, pp. 225-231. Rotterdam: Balkema.
- Adel, H. den, Koenders, M. and Bakker, K.J. 1994. The analysis of relaxed criteria for erosion-control filters. Canadian Geotechnical Journal (CGJ), Vol. 31, No. 6, pp. 829-840.
- ASCE, 1936. Filter sand for water purification plants. Proc. ASCE, No. 62, pp. 1543-1580
- Asgian, M.I., Cundall, P.A., and Brady, B.H.G., 1995. The mechanical stability of propped hydraulic fractures; a numerical study, J. of Pet. Tech., March, pp. 203-208.
- Baylis J. R., 1937. Experiences in filtration. J. of Amer. Water Works Ass., No. 29, pp. 1010-1048.
- Briaud, J.L., Ting, F. C. K., Chen, H. C., Gudavalli, R., Perugu, S. and Wei, G., 1999. SRICOS: Prediction of Scour Rate in Cohesive Soils at Bridge Piers, Journal of Geotechnical and Geoenvironmental Engineering, Vol. 125, No.4, pp. 237-246.
- Briaud, J. L., Ting, F. C. K., Chen, H. C., Cao, Y., Han, S. W., and Kwak, K. W. 2001. Erosion function apparatus for scour rate predictions. Journal of Geotechnical and Geoenvironmental Engineering, Vol. 127, No. 2, pp. 105–113.
- Charlez, Ph. A., 1997. Rock Mechanics: Petroleum Applications. Vol. 2, Editions Technip.
- Chenault, R. L., 1938. Experiments on fluid capacity and plugging of oil-well screens, American Petroleum Institute, API-38-293.

- Cividini, A. and Gioda, G., 2004. Finite element approach to the erosion and transport of fine particles in granular soils. *Int. J. Geomech.*, Vol. 4, No 3, pp.191–198.
- Cividini, A., Bonomi, S., Vignati, G.C. and Gioda G., 2009. Seepage-induced erosion in granular soil and consequent settlements. *Int. J. Geomech.*, Vol. 9, No. 4, pp. 187–194.
- Coberly, C. J., 1937. Selection of screen openings for unconsolidated sands, American Petroleum Institute, API-37-189.
- David, F. W. and Nolle, H., 1982. *Experimental Modelling in Engineering*, Butterworths.
- de Gaauw, A., Van Der Meulen, T. and Van Der Does De Bye, M., 1984. Design Criteria for Granular Filters, *J. Waterway, Port, Coastal, Ocean Eng.* Vol. 110, No. 1, pp. 80-96.
- Detournay, C., Tan, C. and Wu, B., 2006. Modeling the mechanism and rate of sand production using FLAC, *The 4th International FLAC Symposium on Numerical Modeling in Geomechanics*, paper: 08-10.
- Fjaer, E., Cerasi, P., Li, L. and Papamichos, P., 2004. Modeling the rate of sand production, *The 6th North America Rock Mechanics Symposium (NARMS)*, Houston, Texas, USA, June 5–9.
- Gruesbeck, C. and Collins, R. E., 1982. Entrainment and deposition of fine particles in porous media, *Soc. Pet. Eng. J.*, pp. 847-856.
- Guo, S., Shao, Y., Zhang, T., Zhu, D., and Zhang, Y., 2013. Physical modeling on sand erosion around defective sewer pipes under the influence of groundwater, *J. Hydraul. Eng.*, Vol. 139, No. 12, pp. 1247–1257.
- Hornung, H., G., 2006. *Dimensional Analysis: Examples of the Use of Symmetry*, Dover publications, ISBN: 0486446050
- Indraratna, B., Muttuvel, T., Khabbaz, H. and Armstrong, R., 2008. Predicting the Erosion Rate of Chemically Treated Soil Using a Process Simulation Apparatus for Internal Crack Erosion, *J. Geotech. Geoenviron. Eng.*, Vol. 134, No. 6, pp. 837-844.

- Indraratna, B., Athukorala, R., and Vinod, J., 2013. Estimating the Rate of Erosion of a Silty Sand Treated with Lignosulfonate, *J. Geotech. Geoenviron. Eng.*, Vol. 139, No. 5, pp. 701-714.
- Iwasaki, T. 1937. Some Notes on sand filtration, *J. of Amer. Water Works Ass.*, Vol. 29, No. 10, pp.1591-1602.
- Kenney, T. C., and Lau, D., 1985. Internal stability of granular filters. *Can. Geotech. J.*, Vol. 22, No. 2, pp. 215–225.
- Khilar, K. C. and Fogler, H. S., 1983. Water sensitivity of sandstones, *Soc. Pet. Eng. J.*, Vol. 23, No. 1, pp. 55-64
- Khilar, K. C. and Fogler, H. S., 1987. Colloidally induced fines migration in porous media, *Rev. Chem. Eng.*, Vol. 4, No.1, pp. 43-67.
- Khilar, K.C., and Fogler, H.S., 1998, *Migration of Fines in Porous Media*. Kluwer Academic Publishers.
- Kovacs, G., 1981. *Seepage hydraulics*, Elsevier Scientific.
- Ladd, R. S. 1978. Preparing test specimen using under compaction. *Geotech. Testing J.*, Vol. 1, pp. 16–23.
- Li, K., 2000. Fines migration and other aspects of recovery of crude oil by waterflooding, MSc thesis, University of Wyoming, USA.
- Muecke, T. W., 1979. Formation of fines and factors controlling their movement in porous media, *JPT*, pp. 144-50.
- Nguyen, V. T., 2012. Flow through filters in embankment dams, PhD thesis, University of Wolongong, Australia.
- Papamichos, E., and Malmanger, E.M, 1999. A sand erosion model for volumetric sand predictions in a North Sea reservoir, *SPE Latin American and Caribbean Petroleum Engineering Conference*, Caracas, Venezuela, 21-23 April.
- Papamichos, E., Vardoulakis, I., Tronvoll, J. and Skjaerstein, A., 2001. Volumetric sand production model and experiment, *International Journal for Numerical and Analytical Methods in Geomechanics*, Vol. 25, No. 8, pp. 789-808.

- Papamichos, E. and Vardoulakis, I., 2005. Sand erosion with a porosity diffusion law, *International Journal of Computers and Geotechnics*, Vol. 32, No. 1, pp. 47-58.
- Papamichos, E., 2010. Erosion and multiphase flow in porous media. Application to sand production, Special issue of *European Journal of Environmental and Civil Engineering*, Vol. 14/8-9, pp. 1129-1154.
- Penberthy, W.L. Jr. and Shaughnessy, C.M., 1992. Sand control, Vol. 1, SPE Monograph Series, Richardson, Texas.
- Sakthivadivel, R. and Irmay, S., 1966. A review of filtration theories, HEL 15-4. University of California, Berkeley
- Sakthivadivel, R. 1967. Theory and mechanism of filtration of non-colloidal fines through a porous medium, PhD thesis. University of California, Berkeley
- Saucier, R. J., 1974. Considerations in gravel pack design, *Journal of Petroleum Technology*, Vol. 26, No. 2, pp. 205-212.
- Selby, R. J., and Ali, S. M. F., 1988. Mechanics of sand production and the flow of fines in porous media, *Journal of Canadian Petroleum Technology*, Vol. 27, No. 3, pp. 55-63.
- Servant, G., Marchina, P., Peysson, Y., Bemmer, E. and Nauroy, J., 2006. Sand erosion in weakly consolidated reservoirs: Experiments and numerical modeling, SPE/DOE Symposium on Improved Oil Recovery, Tulsa, OK, USA, April 22-26.
- Skempton, A. W. and Brogan, J. M., 1994. Experiments on piping in sandy gravels, *Geotechnique*, Vol. 44, No. 3, pp. 449-460.
- Skjaerstein, A., Stavropoulou, M., Vardoulakis, I., Tronvoll, J., 1997. Hydrodynamic erosion; A potential mechanism of sand production in weak sandstones, *International Journal of Rock Mechanics and Mining Sciences*, Vol. 34, No. 3-4, pp. 292.e1-292.e18.
- Stavropoulou, M., Papanastasiou, P., and Vardoulakis, I., 1998. Coupled wellbore erosion and stability analysis, *Int. J. Numer. Anal. Meth. Geomech.*, Vol. 22, pp. 749-769.
- Sterpi, D., 2003. Effect of the erosion and transport of fine particles due to seepage flow. *Int. J. Geomech.*, Vol. 3, No., 1, pp. 111-122.

- Uno, T., Kamiya, K., Matsushima, T., 1996. The Relationships between Particle Size and Void Diameter for Sand, Proceedings of the Second International Geofilters Conference, pp. 67-74.
- Vaidya, R. N., 1991. Fines migration and formation damage, PhD thesis, University of Michigan, USA.
- Vardoulakis, I., Stavropoulou, M. and Papanastasiou, P. 1996. Hydro-mechanical aspects of the sand production problem, *Journal of Transport in Porous Media*, Vol. 22, No. 2, pp. 225-244.
- Vardoulakis, I., 2006. Sand production, *Rev. Europ. de Génie Civil*, Vol. 10, No. 6-7, pp. 817-828.
- Vaziri, H., Barree, B., Xiao, Y., Palmer, I., Kutas, M., 2002. What is the magic of water in producing sand, SPE Annual Technical Conference and Exhibition, San Antonio, Texas, USA, 29 September - 2 October.
- Veeken, C.A.M., Davies, D.R., Kenter, C.J., Kooijman, A.P., 1991. Sand production prediction review: developing an integrated approach, Proceedings of the SPE Annual Technical Conference and Exhibition, Dallas, Texas, USA. 6 – 9 October.
- Wan, C.F. and Fell., R., 2004. Investigation of erosion of soils in embankment dams, *J. Geotech. Geoenviron. Eng.*, Vol. 130, No. 4, pp. 373–380.
- Wilhelm, Th., 2000. Piping in Saturated Granular Media, Ph.D. Thesis, University of Innsbruck
- Wilson, C. S., 1933. Selection and use of screened pipe, *Transactions of the AIME*, Vol. 103, No. 1, pp. 116-135.
- Worman, A. and Olafsdottir, R., 1992. Erosion in a granular medium interface. *J. Hydraul. Res.*, Vol. 30, No. 5, pp. 639–655
- Wu, B., Tan, C. P., 2001. Effect of water-cut on sandstone strength and implications in sand production prediction. 38th U.S. Symposium on Rock Mechanics (USRMS), Washington D.C., USA, July 7-10.

Appendix A

Modification of Erosion Constitutive Law Based on Dimensional Analysis Technique with Tangent Erosion Rate

A.1. Introduction

In Chapter 3, a constitutive model was proposed for the estimation of internal erosion rate in porous media. In that model, the erosion rate was calculated using secant slope of the experimental data. The reason for using secant erosion rate instead of tangent rate was to eliminate the effects of transient phenomena (such as pore clogging and unclogging) on data trends.

In this appendix, we try to use the same procedure used in Chapter 3 to reformulate the proposed model based on tangent erosion rate. Tangent erosion rate for each point can be calculated using backward, forward, or central difference schemes. In order to minimize the effect of transient phenomena, the tangent erosion rates for all points in each test are calculated using the central difference scheme with the exception of the last point, which is calculated using the backward difference scheme.

A.2. Mathematical modeling

In a similar manner as in Chapter 3, the modified constitutive law for particle erosion rate in porous media is presented using the principles of dimensional analysis. As stated above, the only difference between this model and the model presented in Chapter 3 is that secant erosion rate, m' , is replaced with tangent erosion rate \dot{m} . Also, as mentioned before, the tangent erosion rate for each point in all tests is calculated using the central difference scheme.

In this modified model, similar to the model presented in Chapter 3, the critical fluid velocity is calculated using Eq. (3-27).

We start with the following relationship to relate total eroded mass to most relevant parameters such as grain density, porosity variation, mean size of eroded particles, fluid velocity and fluid viscosity.

$$m = f[(v_f - v_{cr}), D_p, \mu, \rho_s, (\varphi - \varphi_0), (t - t_0), V_{EB}] \quad (\text{A-1})$$

All the parameters in the equation above have the same definitions as of those in Chapter 3. If the eroded mass is expressed as time rate and is normalized by the volume of erosion boundary, then Eq. (A-1) is reduced to:

$$\dot{m} = f[(v_f - v_{cr}), D_p, \mu, \rho_s, (\varphi - \varphi_0)] \quad (\text{A-2})$$

In equation above, \dot{m} is the instantaneous mass rate of eroded particles per unit volume.

Following the same procedure and using Eq. (3-7), (3-8) and (3-9), the parameters in Eq. (A-2) are nondimensionalized one by one.

$$[\dot{m}] = [ML^{-3}T^{-1}] = \left[(\rho_s D_p^3)(D_p)^{-3} \left[\frac{D_p}{(v_f - v_{cr})} \right]^{-1} \right] = \left[\frac{\rho_s(v_f - v_{cr})}{D_p} \right] \quad (\text{A-3})$$

$$[\mu] = [ML^{-1} T^{-1}] = \left[(\rho_s D_p^3)(D_p)^{-1} \left[\frac{D_p}{(v_f - v_{cr})} \right]^{-1} \right] = [\rho_s D_p (v_f - v_{cr})] \quad (\text{A-4})$$

The third dimensionless parameter is selected to be $(\varphi - \varphi_0)$.

Using Eq. (A-3) and (A-4) and parameter $(\varphi - \varphi_0)$, Eq. (A-2) can be written in the following form:

$$\frac{D_p \dot{m}}{\rho_s (v_f - v_{cr})} = g \left[\frac{\rho_s D_p (v_f - v_{cr})}{\mu}, (\varphi - \varphi_0) \right] = g \left[\frac{G_s \rho_f D_p (v_f - v_{cr})}{\mu}, (\varphi - \varphi_0) \right] \quad (\text{A-5})$$

Using the definition of Reynolds number for a particle of diameter D_p , we have:

$$\frac{D_p \dot{m}}{\rho_s (v_f - v_{cr})} = g [G_s (Rp - Rp_{cr}), (\varphi - \varphi_0)] \quad (\text{A-6})$$

Eq. (A-6) can be further simplified into the following form:

$$\dot{m} = \frac{\lambda \rho_s (v_f - v_{cr})}{D_p} \quad (\text{A-7})$$

where, λ is the erosion coefficient and is represented by the following equation:

$$\lambda = g [G_s (Rp - Rp_{cr}), (\varphi - \varphi_0)] \quad (\text{A-8})$$

Equations (A-7) and (A-8) should satisfy the principle of conservation of mass. For an internal erosion problem, the principle of conservation of mass can be simplified into the following equation:

$$\rho_s \frac{\partial \varphi}{\partial t} = \dot{m} \quad (\text{A-9})$$

Where \dot{m} is the mass generation term and expresses *tangent* erosion rate per unit volume.

A.3. Experimental data and model calibration

Same data as in Chapter 3 were used to determine the functional form for the erosion parameter (λ) given by Eq. (A-8). The actual functional form of λ is unknown but based on experimental observations, we know that λ is directly proportional to fluid velocity and inversely proportional to porosity change,

$(\varphi - \varphi_0)$. Having these observations and using the approximation theory, the functional form of λ can be approximated using the equation below:

$$\lambda = \alpha \left[\frac{G_S(Rp - Rp_{cr})}{\varphi - \varphi_0} \right]^\beta \quad (\text{A-10})$$

where α and β are dimensionless calibration parameters.

Let's define ω as:

$$\omega = \frac{G_S(Rp - Rp_{cr})}{\varphi - \varphi_0} \quad (\text{A-11})$$

Then Eq. (A-10) can be simplified to:

$$\lambda = \alpha \omega^\beta \quad (\text{A-12})$$

If we take the natural log of from both sides of Eq. (A-12), we have:

$$\ln \lambda = \ln \alpha + \beta \ln \omega \quad (\text{A-13})$$

Therefore, if we plot $\ln \lambda$ versus $\ln \omega$, $\ln \alpha$ will be the intercept and β will be the slope of the line. Experimental data given in Figure 3-2 were used to estimate the values of α and β for each test.

For each test, the eroded mass is calculated using Eq. (3-35) and is normalized by the volume of the sample and is plotted as a function of time. The values for \dot{m} for each point in Figure 3-2 are calculated using the following formula:

$$\dot{m}_i = \frac{m_{i+1} - m_{i-1}}{(t_{i+1} - t_{i-1})V_{EB}} \quad (\text{A-14})$$

where \dot{m}_i is the tangent erosion rate for i^{th} point, m_{i+1} and t_{i+1} are eroded mass and time for $(i+1)^{\text{th}}$ point and m_{i-1} and t_{i-1} are eroded mass and time for $(i-1)^{\text{th}}$ point and V_{EB} is the volume of the erosion boundary (test specimen).

In Eq. (A-11), $\varphi - \varphi_0$ is calculated using Eq. (3-36). Also, the procedure for calculation of D_p is similar to the one used in Chapter 3.

Based on the approach discussed above and by using Eq. (A-7) and Eq. (A-11), the corresponding values of λ and ω for each test can be obtained from the experimental data. Tests 1, 2 and 3 were used to determine the material parameters and Tests 4 and 5 were used to validate the proposed model. Figure A-1 through Figure A-3 show the plots of $\ln \lambda$ versus $\ln \omega$ for Tests 1, 2 and 3, respectively.

In Figure A-1 through Figure A-3, the green diamonds represent experimental data and the solid line represents the best linear fit (least square method). The corresponding equation for the linear fit is also shown in these plots along with the value of coefficient of determination, R^2 . Also, in these figures, the upper-right data points correspond to the start of the test and lower-left data points correspond to the end of the test.

As mentioned in Chapter 3, in Test 2, there was a sudden increase in fluid velocity after 5 hours. Since we need the value of fluid velocity to calculate λ and ω but we didn't have the value of velocity after 5 hours in this test, only data points up to 5 hours after the start of the test were used in calibration of α and β (Figure A-2).

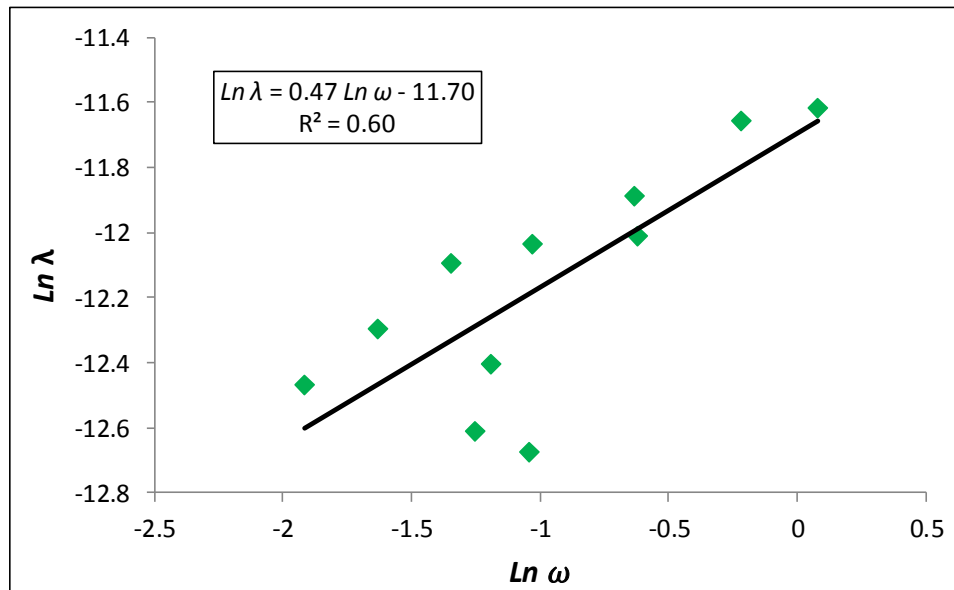


Figure A-1: Calibrating model parameters for Test 1 ($i=0.18$)

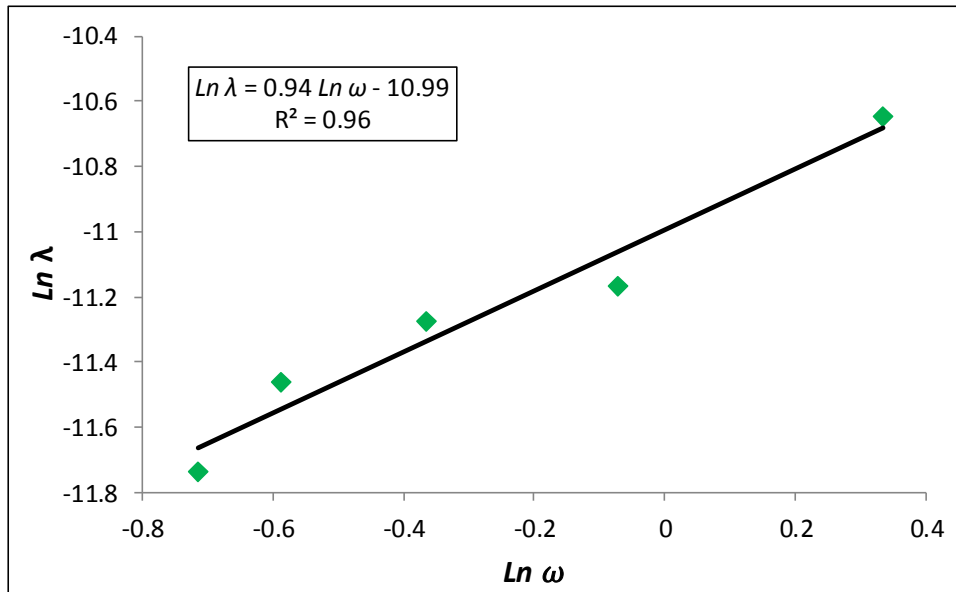


Figure A-2: Calibrating model parameters for Test 2 ($i=0.39$)

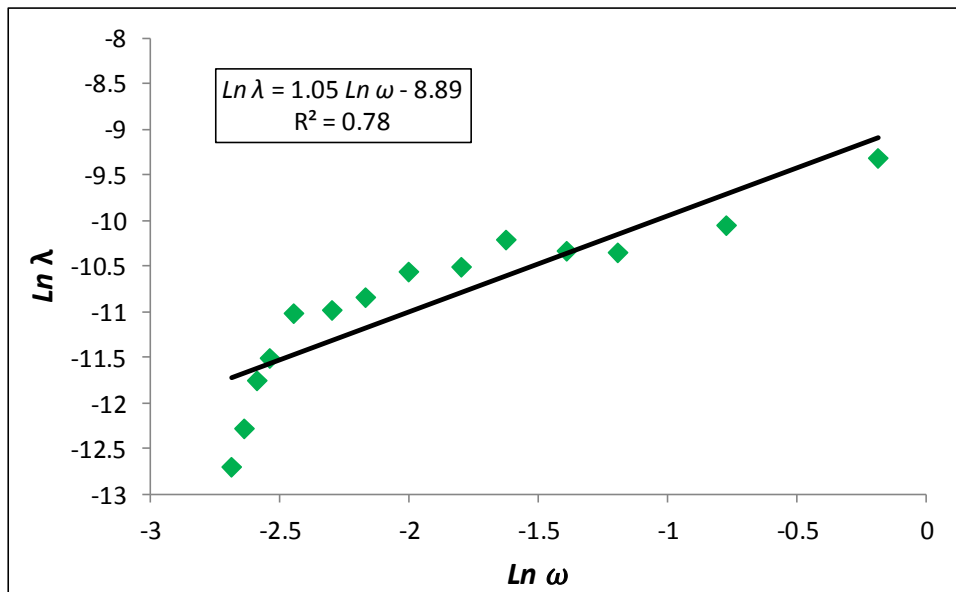


Figure A-3: Calibrating model parameters for Test 3 ($i=0.55$)

Table A-1 shows a summary of calibration parameters for Tests 1, 2 and 3.

Table A-1: Summary of calibration parameters for Tests 1, 2 and 3

Test #	Hydraulic gradient	α	β
1	0.18	8.29E-6	0.47
2	0.39	1.69E-5	0.94
3	0.55	1.38E-4	1.05

After calibrating the erosion coefficient, λ , for each test, Eq. (A-7), Eq. (A-9) and Eq. (A-10) are used together to obtain an analytical relationship for the instantaneous rate of erosion. After some rearrangement we have:

$$\frac{\partial \varphi}{\partial t} = \alpha \left[\frac{G_s(Rp - Rp_{cr})}{\varphi - \varphi_0} \right]^\beta \frac{(v_f - v_{cr})}{D_p} \quad (\text{A-15})$$

After integration and simplification, an analytical relationship for porosity variation, $\varphi - \varphi_0$, is obtained in the following form:

$$\varphi - \varphi_0 = \left[\frac{\alpha (\beta + 1) G_s^\beta (Re_p - Re_{p,cr})^\beta (v_f - v_{cr}) (t - t_0)}{D_p} \right]^{\frac{1}{(\beta+1)}} \quad (\text{A-16})$$

Using Eq. (A-9), the following relationship is obtained for \dot{m} :

$$\dot{m} = K(t - t_0)^{\frac{-\beta}{(\beta+1)}} \quad (\text{A-17})$$

where K is

$$K = \rho_s \frac{1}{(\beta+1)} \left[\frac{\alpha (\beta+1) G_s^\beta (Re_p - Re_{p,cr})^\beta (v_f - v_{cr})}{D_p} \right]^{\frac{1}{(\beta+1)}} \quad (\text{A-18})$$

As mentioned before, data from Tests 1, 2 and 3 were used for model calibration. Comparisons between the experimental and calculated values of tangent erosion rate for these three tests are shown in Figure A-4 to Figure A-6. In these figures, analytical values of erosion rate were calculated by using Eq. (A-17) and the data given in Table 3-1 and Table A-1.

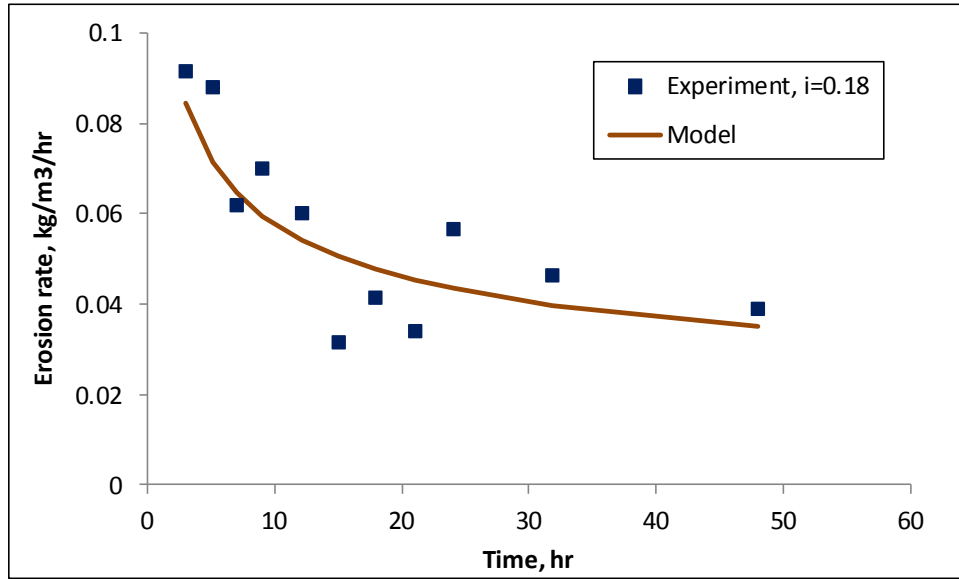


Figure A-4: Comparison between experimental and calculated values of tangent erosion rate, $i=0.18$

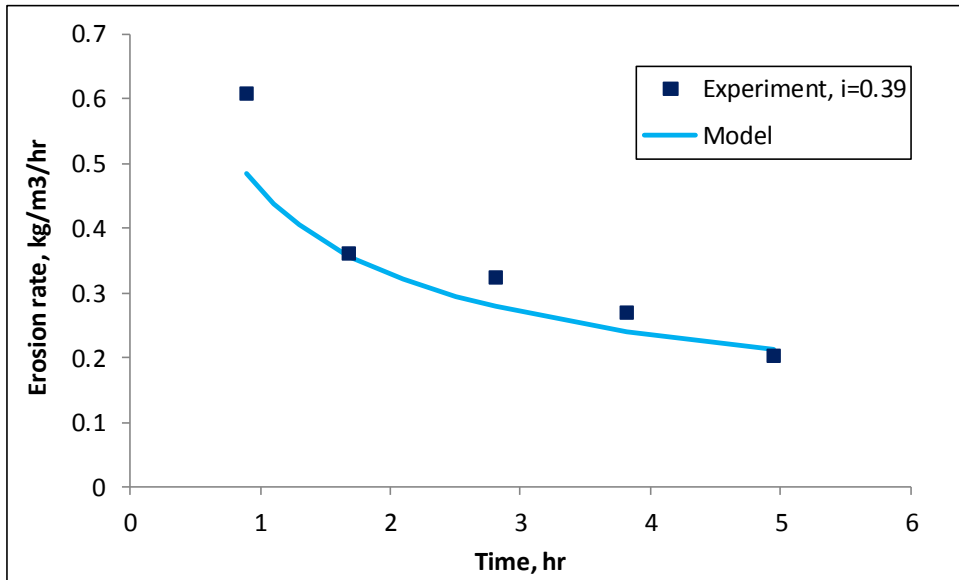


Figure A-5: Comparison between experimental and calculated values of tangent erosion rate, $i=0.39$

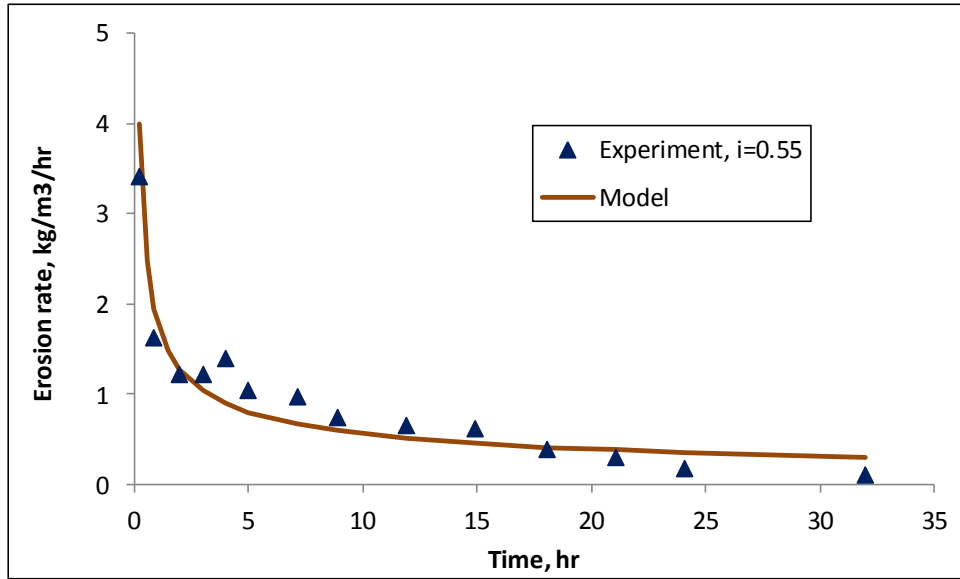


Figure A-6: Comparison between experimental and calculated values of tangent erosion rate, $i=0.55$

A.4. Model validation

Table A-1 shows that α and β vary with hydraulic gradient. We used the data given in this table to examine the relationship between α and β and hydraulic gradient for Tests 1, 2 and 3 and the results are shown in Figure A-7 and Figure A-8.

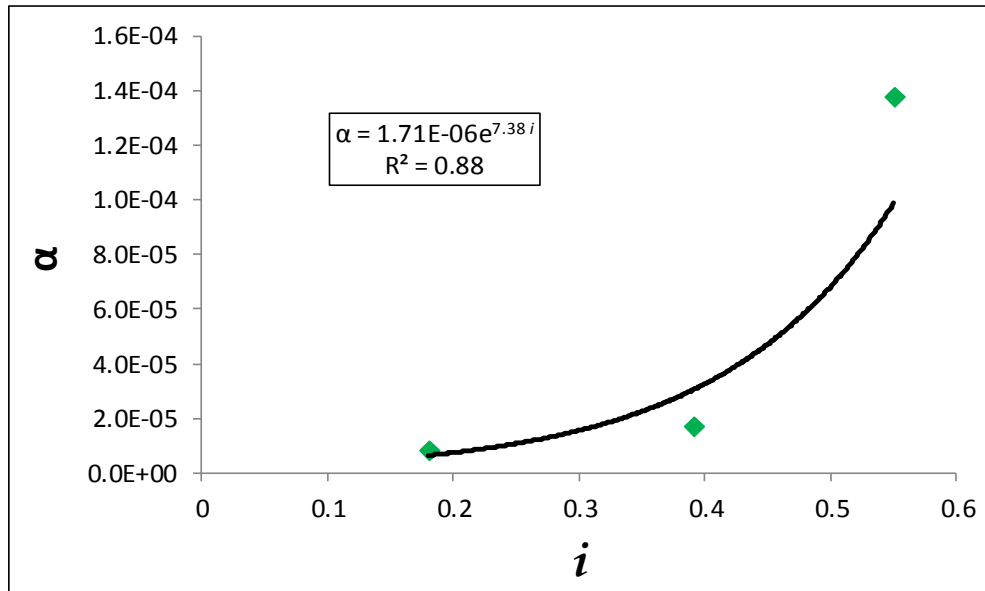


Figure A-7: Variation of α with hydraulic gradient for Tests 1, 2 and 3 and best fit (solid line)

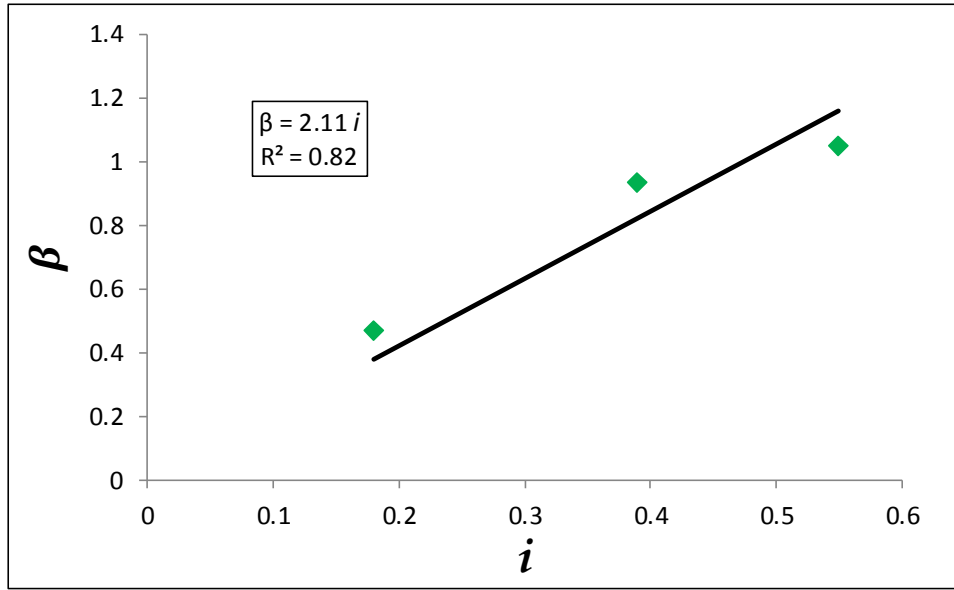


Figure A-8: Variation of β with hydraulic gradient for Tests 1, 2 and 3 and best fit (solid line)

Figure A-7 shows that α varies exponentially with hydraulic gradient and Figure A-8 suggests that the relationship between β and hydraulic gradient is linear. Therefore, based on the trends observed in figures above, the following relationships are suggested for variation of α and β with hydraulic gradient.

$$\alpha = \gamma_1 e^{\gamma_2 i} \quad (\text{A-19})$$

$$\beta = \gamma_3 i \quad (\text{A-20})$$

In Eq. (A-19) and Eq. (A-20), γ_1 , γ_2 and γ_3 are model constants which (based on Figure A-7 and Figure A-8) are calibrated to be 1.71E-6, 7.38 and 2.11 respectively.

The proposed analytical model, which is shown in Eq. (A-17) through (A-20), was validated by using it to predict the experimental results of Tests 4 and 5 (with hydraulic gradients of 0.60 and 0.75, respectively). In the validation process, first the values of α and β for tests 4 and 5 were calculated by using the calibrated values of γ_1 , γ_2 and γ_3 in Eq. (A-19) and Eq. (A-20) and by using their corresponding hydraulic gradients. Table A-2 shows a summary of calculated values of α and β for Tests 4 and 5. In this table, the calculated values of α and β were obtained by using Eq. (A-19) and Eq. (A-20).

Table A-2: Calculated values of α and β for Tests 4 and 5

Test #	Hydraulic gradient	α	β
4	0.60	1.43E-4	1.27
5	0.75	4.33E-4	1.58

Next, the values of tangent erosion rate for these tests were calculated using Eq. (A-17), Eq. (A-18) and the data given in Table A-2. The comparisons between experimental and predicted values of tangent erosion rate for these two tests are presented in Figure A-9 and Figure A-10, respectively. These figures show that the model predictions have a reasonable agreement with the experimental results.

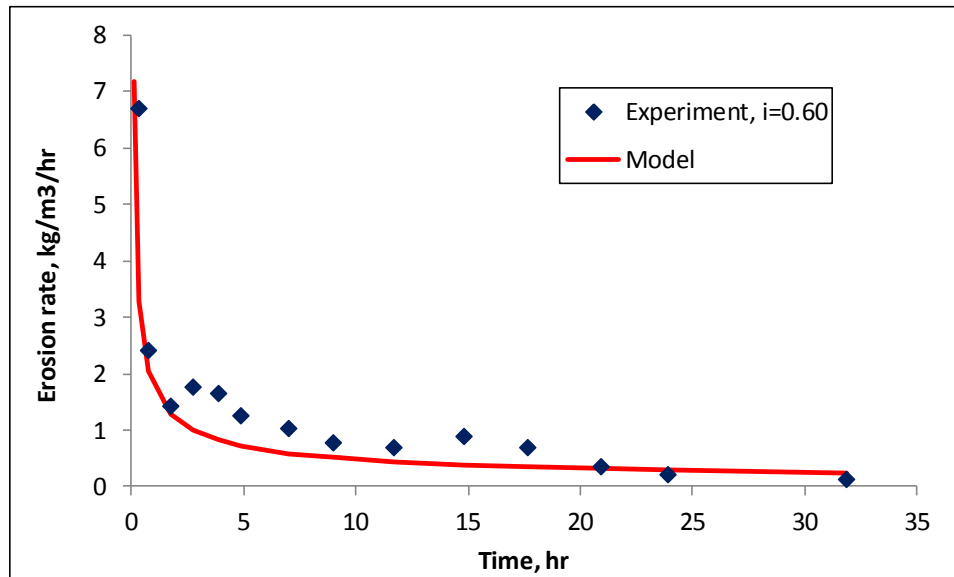


Figure A-9: Comparison between experimental results and model prediction of tangent erosion rate, $i=0.60$

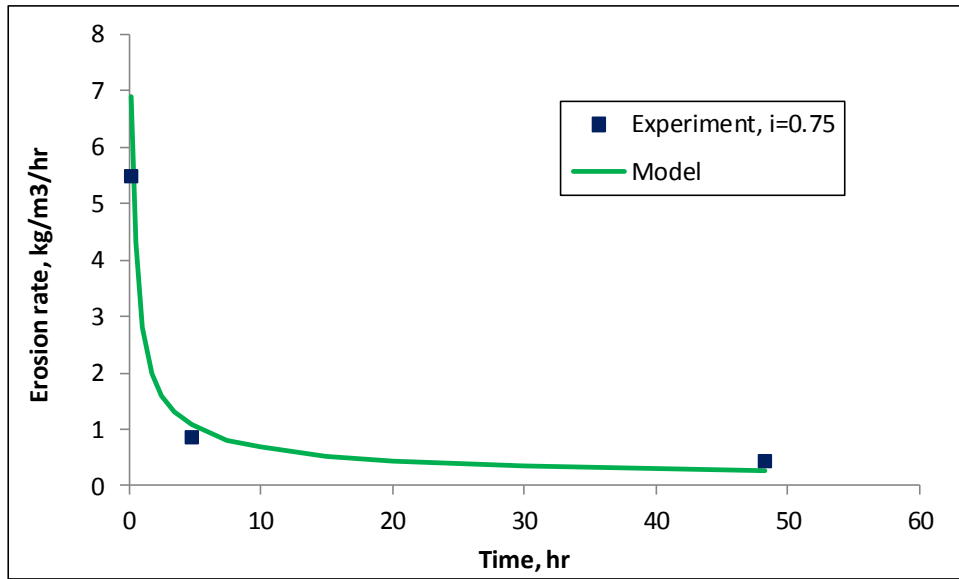


Figure A-10: Comparison between experimental results and model prediction of tangent erosion rate, $i=0.75$